Progress in Materials Science 74 (2015) 211–307

Contents lists available at ScienceDirect

Progress in Materials Science

journal homepage: www.elsevier.com/locate/pmatsci

The fracture of bulk metallic glasses

B.A. Sun, W.H. Wang

Institute of Physics, Chinese Academy of Science, 100190 Beijing, China

ARTICLE INFO

Article history:
Received 6 May 2015
Accepted 19 May 2015
Available online 16 June 2015

Keywords:
Fracture
Metallic glass
Fracture surface morphology
Crack
Deformation

ABSTRACT

The fracture of metallic glasses has received relatively little attention until recently. The development of bulk metallic glasses (BMGs) with more compositions, large sample sizes and diverse fracture behaviors provides a series of ideal model systems for the study of fracture in glassy materials. The fracture toughness of different BMGs varies significantly from approaching ideally brittle to the highest known damage tolerance. Diverse fracture patterns on the fracture surface, fracture modes and dynamic propagation of cracks have been observed in different BMGs. In this review paper, we present a comprehensive view of the state-of-the-art research on various aspects of the fracture of BMGs, including fracture behavior and characteristics, fracture mode, fracture criterion, fracture toughness, and fracture morphology. Accumulated experimental data on BMG fracture are presented and their possible theoretical connections with continuum fracture mechanics and the atomic-scale process are introduced and discussed. Modeling studies of the fracture of BMGs by various computational methods are also reviewed. The review also presents a number of perspectives, including the relation of BMG fracture study to other topics, and unsolved issues for future investigation.

E-mail addresses: iphysunba@gmail.com (B.A. Sun), whw@iphy.ac.cn (W.H. Wang)

http://dx.doi.org/10.1016/j.pmatsci.2015.05.002
0079-6425/

Contents

1. Introduction

Metals and alloys, which have been the most important material class used by human beings for thousands of years, are crystals. This is mainly due to the non-directional nature of metallic bonding, which allows metallic liquid to crystallize much more easily than the melts of covalent bonding matters including organics and polymers. Amorphous alloys, also known as metallic glasses, with the

Nomenclature

AFM	atomic force microscopy
ASTM	standards of American Society for Testing and Materials
BMG	bulk metallic glass
Bcc	body centered cubic
CCD	charge-coupled device
CT	compact tension
CTOD	crack tip opening displacement
DBT	ductile-to-brittle transition
DMA	dynamic mechanical analysis
DSC	differential scanning calorimetry
fcc	face centered cubic
FE	finite element
hcp	hexagonal close-packed
GFA	glass-forming ability
MD	molecular dynamics
MG	metallic glass
MRO	medium range order
NMR	nuclear magnetic resonance
PAS	positron annihilation spectroscopy
RFM	random fuse model
RT	room temperature
SEN	single-edge notched
SENB	single-edge notched bend
SENT	single-edge notched tension
SEM	scanning electron microscope
SOC	self-organized criticality
SRO	short range order
STZ	shear transformation zone
TEM	transmission electron microscope
TM	transition metal
TTZ	tension transformation zone
XRD	X-ray diffraction
a	the half-length of a crack
c_p	specific heat
d	diameter
h	height
f_v	free volume
k_B	Boltzmann constant
p	pressure
r_0	the equilibrium distance between atoms
r_p	plastic zone size
v_l	longitudinal acoustic velocity
v_s	transverse acoustic velocity
t	time
x	displacement
E	Young's modulus
G	shear modulus (modulus of rigidity)
G_C	fracture energy
ΔH	enthalpy
ΔS	entropy
I	current
J	J integral

K	stress intensity factor
K_C	fracture toughness
M	mass
K	bulk modulus (or modulus of compression)
K_C	fracture toughness
K_Q	notched toughness
K_{IC}	mode I fracture toughness
K_{IIC}	mode II fracture toughness
K_{IIIC}	mode III fracture toughness
ΔK_{TH}	the fatigue threshold
L	length
Hv	Vicker hardness
V	volume
V_m	average molar volume
V_a	atomic volume
T	temperature
T_g	glass transition temperature
T_x	crystallization temperature
T_m	melting temperature
T_l	liquidus temperature
T_{rg}	reduced glass transition temperature ($=T_g/T_l$)
ΔT	supercooled liquid temperature region, $\Delta T = T_x - T_g$
γ	the surface energy per unit area
ρ	density of matter
σ	stress
σ_F	fracture strength
σ_y	yield strength
v	velocity
θ	angle
ε	strain
$\dot{\varepsilon}$	strain rate
χ	effective disorder temperature
τ	shear stress
κ_M	machine stiffness
κ_S	sample stiffness
η	viscosity
τ_R	relaxation time
τ_Y	yield shear strength
Ω	the volume of a STZ
Γ	impact toughness
ν	Poisson's ratio

absence of long-range atomic order, did not emerge until 1960, when Duwez et al. [1] performed their pioneering work of the vitrification of an AuSi alloy. Since that time, there has been rapidly increasing interest in experimental and theoretical understanding of this new family of glasses. Initially, the fabrication of metallic alloys was limited to thin foils, wires or ribbons usually prepared by rapid quenching at cooling rates as high as 10^5–10^6 K/s [2,3]. Over the subsequent 30 years, it was found that some alloy compositions, mostly complex multicomponent alloys, exhibit robust glass-forming ability (GFA) and sluggish crystallization kinetics, and their critical cooling rate for glass formation is dramatically

reduced to 1 K/s [4,5]. These alloys, which can be readily cast into fully glassy specimens with characteristic sizes in excess of 1 mm, are termed bulk metallic glasses (BMGs) [4,6–10]. So far, the maximum rod size of metallic glass has reached about 90 mm in diameter [4].

Unlike crystalline metals and alloys characterized by short and long-range order, bulk metallic glasses with amorphous disordered atomic structure display unique and intriguing mechanical, chemical and physical properties, which have proven to be of interest both on the fundamental level and for engineering applications [6–8,10]. For example, with the absence of dislocation defects in the disordered-lattice structure, most BMGs exhibit strengths and elastic limits much higher than those of conventional crystalline alloys and other engineering materials, together with good wear and corrosion resistance at room temperature [7,8]. Fig. 1(a) exhibits a comparison of the strength and elastic limit of metallic glasses with other engineering materials [8]. The strength of BMGs is about twice and the elastic limit is about five times higher than that of conventional steels. Meanwhile, these alloys can be processed to near-net shape due to stable viscous flow in their wide supercooled-liquid region, and very slight shrinkage during the glass transition. Fig. 1(b) shows some as-cast BMGs samples and parts formed with the near-net shape process. One can see that the BMGs samples and parts exhibit shining

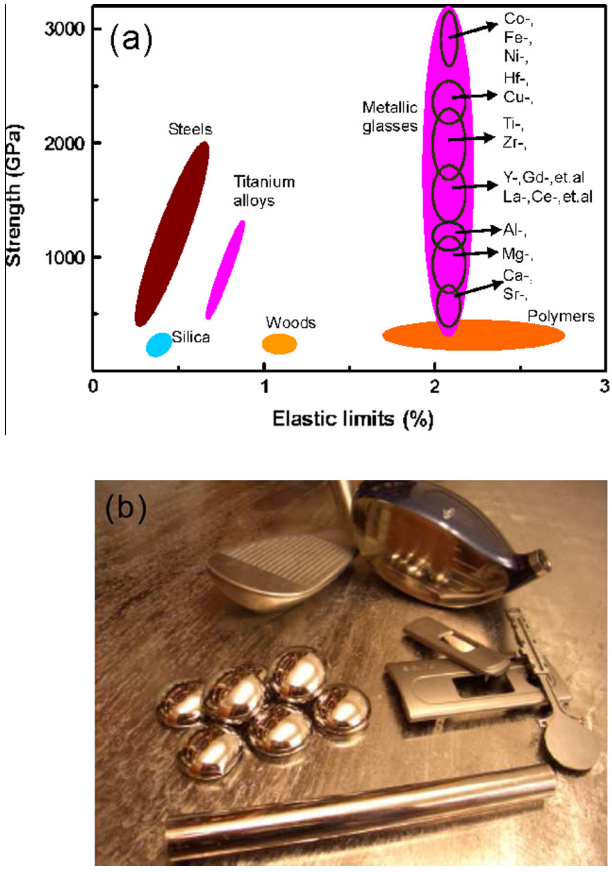

Fig. 1. (a) Comparison of the strength and elastic limit of metallic glasses with other engineering materials (after Ref. [7] with permission. ©2004. Elsevier). (b) Examples of BMG samples and parts including ingots, 12 mm diameter rods, golf clubs, electronic casting, and optical hardware (reproduced from Ref. [11] with permission).

smooth surfaces [9,11,12]. The combination of these attributes makes BMGs highly attractive for various structural, engineering and functional applications. From the point of view of fundamental science, the availability of bulk specimens enables accurate measurement of various physical and mechanical properties which have previously been inaccessible. This opens new opportunities for studying some fundamental issues in glass science and condensed matter physics such as elastic, inelastic and plastic deformations, structural disorder features, and fracture [6,13]. In addition, BMGs, with exceptional stability against crystallization in the supercooled-liquid region, are also ideal materials for investigating the intrinsic viscous behavior and relaxations of liquids as well as the nature of the glass transition [14,15]. Therefore, BMG materials are now extensively studied, as can be seen from an explosion of academic research papers in archival scientific journals in recent years [8,9,11–19].

Fracture, involving the separation of a material into two or more pieces, is the most common way that engineering materials fail. From a microscopic view, the fracture process often initiates at a pre-existing flaw or a micro crack, and then proceeds with the propagation of the crack to create new material surfaces under the applied stress [20]. Technically, understanding how materials break is of crucial importance for structural safety in industrial processes and daily life. Scientifically, the mathematical prediction of how a crack will move in a material is still a challenge [21]. Metallic glasses often fracture catastrophically under tensile loads [8], and are generally regarded as brittle or quasi-brittle materials due to their shear localization and work softening at low temperatures [8]. Compared to elastic and plastic deformations, the fracture behavior of metallic glasses has received relatively little attention until recently. With the increasing development of bulk metallic glass systems with various compositions, BMG specimens with diverse and impressive mechanical properties have been obtained. The fracture toughness, K_c, of BMGs varies significantly from 1.26 MPa $m^{1/2}$ for Dy-based BMGs, which is very close to ideally brittle oxide glasses, up to 200 MPa $m^{1/2}$ for Pd-based BMGs, which exhibit the highest known damage tolerance [9,17]; The Young's modulus E also varies vastly from the 16.0 GPa of Zn-based BMGs to the 246.9 GPa of Co-based BMGs [15]. Unique fracture patterns such as dimple structures, nano-scale periodic corrugations and structures such as nanocones, nanospheres and nanowires, river like patterns, and transitions among them have been observed on the fracture surface of these BMGs. Due to the plentiful metallic glass specimens, it is now possible to experimentally characterize the fracture features of various BMGs and analyze their correlations with processing conditions, microstructure and mechanical and physical properties [22,23]. Their diverse fracture properties, together with their unified deformation mechanism in crack tips, also render the BMGs model systems for studying some critical issues in fracture mechanics such as crack instability, initiation and propagation, fracture surface roughening, and branching [24,25]. Studies of the fracture of metallic glasses have recently triggered great scientific and industrial interest. Theoretical understanding of the fracture mechanism of BMGs at different length scales is also showing remarkable progress by exploiting various computational methods from atomistic to continuum modeling [26–31].

The purpose of this review article is to present a comprehensive overview of the current state of research on fracture in metallic glasses, including their fracture phenomenology, fracture toughness, fracture surface morphology, and the relation between deformation and fracture, as well as the theoretical efforts toward an understanding of the fracture mechanism. Because recent research work on the mechanical properties of BMGs has been reviewed, special attention is paid to the newly reported fracture phenomena, progress, and recent theoretical advances. We start with a brief introduction to theoretical principles and commonly used concepts in fracture mechanics, and present a short review on the general deformation and fracture behaviors of BMGs. After that, we focus on two important fracture characteristics of BMGs: fracture toughness and fracture morphology. Their diversity in various BMGs are summarized and compared, and their correlations with various intrinsic and extrinsic factors are highlighted. We also review recent theoretical advances in understanding fracture characteristics at different length scales in BMGs. Finally, we conclude the paper with some open issues and perspectives which are important for further research in this field.

2. A brief introduction to fracture mechanics principle

Modern fracture mechanics, mainly concerned with crack behavior in the framework of elastic–plastic mechanics, started in the 1920s when Griffith tried to explain the discrepancy between the observed fracture stress and theoretical strength of brittle solids [32]. He considered the problem using a thermodynamic approach. As shown in Fig. 2(a), an infinite elastic thin plate is applied with a fixed tensile stress σ_A at its boundary. The free energy increment of inserting a crack of length $2a$ into the plate can be written as [32]:

$$\Delta U(a) = -\pi a^2 \sigma_A^2 / E + 4\gamma a, \tag{1}$$

where, E is the Young's modulus and γ is the surface energy per unit area. The first term is the released elastic energy, and the second term is the increased surface energy due to the presence of the crack. By setting $\Delta U = 0$, the critical stress for the stable crack growth is:

$$\sigma_f = \sqrt{\frac{2E\gamma}{\pi a}}. \tag{2}$$

Eq. (2) is the famous Griffith strength relation. The σ_f is fracture stress of a material with a pre-existing crack of half length a. The equation accounts for the fact that the observed fracture strength σ_f is usually much smaller than the theoretical cohesive strength of brittle solids of $\sigma_c = \sqrt{E\gamma/r_0}$ (r_0 is the equilibrium distance between atoms) as $r_0 \ll a$. Eq. (2) can also be written as $\sigma_f\sqrt{a} = C$, where C is a constant that reflects the intrinsic properties of materials.

Griffith's theory agrees well with the experimental data for the fracture of brittle materials such as oxide glasses. However, it encounters difficulty in explaining the fracture behavior of ductile materials such as steels. For ductile materials, although $\sigma_f\sqrt{a} = C$ still holds, the surface energy predicted by the Griffith theory is unrealistically high. Irwin [33] assumed that plasticity must play a significant role in

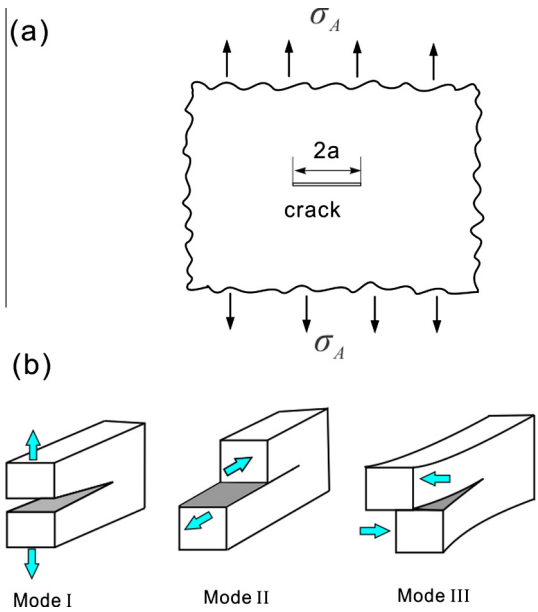

Fig. 2. (a) The schematic illustration for a thin infinite plate containing a crack of the length $2a$ and the fixed tensile stress σ_A applied on its boundary (after Griffth [32]). (b) Three independent crack modes during the fracture: opening (mode I), in-plane shear (mode II) and out-of-plane shear (mode III).

the fracture behavior of these materials, and defined the strain energy release rate with the crack growth as:

$$G = -\frac{dU_e}{da}, \tag{3}$$

where U_e is the elastic energy stored in the material. For ideally brittle materials, the release elastic energy is totally dissipated in creating new surfaces of the crack, and $G = 2\gamma$. For ductile materials, a plastic zone is developed in the crack tip, and the released elastic energy is dissipated both in the plastic deformation of the plastic zone and in creating new surfaces. Thus, G should be written as $G = 2\gamma + G_p$, where G_p is the dissipated plastic energy in the plastic zone. Therefore, the fracture stress can be expressed as $\sigma_f = \sqrt{EG/\pi a}$ for both brittle and ductile materials. For some ductile alloys such as steels, $G_p \approx 1000\ \mathrm{J/m^2}$, which is much larger than 2γ ($\approx 2\ \mathrm{J/m^2}$), and the plasticity around the crack tip thus dominates their fracture behavior [34].

The crack will grow and propagate when G is greater than or equal to a critical value of fracture energy, G_C,

$$G \geqslant G_C, \tag{4}$$

The G_C is an intrinsic materials property independent of loading conditions and sample geometry. The crack resistance curve or R-curve is defined as the plot of the total energy dissipation rate upon the growing crack size.

Besides the modification on the Griffith energy criterion, Irwin and his colleagues [33,34] also developed an alternative method to evaluate crack resistance. Based on the linear elastic theory, they showed that the stress field around a crack tip had the form:

$$\sigma_{ij}(r,\theta) \approx \frac{K}{\sqrt{2\pi r}} f_{ij}(\theta), \tag{5}$$

where $\sigma_{ij}(r,\theta)$ is the Cauchy stress at a polar coordinate (r,θ) with the origin at the crack tip. The $f_{ij}(\theta)$ is a dimensionless quantity depending on the load and the crack geometry, and K is the stress intensity factor with the unit Pa $\mathrm{m}^{1/2}$. Eq. (5) also holds if the plastic zone in the crack tip is much smaller than the size of crack. Generally, complex loading conditions on the pre-existing crack can be resolved into three independent fracture modes: tensile (mode I), in-plane shear (mode II), and out-of-plane shear (mode III), as shown in Fig. 2(b). The stress intensity factors of these modes are labeled K_I, K_{II}, and K_{III}, respectively. Expressions for K under different geometry and loads can be found in literature [35]. As a special case, $K_I = \sigma\sqrt{\pi a}$ is an infinite elastic plate, as in Fig. 2(a). The fracture occurs when

$$K \geqslant K_C, \tag{6}$$

where K_C is a constant and a measure of the fracture toughness of the material. Generally, mode I fracture toughness, K_{IC}, is most commonly used in engineering measurements. Under general loading conditions, the stress intensity factor K is related to strain energy release rate G by [36,37]

$$G = K_I^2\left(\frac{1}{E'}\right) + K_{II}^2\left(\frac{1}{E'}\right) + K_{III}^2\left(\frac{1}{2\mu}\right), \tag{7}$$

where $E' = E$ for the plane stress condition, $E' = E/(1-\nu^2)$ for the plane strain condition, ν the Poisson's ratio, and μ the shear modulus.

The above fracture models and methods are based on linear elastic fracture mechanics, thus these models are generally applied to cases with a small-scale yielding condition around the crack tip. For structural materials (such as steels) which exhibit large-scale plasticity, the linear elastic fracture mechanics cannot accurately characterize fracture behavior, and thus alternative nonlinear elastic–plastic fracture mechanics models have to be used [38]. The J-integral represents one of such ways to describe the strain energy release rate or work per unit fracture surface during crack growth. This theoretical concept was proposed by Rice in 1967 [37] and defined as:

$$J = \int_\Gamma \left(W dx_2 - t_i \frac{\partial u_i}{\partial x_1} ds\right), \tag{8}$$

where Γ is an arbitrary curve around the tip of a crack, $W(x_1, x_2)$ is the strain energy density, x_1 and x_2 are the coordinate directions, t_i is the component of the traction vector, u_i is the displacement vector component, and ds is the length increment along the contour. It is proven that the J-integral is independent of the path of the integration around the crack tip [39]. Physically, the J-integral is essentially equal to the energy release rate or work done on a nonlinear elastic body containing a crack per unit fracture surface area. In displacement controlled conditions, the J-integral can be expressed as:

$$J = -\left(\frac{dU}{Bda}\right)_{\Delta}, \tag{9}$$

where U is the strain energy stored in the body, a is the crack length, B is the thickness and the subscript Δ follows the partial derivative convention indicating the displacement variable that is constant during partial differentiation. For the special case of a linear elastic material, $J_{el} = G$. From Eq. (9), the relationship between elastic J and K factor is obtained:

$$J_{el} = K_I^2\left(\frac{1-\nu^2}{E}\right). \tag{10}$$

Similarly, a fracture criterion can be defined as: $J = J_{IC}$, where J_{IC} is considered as a material parameter for measuring the crack resistance. Effective testing methods for evaluating the critical value J_{IC} for plane strain opening cracks have been developed, and the applied fracture work has been predominantly in mode-I loading and elastic–plastic conditions [38].

In addition to G_C and K_C, there are other parameters to measure the fracture toughness of a material, including crack-tip opening displacement (CTOD) [40] and crack-tip opening angle (CTOA) [38]. These parameters are usually used to evaluate the fracture resistance of a material with large-scale plasticity in the crack tip. As these parameters are seldom involved in the fracture of BMGs, we will not discuss them here. For their definitions and testing methods, one can refer to literature [34,38] and the standards of American Society for Testing and Materials (ASTM) E399, E561, E813, E1290, E1820 and E2472 [41,42].

3. Fracture phenomenology of BMGs

3.1. The plastic deformation process before fracture

Fracture behavior is closely related to plasticity in the crack tip in BMGs. Therefore, it is necessary to introduce and discuss the plastic deformation behaviors of BMGs before thorough discussion of their fracture. Due to their disordered atomic structure, BMGs display unique deformation behaviors which are completely different from that of their counterpart crystalline alloys [9,17–19]. Macroscopically, the plastic deformation of BMGs strongly depend on temperature and applied strain rate, from which a deformation map has been constructed [8]. At high temperatures (close to the glass transition temperature, T_g) and/or low strain rates, BMGs deform homogeneously with each volume element of the specimen. In this case, the deformation can be viewed as a viscous flow process (Newtonian or non-Newtonian flow behavior, or thermoplastic forming process) with a low flow resistance, and the BMG behaves liquid-like, which is directly related to the shape-forming process that provides technologically unique metal-processing opportunities. Because of this, the homogeneous flow behavior of BMGs has been extensively studied [8,19,43]. At lower temperatures ($<0.8T_g$), BMGs manifest high strength and large elastic limit, and their plastic deformation is usually inhomogeneous with plastic strain highly localized into nano-scale narrow regions termed as shear bands [8]. The shear band is usually 10–20 nm in thickness as observed by TEM and predicted by theory [44]. However, the shear band can accommodate displacement nearly up to millimeter scales, yielding an extremely large plastic strain within them. The plastic shear along the shear band plane often leaves some slip steps in the surface of BMG specimens as shown in Fig. 3. Once initiated, shear bands become unstable and propagate rapidly, often leading to catastrophic fracture of BMGs. Thus, the shear bands play a central role in understanding plastic deformation and fracture behavior of BMGs as well as in controlling and designing the plastic metallic glasses [9,17–19].

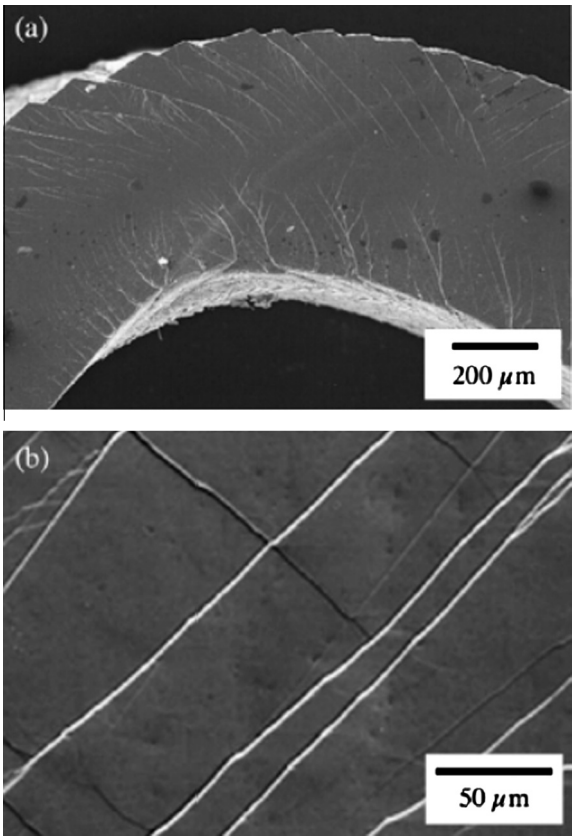

Fig. 3. Scanning electron micrographs (SEM) showing the surface slip steps associated with shear bands in BMGs. (a) The slip steps formed during the bending of a strip of $Zr_{57}Nb_5Al_{10}Cu_{15.4}Ni_{12.6}$ BMG on both tensile and compressive sides. (b) The slip steps formed on the side surface of the sample during the compression of a $Zr_{52.5}Cu_{17.9}Ni_{14.6}Al_{10}Ti_5$ BMG, for which the loading axis is vertical (reproduced from Refs. [8,295] with permission. ©2007. Elsevier).

Despite extensive studies in the past decades, the physical origin of the shear localization process is still not fully clarified. From the viewpoint of mechanics, the shear localization is closely related with a strain softening mechanism. The deformation-induced soft regions concentrate more strain and eventually lead to spatial instability in the strain rate partition [45,46]. For BMGs, there are two potential causes for the strain softening: the shear-induced dilation (structure disordering with more free volumes) [45] and temperature rise [47]. The early experimental studies [48] on pre-etching of existing shear bands provide clear evidence for structure disordering, while there is still much uncertainty and debates regarding significant local temperature rise during deformation. Theoretical calculations and experimental studies have shown a wide range of values from less than 0.1 K to a few thousands of Kelvins. For example, by measuring the shear band displacement and duration during a shear serrated event in a time-resolved experiment, Wright et al. [49] calculated the temperature rise in the shear band by assuming that shear occured either on the whole shear plane or as a propagating shear front, and got a maximum temperature rise of 65 K, which is much lower than the glass transition temperature. In contrast, Lewandowski et al. [47] demonstrated, using a fusible coating technique with excellent temporal (∼30 ps) and spatial (∼100 nm) resolution, that the temperature rise could be a few thousand Kelvins in the operating shear band. Direct measurements with the high-speed infrared cameras have also reported a variety of temperature values from 3 to 900 K [50,51]. Clearly, the difficulties in measuring and theoretically predicting the temperature rise within shear bands are closely

related with the strong spatial and temporal localization of shear banding. Despite the controversy on this issue, significant temperature rise indeed occurs, and it is believed to play a critical role in the final fracture process of BMGs [52].

Although BMGs display diverse deformation behaviors macroscopically, their underlying atomic-scale processes might be the same. Accumulating evidence [53,54] shows that the deformation of BMGs could be accomplished by the local arrangement of some atomic clusters which can accommodate the shear strain. This is completely different from the dislocation-mediated plasticity in crystalline alloys. In addition, these local atomic arrangement processes often occur at high stresses and energies as compared to the dislocation process in crystalline materials due to the lack of long-range translational order in BMGs. Some theoretical models have been proposed. Among them the most commonly used are the free volume theory proposed by Spaepen [45] and the shear transformation zone (STZ) theory proposed by Argon [46], and then subsequently improved by Langer et al. [54,55]. The free volume model considers the deformation in metallic glass as a consequence of diffusion-like atomic jumps biased by the shear stress, and these jumps are favored by nearby sites with high free volume. At low temperatures, the free volume can be created by squeezing an atom into a small empty space which is then annihilated by the diffusion. However, it is difficult to understand why the atomic jumps would be biased by the shear stress, and the single atomic jump cannot in fact accommodate shear strain in glass, either. Nevertheless, the free volume model indeed provides a simple and clear way to model the issues of deformation and glass transition. In the shear transformation zones (STZs) model, the plastic shear deformation of glasses is described by the cooperative shearing of atomic clusters termed as STZs instead of single-atom jump process [43]. The free volumes are created by the shear dilation associated with the operation of STZs, and lead to the reduction of shear resistance or strain softening in these local regions. Compared to the free volume model, the STZ picture for shear deformation in BMGs is more realistic and has been verified by atomic simulations on glass deformation [53,54]. However, the STZ model views the shear deformation as a thermally activated process and uses the single parameter of free volume as the internal state variable to control the deformation process. Based on the STZ model, Falk and Langer [54,55] later proposed a generalized version of STZ theory, which incorporates more internal state variables (such as the number of STZs and effective temperatures) and thus can describe the transition of STZs in the absence of thermal activation. Many other models were also proposed, and these models essentially replace the free volume with another state variable (such as the "fictive stress" [43]) or use more sophisticated expression for the activation energy (such as in the cooperative shear model [56]), and thus remain philosophically similar to the STZ theory.

Many theoretical analyses based on the above models have also been put forth to explain various features of deformations in BMGs. For example, the overshoot observed in the homogeneous deformation regime can be interpreted as the non-steady evolution of free volume during deformation [57]; shear localization at low temperature is ascribed to a spatial instability process of the state variable evolution during deformation [46,57–59], and an example of such instability is shown schematically in Fig. 4(a); the thermal effect on the strain softening and shear band instability can also be analyzed by considering heat conduction in some coupled thermo-mechanical models [59,60]. However, these analyses are generally based on the dynamic instability method wherein the local region to be developed into shear bands is usually prescribed in advance (usually soft regions with slightly more free volumes), thus the microscopic nature of the shear localization, that is, how the STZs organize and coalescence into a shear band, cannot be fully understood from these models. Recent theoretical work by Dasgupta et al. [61] seems to give some hints along this direction. By computational and theoretical analysis, they showed that the STZs are spatially correlated with the long-range quadrupolar stress field from the Eshelby inclusion theory, and that the formation of shear bands, with the appearance of the highly correlated Eshelby-like quadrupolar singularities organized at a line that is 45° to the principal stress axis [see Fig. 4(b)], corresponds to a minimum state of the total interaction energy.

However, it is quite elusive to define the free volume or STZ, which is not a structural defect, but a local transient event which cannot be experimentally visualized like dislocations or grain boundaries in crystalline materials. Recently, intensive work shows that the structure of metallic glasses is not uniform in nanoscale as thought before [62–72]. Using X-ray diffraction (XRD) and anisotropic pair-density function analysis, Dmowski et al. [62] showed that one-quarter in volume fraction of

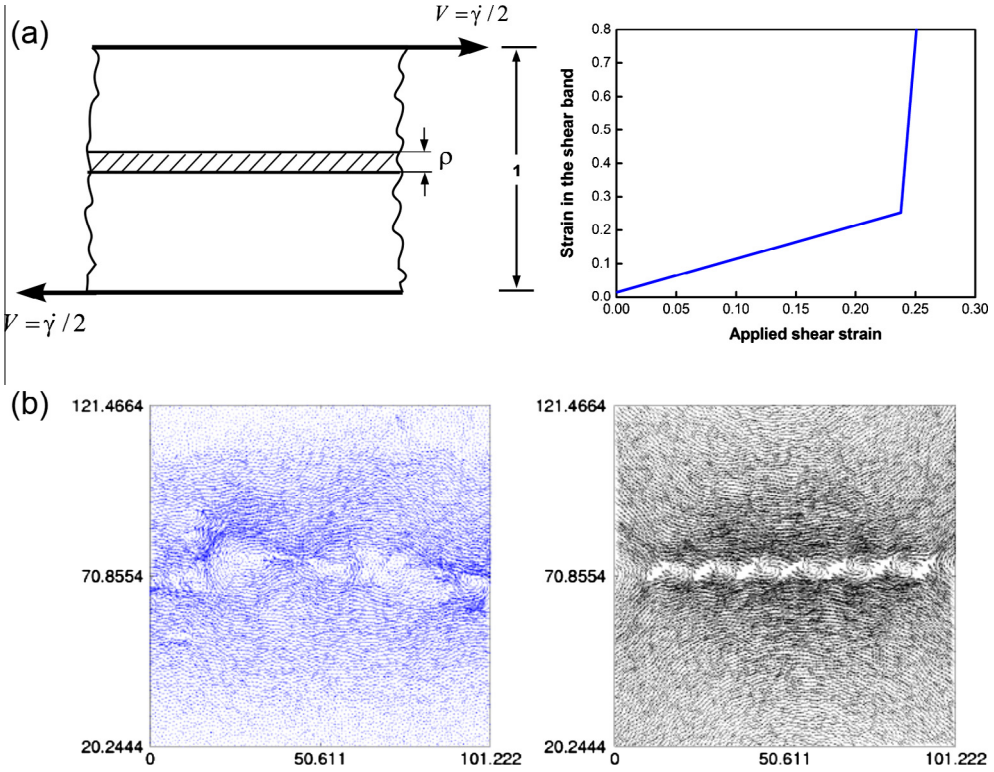

Fig. 4. The shear localization process in metallic glasses. (a) The development of shear band from a prescribed thin layer (thickness ρ) with initially relatively larger free volume (the left) due to the instability of spatial evolution of free volume. The strain evolution in shear band with the applied strain are shown in the right (after the work of Ref. [57]). (b) The formation of shear bands in the atomic scale due to the interaction and organization of STZs: the left is the molecular dynamic (MD) simulation results and the right is the theoretical calculation results by minimizing the interaction elastic energy between STZs (reproduced from Ref. [61] with permission. ©2012. American Physical Society).

BMGs an elastically deforms without resistance, and this anelastic portion can be considered as residual liquidity in the glass. Dynamic micro-pillar tests also indicate the inelastic deformation zones exist in BMGs [63], and that nanoscale mechanical heterogeneity in BMG is also characterized by dynamic force microscopy [71]. It is also found, using an atomic force acoustic microscopy, that the local elastic constants of a PdCuSi metallic glass exhibit a wide distribution in a scale below 10 nm [64]. Granato et al. proposed an interstitialcy theory [73] which claims that the interstitialcies inherited from the liquid are defects in the glass, that these defects decrease the shear modulus of the glass compared to the crystalline counterparts, that deformation in BMG can be attributed to the generation of interstitialcy-like defects. Dynamical mechanical analyzer (DMA) results show that BMG is viscoelastic and can be divided into solid regions, which are the source of storage modulus, and liquid like regions, or flow units, without stress resistance, which provide the loss modulus and accommodate the plastic deformation [65,66,72]. In colloidal glasses, Spaepen et al. [74] obtained direct 3D images of thermal-induced localized irreversible flow units and their evolution with temperature. Through atomic-resolution spherical aberration-corrected TEM, localized regions with large rearrangements suggesting the existence of the liquid-like zone in 2D SiO_2 glass were directly observed [75]. Simulations also show evidences of dynamic heterogeneities in glasses, that atomic or molecular rearrangements differ from one region of space to another [67,76,77], and that localized plastic events initiate the shear bands and plastic deformation in BMGs [78].

The intrinsic nanoscale liquid like regions can be considered as a property "defects" or dynamic "defects" of BMGs, and the actual structure of BMGs can be regarded as these liquid-like regions

(which act as the viscous flow units for deformation and glass transition) embodied in the elastic solid matrix, that is: metallic glass = ideal elastic glassy matrix + flow units [65,66,68,79–87]. Compared with the elastic matrix, the defects of flow units are a group of atoms exhibiting a lower packing density, higher atomic mobility, higher energy dissipation rate, lower modulus, and higher energy states in the energy landscape [77–85,88]. The flow units show a collective rearrangement process during stress or thermal induced deformation. Experimental evidence strongly supports the existence of flow units for deformations in metallic glasses, and the challenge now is how to characterize the flow units, and to correlate the flow units to macroscopic physical properties of metallic glasses [88]. In crystalline metals and alloys, the density of dislocations can be changed and controlled through heat treatment, plastic deformation or microalloying. By controlling the density of dislocations, the mechanical and physical properties of metallic materials can be modulated. To control and modulate the properties of BMGs, it is essential to know the effects of the concentration of structural defects of flow units on their performance. However, it is difficult to directly observe, identify and characterize the flow units in BMGs using current experimental methods.

It is known that glass-forming liquids show a large range of relaxation times, or various relaxation modes with different energies or frequencies [18]. Rapid quenching can freeze the large scale and slow primary relaxation (the so-called the α-relaxation), while the fast secondary beta-relaxation, which is a reversible process, can be kept in the glass state, [77,84,85]. The microstructural origin of β-relaxation in metallic glasses is associated with the motion of groups of loose atoms in nano-scale localized soft regions of metallic glasses [87b,88], which is reminiscent of potential STZs or flow units in BMGs, because in simple atomic BMGs, no complicated mobility forms such as the intramolecular effect in other non-metallic glasses exist. This indicates that the β-relaxations reflect the dynamic behavior of flow units in BMGs.

In crystals, the internal friction can detect defects such as grain boundaries. In BMGs, the β-relaxations associated with the dynamic flow units can also be determined by using internal friction or dynamic mechanical analysis methods. Systematical studies show that the β-relaxation is universal in BMGs and can be detected both in frequency and temperature domain by DMA. Based on the obtained data of activation energy for STZs (W_{STZ}) and β-relaxations (E_β) in various BMGs, a clear correlation between E_β and W_{STZ} for BMGs is revealed. This indicates that the flow units and β transition have common structural origin, and that the activation of STZs and the β-relaxations are directly correlated [84]. The β-relaxations, similar to the events of potential STZs, take place in loosely packed regions, where the local translational atomic motion can be readily activated compared with that in closely packed regions, meaning that structural heterogeneity is the common structural origin of flow units and β-relaxations. The β-relaxation in BMGs then corresponds to a process involving "thermal driven flow units", i.e., a group of atoms within loosely packed regions undergoes an inelastic distortion from one configuration to another, crossing an energy barrier induced by thermal fluctuations. The localized flow process is reversible due to the confinements of the surrounding closely packed regions. Therefore, the β-relaxation represents nano-scale localized dynamics in metallic glasses, and provides a route to identify and characterize the flow units for initiation of deformation in structural disordered glasses especially in relatively simple atomic BMGs.

The percolation of homogeneously and stochastically activated flow units forms a shear band. With the activation of a sufficiently large population of flow units in the glass, they eventually exceed the percolation limit. The percolated flow units, along the plane with maximum shear stress, form a deformation band, which is softened due to the activation of flow units and therefore concentrates subsequent shear strain. A shear band then develops from this [87,88]. In the next section, we will address the features of a shear band in metallic glass.

3.2. The shear banding process: precursor of the fracture of BMGs

In BMGs, macroscopic plastic deformation at room temperature is mainly accomplished by highly localized shear bands. Once a shear band is initiated in a local region by softening which is attributed to the influence of local heating or shear dilation (localized arrangement events), it will propagate rapidly with the reduced resistance or viscosity in its vicinity, resulting in crack formation in the band and subsequent fracture [8]. In this regard, the shear banding process can be viewed as the precursor

of fracture in BMGs, which is important for understanding the fracture of BMGs. In general, once triggered, a shear band in BMG will quickly become unstable in a runaway manner under unconstrained loading such as tensile testing [89,90], leading to the catastrophic failure of the glass along the primary shear plane, and the macroscopic outcome is the almost zero tensile ductility of the BMGs. As the plastic flow is strongly localized both in space (10–20 nm in thickness) [44,91] and time (1–2 μs in duration) [49,89] during shear banding, it is difficult to directly characterize the shear band evolution process by conventional experimental methods such as transmission electron microscopy (TEM) and SEM. However, the shear banding process under constrained loading such as compression does not always have catastrophic consequences. For example, the shear banding process in the case of compression of some BMGs can be manifested as stable serrated flow behavior [89,92–94] in the plastic regime of stress–strain/time curves, as shown in Fig. 5. We can see that one serration usually comprises a sudden stress drop part and an elastic reloading part, and that the sudden stress drop part often corresponds to the rapid shear band operation process, during which the shear band propagation velocity (v_{sb}) is much higher than the external loading rate (v_0), while the elastic reloading part corresponds to the slow creep process of the shear band where $v_{sb} < v_0$ [95]. Therefore, it is possible to investigate the dynamic evolution of shear banding until the final fracture by carefully characterizing the serrated flow behavior in BMGs.

As early as 1978, there were intensive studies on shear band dynamics [96,97]. For example, Neuhäuser [97] used a high-speed cinematography (up to 600 frames per second) in an attempt to capture the development of shear bands during deformation. Other experiments' techniques [98,99], such as utilizing linear variable differential transformers with an acquisition rate of 100 Hz in order to capture the displacement burst during the shear band operation, attempted to obtain the shear band speed. However, these early experiments generally lacked the temporal and spatial resolution necessary to conclusively determine shear band speed. Because few and limited datum points were recorded in each displacement burst during serrated flow, only a lower bound for the shear band speed could be reasonably determined from the data [49]. Furthermore, it was also unclear whether a flow serration recorded in the load–displacement curve corresponded to a successive (intermittent) shear along a single shear plane or to random shear band emission, which also blurred the investigation on shear band dynamics [96]. We note that it is necessary to distinguish the difference between shear band "propagation" and "operation", as the difference affects the measured shear band velocity. Here, we arbitrarily define the shear band "propagation" as the cooperative motion of

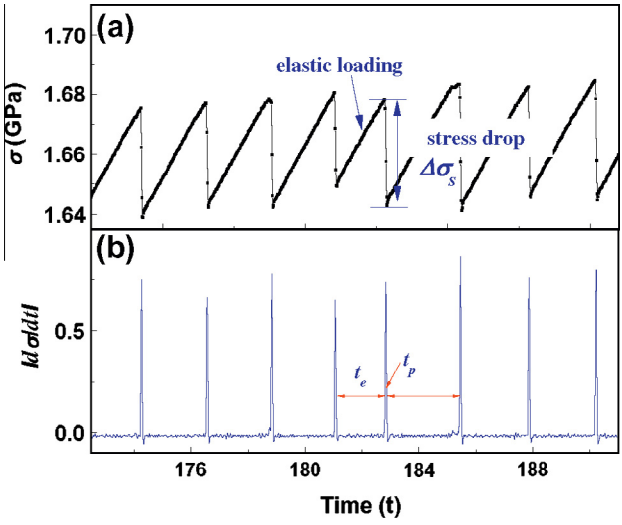

Fig. 5. (a) A typical segment of serration taken from the stress-time curve of a $Zr_{65}Cu_{15}Ni_{10}Al_{10}$ BMG sample. (b) The absolute derivative of the stress to the time from (a), which shows the duration time of the elastic loading part and stress drop part, respectively (reproduced from Ref. [92] with permission. ©2012. Elsevier).

the band along the shear plane, and define the shear band "operation" as the progressive motion of the shear front before the establishment of the propagation. Recently, Song et al. [89] found that the regularly spaced striations observed on the fracture shear surface matched well with the flow serration in compression of a Zr-based BMG, indicating that the serrated flow in the compression may arise from the stick–slip motion of a single dominant shear band. This point was further verified by *in-situ* compression experiments where a one-to-one correspondence was observed between the intermittent sliding of the primary shear band and the serrated events in the stress–strain curves. Based on this view, they measured the velocity of the shear band by carefully characterizing the displacement burst and the elapse time of a serrated flow event with high-sensitivity strain gauges [89]. The strain gauges were capable of capturing small strains (10^{-5}) with a high data acquisition rate (2 kHz). A three-step (acceleration, steady-state and deceleration) process in shear band propagation was discovered in each displacement burst and each stage was associated with different shear band propagation velocities, as shown in Fig. 6. Particularly, the shear band speed in the steady-state stage is much faster than the crosshead speed. The maximum speed is calculated to be 8×10^2 μm/s, almost 1000 times that of

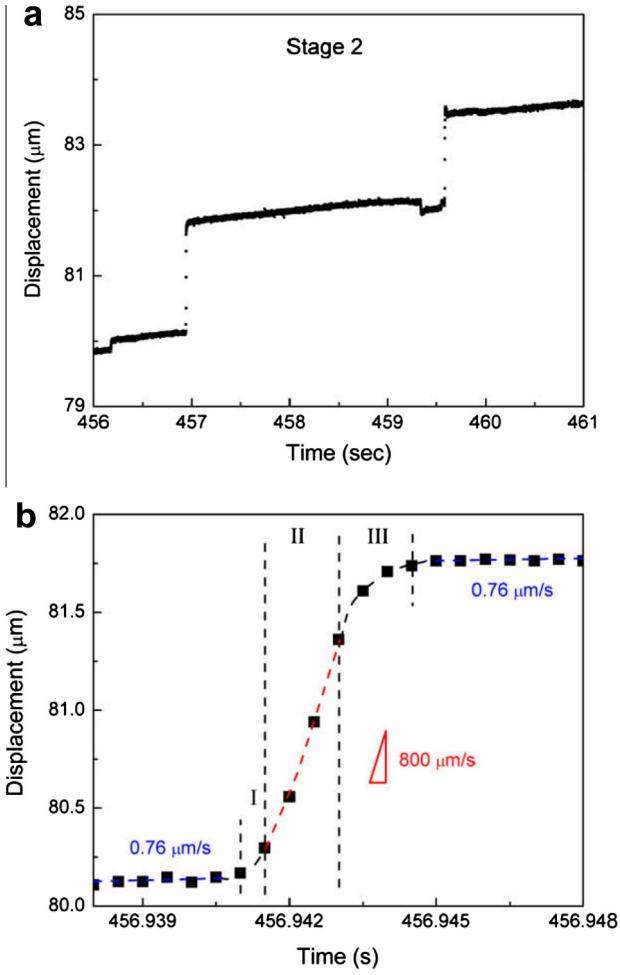

Fig. 6. (a) Displacement as a function of time in the serrated flow of the $Zr_{64.13}Cu_{15.75}Ni_{10.12}Al_{10}$ BMG during compression. (b) Typical serration profile including three stages of shear band propagation (acceleration, steady-state, deceleration) (reproduced from Ref. [89] with permission. ©2009. Elsevier).

the crosshead speed, where the motion of a single shear band is found to be the cooperative shear along the plane, and thus the speed measured is the shear band propagation speed. With experimentally measured load drop, displacement and elapsed time during one serrated event, the viscosity of a propagating shear band can then be determined, which is relatively low and in a similar range to that usually measured in the supercooled-liquid region [89]. A similar but improved experimental approach was also employed by Wright et al. [49]. The strain and load data were acquired at a time-resolved rate of up to 400 kHz using strain gauges affixed to all four sides of the specimen and a piezoelectric load cell located near the BMG specimen. The measured propagation rate is 0.002 m/s assuming that the entire shear plane operates simultaneously. Instead, if one assumes that the displacement occurs as a localized propagating front, the operation velocity of the shear front is approximately 2.8 m/s. In either case, the shear band velocity is orders of magnitude less than the shear wave speed (2000 m/s) in BMGs, and the maximum temperature increase in a shear band during serrated flow predicted by thermal modeling based on this range of shear band velocity is only 65 K, which is insufficient to melt the glass as happened in the final catastrophic failure.

The serrated flow in the compression of BMGs has recently been interpreted as a stick–slip instability of the shear banding process. As most monolithic BMGs are deformed by the formation of a single dominant shear band, the compression process of a BMG sample can be simplified into a machine-sample system (MSS) as schematically shown in Fig. 7. In this system, the effects of elastic

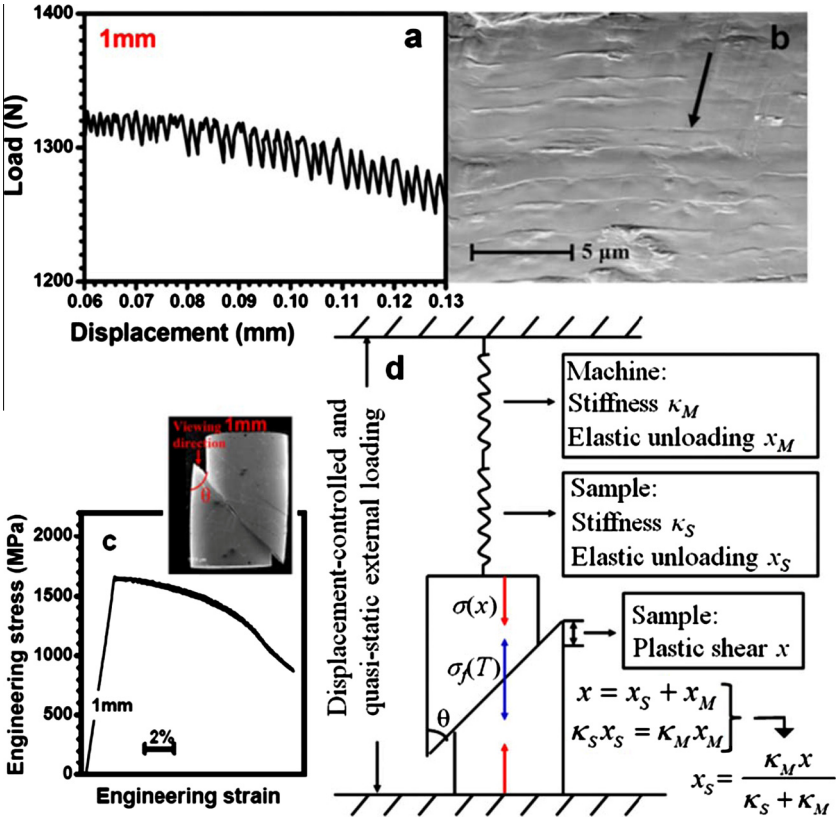

Fig. 7. The stick–slip process of shear banding in the compression of BMGs. (a) Serrated load–displacement curve of a BMG sample. (b) Striations on the shear fracture surface after deformation. (c) The entire stress–strain curve showing large plastic strains of a sample with d = 1 mm and stable stick–slip shear banding process. (d) The schematic of the machine-sample system in the compression of BMGs where a single dominant shear band is formed (reproduced from Ref. [106] with permission. ©2009. American Physical Society).

deformation of the testing machine and the sample are modeled as two springs with the stiffness κ_M and κ_S, respectively (d and L are the diameter and length of the sample, respectively, and E is the Young's modulus). The machine-sample system is loaded at a constant loading rate v_0 (corresponding to a constant strain rate) from time $t = 0$, and thus the elastic energy is gradually stored in the system with the driving force of $\kappa_M\kappa_S v_0 t/(\kappa_M + \kappa_S)$. Once the sample is loaded up to the yield stress, a major shear band will be activated [100]. The operation or sliding of the band will cause the partial release of the elastic energy in the system. For a vertical sliding displacement x in the band [see Fig. 7(d)], the driving force is relieved by $\kappa_M\kappa_S x/(\kappa_M + \kappa_S)$. Thus, the plastic flow of a system is fully accommodated by sliding of a single shear band, which can be described by the dynamic equation:

$$\frac{\kappa_M\kappa_S}{\kappa_M + \kappa_S}(v_0 t - x) - \frac{\pi d^2}{4}\sigma_f = Mx'', \tag{11}$$

where d is sample diameter, M is the effective inertia of the system (typically in the order of 10–100 kg), x'' is the second time derivative of x. σ_f is the internal resistant stress of shear band, which is function of strain rate or sliding rate and internal state variables (such as the free volume and temperature) in the band, and can be given by constitutive deformation law of the BMG: $\sigma_f = f(v, states)$ with v the instantaneous sliding rate of shear band. Divided by the area of the sample, the prefactor in the first term of Eq. (11) is usually replaced with an elastic constant k [$k = E/L(1 + S)$ with $S = \kappa_S/\kappa_M = \pi d^2 E/4L\kappa_M$], which represents the combining elastic effects of machine and sample. From Eq. (11), the dynamics of shear band sliding is determined by two factors: the driving force $\sigma_d = k(v_0 t - x)$ and the shear flow resistance of band $\sigma_f = f(v, states)$. For $\sigma_d > \sigma_f$, shear band sliding is accelerated, and for $\sigma_d < \sigma_f$, shear band sliding rate slows down to cease [101]. The competition between the two factors will result in jerky flow in the stress–strain curve where the band undergoes undergoes alternating negligible ($v \leqslant v_0$) and rapid ($v \geqslant v_0$) sliding rates. If the detailed expression of $\sigma_f = f(v, states)$ is prescribed, the critical condition for the appearance of serrated flow or stick–slip instability of shear band sliding can be quantitatively analyzed [100,102].

Stick–slip dynamics of shear banding process suggests that shear stability or plasticity of BMGs is not only affected by intrinsic properties such as the glassy structure and the elastic modulus (such as Poisson's ratio) [103], but also is influenced by various extrinsic materials properties (such as sample size) and experimental factors (such as the machine stiffness). Indeed, this viewpoint has been verified by recent experimental results. For example, Han et al. [104] showed that compressive plasticity of monolithic BMGs strongly depended on the sample size and the stiffness of the testing machine. They proposed a parameter S ($S = \kappa_S/\kappa_M = \pi d^2 E/4L\kappa_M$) in stick–slip dynamics to govern the critical transition from unstable to stable shear banding with variation of sample size and machine stiffness. In addition, enhanced or reduced plasticity may be also a consequence of geometrical constraints during mechanical testing. For example, a series of carefully compression tests [105] find that any deviation from a perfect coaxial alignment of the sample with respect to compression axis can result in a large apparent plasticity. Cheng et al. [106] also proposed a stick–slip model for operation of a single shear band by incorporating temperature as an internal variable in shear band dynamics. The analysis results could quantitatively illustrate how the experimental factors (such as the sample size and machine stiffness) affect temperature rise in the shear band. It should be noted that in theory, materials are not expected to fracture in compression, because theoretically there is no opening stress to initiate a crack. However, in practice, we do often observe fracture in compression of metallic glasses. As fracture usually occurs along the shear plane of the primary shear band, one can presume that the fracture is closely related with the mode II crack instability and microscopically, and this kind of fracture is mainly caused by fluid meniscus instability due to significant softening in the shear band, which will be discussed in details in Section 5.1.

Stick–slip instability is not only limited in low-temperature deformation of BMGs, but also in a large number of systems ranging from atomically thin films to earthquake faults [93]. Rich and complex dynamics have been revealed such as chaotic and self-organized critical (SOC) dynamic systems exhibiting different internal physics [107]. Recently, the understanding of plastic flow process of materials with non-equilibrium dynamic concepts have aroused considerable research interest [108,109]. In crystalline solids, intermittent plastic flow or discontinuous yielding, known as the

"Portevin Le Chatelier" effect [110], is closely related to dislocation avalanche. The number of avalanche events and their magnitudes are found to follow the power-law scaling or scale-free flow from either direct [111] or indirect acoustic emission measurements [108], which cannot be explained by conventional continuous model of plastic deformation and is reminiscent of the SOC dynamics. For BMGs, the intermittent plastic flow or serrated events can also be considered from avalanche dynamics, even dislocation-mediated plasticity is absent in their disordered structure. Considering the plastic deformation of BMGs is an intrinsically dynamic process, it is expected that shear stability or ductility of BMGs is closely associated with dynamic characteristics of serrated flow behavior. Sun et al. [112] examined the correlation between dynamics of serrated flow and plasticity in BMGs with different ductility. As can be seen from Eq. (8), shear displacement is proportional to stress drop in a serrated event, and the amplitude of the stress drop in serrations can be used as a measure of the size of the plastic event. By performing a systematically statistic analysis on the stress drop associated with each serration in stress-time curves of various BMGs, they find that, without exception, the stress drop distribution of all brittle BMGs (with the plasticity $\varepsilon_p < 5\%$) displays a peak shape with a characteristic size, while for ductile BMGs ($\varepsilon_p > 10\%$), the stress drop distribution follows a power-scaling without characteristic sizes. The peak-shape distribution of serration sizes, similar to that observed in single crystals, indicates a chaotic dynamic state [113]. Indeed, this has been verified by dynamic time series analysis on stress-time curve of a brittle BMG, which exhibits finite correlation dimension and positive Lyapunov spectrum [93]. In contrast, the power-scaling of serrated events, together with a large number of interacting shear bands observed in post-deformed samples and slow external loading rate, suggest that the dynamic for plastic deformation of ductile BMGs evolves into the SOC state [114]. The SOC, which has been observed in many complex systems in various fields, means that the system can buffer against large changes, and the endure intervention as any external impact on such a complex system is dissipated throughout the networks of connected participants [112]. Therefore, SOC dynamics can result in a large stable plasticity in ductile BMGs. This also provides a new perspective on plastic deformation mechanism of BMGs and may have implication for exploring new ductile BMGs. In addition, the emergence of the SOC state suggests that one must consider the effect of shear-band interaction during deformation of ductile BMGs. The important role of shear-band interaction on stick–slip dynamics and stability has been recently explored by well-designed multiple-sample compression experiments [92]. A stick–slip model considering interaction of multiple shear bands is also proposed. Numerical calculation results (see Fig. 8) of this model show that sliding of multiple shear bands are well correlated and organized into intermittent shear avalanches following a power-law scaling, which is well consistent with experimental observations. In addition, these sliding events appeared in an intermittent, trigger aftershock pattern in which small events leading to smoothing in a larger scale and a larger event later on, similar to what happened in the fault dynamics [115]. Furthermore, fractal analysis on surface morphology at compressive plastic strains in BMGs indicates that multiple shear band patterns are self-similar fractals [116]. The formation and interactions of multiple shear bands during deformation of ductile BMGs could be a laboratory system to mimic the earthquakes [112].

There are several studies [117–121] concerning about shear band formation, organization and spacing in bending of BMGs. Under such loading mode, BMGs are subjected to inhomogeneous stress state across plate sample, with tensile stress at the outside surface gradually transferring to compressive stress at the inside surface. As the driving stress of shear bands diminishes approaching the neutral axis, bending can be regarded as an inherently stable method of deformation. Shear band formation in bending shows multiplicity on both sides. Fig. 9 displays typical scanning electron microscope (SEM) observations of shear band patterns under bending [117]. Although the primary shear bands on both surfaces show initially uniform spacing, shear offsets initially propagate at $\sim 50^\circ$ with respect to the free surfaces, yet the patterns are not symmetrical on both sides. Those on the tensile side tend to be longer and more uniformly spaced than that on the compressive side. In addition, the secondary and tertiary bands are evenly spaced on the tensile side, while they form numerous branches on the compressive side. Further investigations [117–119] revealed that both the spacing between shear bands (including primary shear bands and secondary shear bands) and the shear offset scaled linearly with sample thickness as well as bending radius. Specifically, both shear band spacing and shear offset increase with the increasing sample thickness, and similar correlation is also found

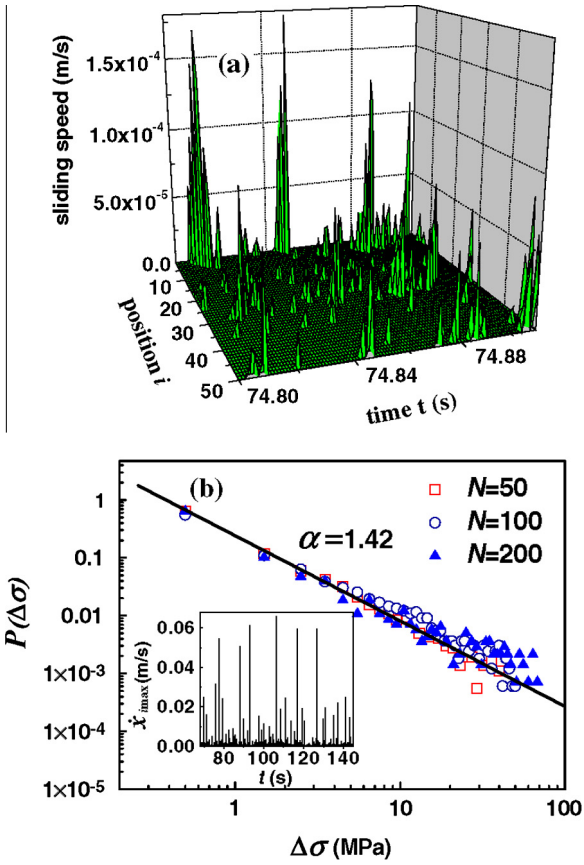

Fig. 8. Numerical solutions for the stick–slip model of multiple shear bands. (a) The shear band sliding are organized into shear avalanches with different sizes. (b) The probability distribution of stress drops due to the shear avalanches for different numbers of multiple shear bands, which can be well fitted by a power-law scaling. The details for the numerical calculations can be found in Ref. [112] reproduced with permission. ©2010. American Physical Society).

with respect to the bend radius. Shear banding process in bending has been assumed to be responsible for size-dependent bending ductility, i.e. the strain to fracture increases markedly as the sample thickness drops below about 1 mm. Some analytical models [118–121] are proposed to explain the scaling law of the shear band features observed in experiments. For example, Conner et al. [120] consider strain relaxation in the vicinity of shear band, which causes other shear bands to be excluded from that band and leads to the increasing shear band spacing with increasing plate thickness. If a critical length for the unstable shear band propagation and the crack initiation are given, the model could predict the thickness-dependent bending ductility. Further delicate models consider energy dissipation along shear bands [119] or momentum diffusion from the elastic–plastic theory of bending, coupled with some deformation features of metallic glasses [118,121] (such as normal stress or pressure dependence of yield stress and strain softening). Although these models could capture some features observed in experiments, they are in general in the framework of continuum mechanics and thus have a mean-field nature. The issues that how multiple shear bands initiate from elastically coupled atomic-scale deformation units and how shear band interact with each other during their evolution process in bending, still deserve further studies.

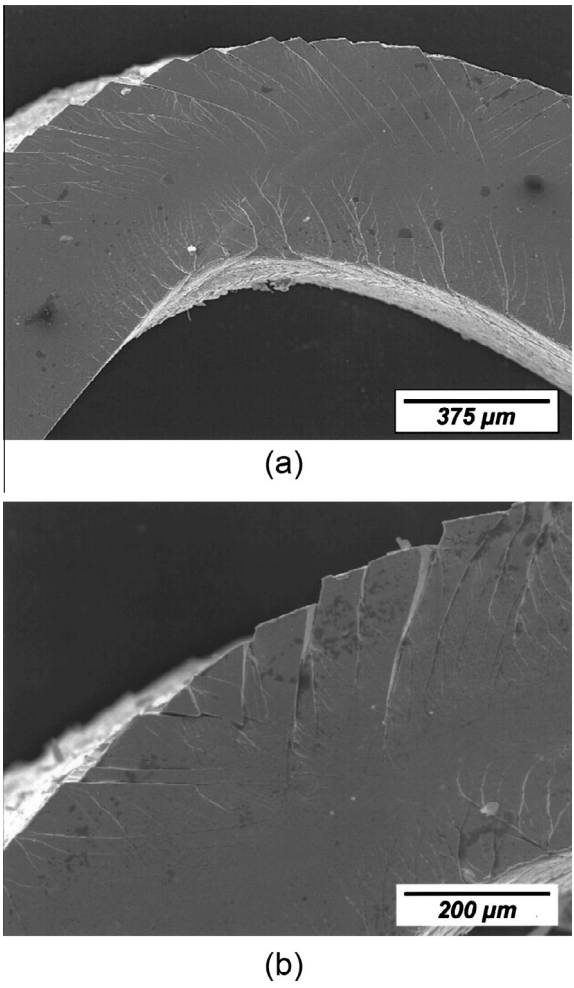

Fig. 9. SEM micrograph showing shear band patterns in a 0.5 mm thick plate of Vitreloy 106, bent over a mandrel with a radius of 1 mm. (reproduced from [120] ©2003. American Institute of Physics).

3.3. The general fracture behaviors

There are two types of fractures in engineering materials: brittle fracture and ductile fracture [19,20]. Brittle fracture, occurring only within elastic regime, is observed in most ceramics, oxide glasses and some brittle polymers. While ductile fracture, can be found in crystalline metals and alloys as they can dissipate fracture energy and block crack propagation with a significant plastic deformation regime. BMGs have a fracture ability that is intermediate between traditional brittle and ductile materials, and could dissipate some plastic energy in localized shear bands compared to that of oxide glasses, but lack strain hardening and intrinsic crack propagation barriers such as grain boundaries in crystalline metals and alloys. Depending on composition and loading conditions, BMGs display resultant fracture behavior, such as multiple fracture modes and various fractographs on fracture surfaces. The fracture toughness-strength data reported so far for BMGs bridge the gap between those brittle ceramics, tough metals and alloys [22]. These diverse fracture behaviors, on one hand, make BMGs model systems to investigate some critical issues in fracture mechanics; on the other hand, complicate the understanding of underlying fracture mechanism.

Under uniaxial tensile conditions, most monolithic BMGs (even for the toughest BMG reported [122]) will fracture catastrophically with almost zero macroscopic plasticity in the stress–strain curves (see Fig. 10) at room temperature. Only in few exceptions, such as in dynamic testing with high strain rates [123] or in nanoscale size samples [124] or some BMGs with low T_g, the tensile plasticity in BMG can be observed. Under stable loading geometries, such as uniaxial compression, however, some BMGs display plasticity before final fracture [90], as shown in Fig. 10, for a Zr-based BMG. The plasticity asymmetry in compression and tension indicates that the normal stress/pressure has an important effect on its flow and fracture behavior. In compression, deformation is mainly dominated by the shear banding process, which becomes unstable and evolves into crack along the shear band plane. The shear stability, closely related with plasticity of BMGs, depends not only on the intrinsic glassy states (such as structure, free volume content and elastic constant), but also on various extrinsic materials properties (such as sample size and geometry) and experimental factors (such as machine stiffness) [92,104]. For example, some Zr-based BMGs display unusual large room-temperature compressive plasticity or even super large plasticity without final fracture due to the formation of multiple shear bands by carefully tuning their composition and elastic constant [125] or introducing nanoscale inhomogeneity in their structures [126]. The improved plasticity could also be achieved by reducing the sample size or aspect ratio or simply changing testing machine [104]. In this regard, the use of ductility, i.e. the plastic strain before final fracture, as an intrinsic measure to toughness of BMGs is ambiguous. Instead, the fracture toughness concepts and methods should be used in BMGs to measure the intrinsic crack resistance during fracture. In addition to loading condition, the fracture behavior of BMGs also strongly depends on temperature, pressure and loading rate, etc. Their effects on fracture stress, fracture toughness and fracture morphology will be discussed in details in following sections.

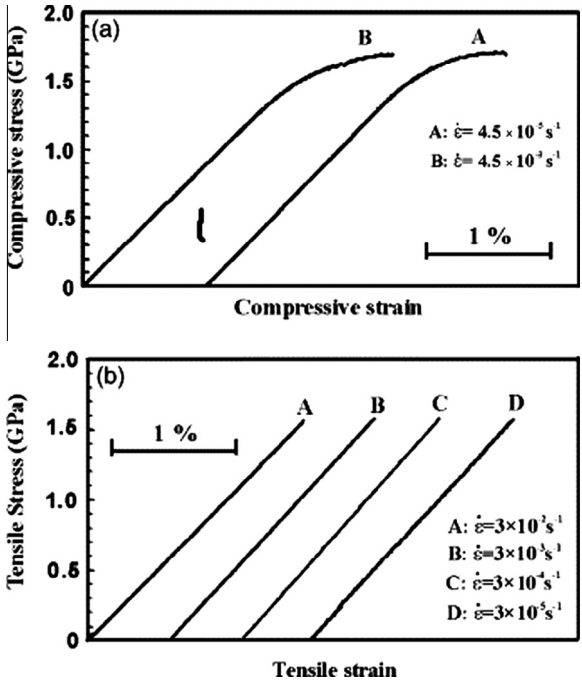

Fig. 10. The typical stress–strain curves for a Zr-based BMG under uniaxial compression (a) and tension (b) tests at different strain rates (reproduced from [90,124] with permission. ©2003. Elsevier).

3.4. Fracture modes

After final fracture, BMG specimens appear in different shapes and forms, from which the fracture modes can be defined and classified. Fracture forms and shapes of BMGs are determined by their composition, structure states, and loading conditions. It should be noted that the fracture mode used here is different from the crack opening modes discussed in Section 2. The sample appearance after fracture is a general result of the mixture of three basic crack modes and is determined by their partitions during fracture. We summarized and discussed these fracture modes as following:

3.4.1. Shear fracture mode

Shear fracture mode is usually observed in compression and tension tests of BMGs where the final fracture occurs along the shear plane declined to the applied loading axis, as shown in Fig. 11. Different from crystalline alloys, the shear plane deviates from the maximum resolved shear stress plane (45°) with the shear angle $45^\circ < \theta^T < 90^\circ$ under tension and $0^\circ < \theta^C < 45^\circ$ under compression [127–129]. This indicates that the failure of BMGs is not only controlled by the deviatoric stress,

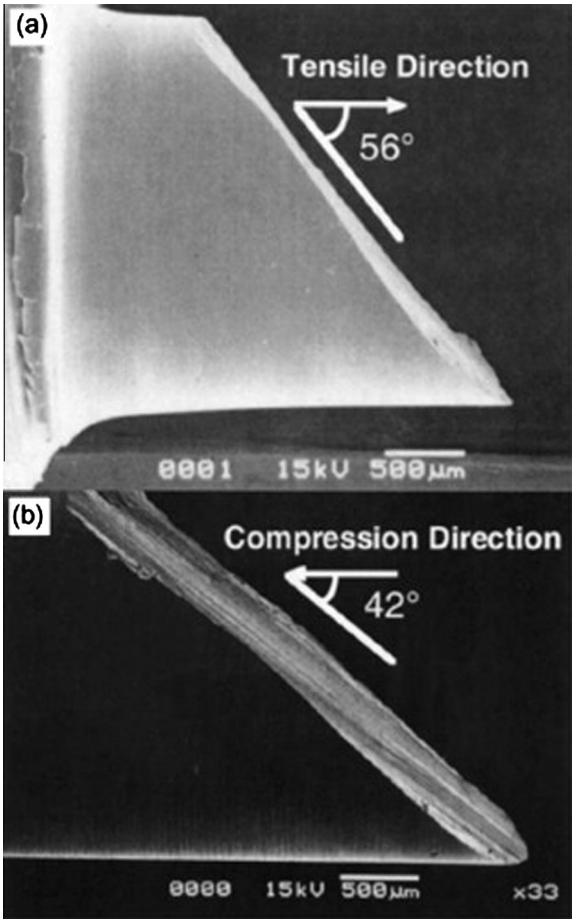

Fig. 11. The side view of a $Pd_{40}Ni_{40}P_{20}$ BMG after shear fracture in tension (a) and compression (b) respectively. The different shear angle can be seen: 56° and 42° for tension and compression, respectively (reproduced from Ref. [127] with permission. ©2002. Elsevier).

but also by pressure or normal stress. It is emphasized that such deviation from 45° is not symmetrical, as the tensile stress results in a more remarkable deviation ($> 5°$) than that in compression case ($< 5°$) (see Table 1), implying the normal stress effect in tension is much more pronounced than that in compression. Consequently, the traditional failure criteria such as Tresca or von Mises criteria [130] describing the plastic flow and fracture of crystalline alloys cannot be applied to shear fracture in BMGs, and Mohr–Coulomb or other criteria incorporating the effect of normal stress have to be considered [90,131]. Generally, the shear fracture mode often appears in ductile BMGs (such as those based Zr, Cu, Ti and noble metals) and the fracture arises from the shear instability along one dominant shear band (mode II crack instability). After fracture, vein patterns with some liquid features can be observed on the fracture surfaces, indicating significant temperature rise, local plasticity and local softening in the shear fracture process [28,132].

3.4.2. Cleavage mode

Cleavage mode involves breaking up of BMG along the plane perpendicular to the applied tensile stress, and often occurs in tension or bending of some brittle Mg-, Rare earth-, and Fe-based BMGs [24,25,133]. Clearly, mode I crack plays a dominant role in this mode. However, the cleavage in BMGs is different from that in crystals. The cleavage in crystals usually occurs along a well-defined crystallographic plane with weak atomic bonding [134], which leads to an extremely smooth and flat fracture surface even at the atomic scale. In contrast, BMG lacks of such well-defined lattice plane to cleavage, and when the cleavage occurs, the crack usually propagates in a wavy way, resulting in relatively rough fracture surfaces. According to surface roughness, the fracture surface can be roughly divided into three distinct regions, i.e., mirror, mist and hackle region [133], as shown in Fig. 12(a) [24,133]. These regions are similar with that in other brittle glassy materials such as covalent silicate glasses and polymer glasses. The characteristic fractographs associated with these regions will be

Table 1
The fracture stress and angle in tension and compression of different metallic glasses [128]. σ^T and σ^C are the fracture stress in tension and compression, respectively. The θ^T and θ^C is the angle between the fracture plane and the loading axis in tension and compression, respectively. As they were mostly measured from the SEM micrographs of failed sample, the errors for these angle values are estimated as 1–2°.

Composition	Tensile failure		Compressive failure		Ref.
	σ^T (GPa)	θ^T (°)	σ^C (GPa)	θ^C (°)	
$Pd_{77.5}Cu_6Si_{16.5}$	1.44	50	1.51	45	[147]
$Pd_{78}Cu_6Si_{16}$	1.45	55	1.54	45	[283]
$Pd_{40}Ni_{40}P_{20}$	1.46	50	1.78	41.9	[284]
	1.6	56	1.74	42	[127]
$Zr_{40.1}Ti_{12}Ni_{9.3}Cu_{12.2}Be_{26.4}$	1.98	51.6	2.0	40.8	[148]
$Zr_{41.2}Ti_{13.8}Ni_{10}Cu_{12.5}Be_{22.5}$	1.8	55	2.0	44	[135]
	1.8	56	1.95	42	[285]
	1.89	–	1.9	–	[286]
$Zr_{52.5}Ni_{14.6}Al_{10}Cu_{17.9}Ti_5$	1.65	54	1.88	44	[52]
	1.66	60	1.82	42.5	[287]
	1.66	56	1.76	42	[288]
$Zr_{55}Al_{10}Cu_{30}Ni_5$	1.53	53	1.77	41	[289]
	1.6	–	1.8	–	[290]
	1.51	–	1.82	–	[128]
$Zr_{56.2}Ti_{13.8}Nb_{5.0}Ni_{5.6}Cu_{6.9}Be_{12.5}$	1.487	59	1.669	45	[291]
$Zr_{57.5}Nb_5Cu_{15.4}Ni_{12.6}Al_{10}$	1.2	–	1.8	–	[117]
$Zr_{59}Cu_{20}Al_{10}Ni_8Ti_3$	1.58	54	1.69	43	[90]
$Zr_{60}Al_{10}Cu_{20}Pd_{10}$	1.68	55	1.88	45	[5]
$Zr_{60}Al_{10}Cu_{25}Ni_5$	1.63	–	1.76	–	[289]
$Co_{80}Nb_{14}B_6$	2.88	–	3.47	–	[284]
$Cu_{60}Zr_{30}Ti_{10}$	2.0	–	2.15	–	[292]
$Cu_{60}Hf_{25}Ti_{15}$	2.13	–	2.16	–	[292]
$Pd_{80}Si_{20}$	1.33	90	–	–	[293]
$La_{62}Al_{14}(Cu,Ni)_{24}$	0.55	90	0.56	40–45	[219]

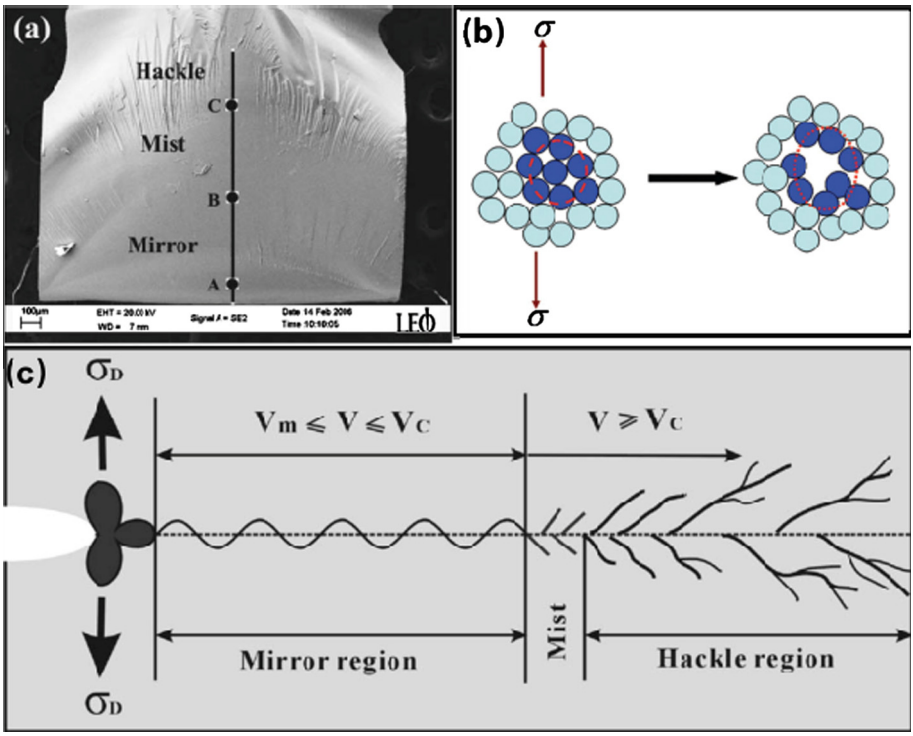

Fig. 12. (a) The typical cleavage fracture surface shown by a Fe-based BMG where mirror, mist and hackle region can be observed (reproduced from Ref. [24] with permission. ©2003. American Institute of Physics). (b) The schematic illustration the tension transformation zone under tension stress (reproduced from Ref. [135] with permission. ©2008. Taylor & Francis). (c) The illustration of dynamic cleavage crack propagation showing the correlation between three typical regions and crack velocity (reproduced from Ref. [24] with permission. ©2003. American Institute of Physics).

discussed in details in Section 5. Mechanically, the formation of these regions is due to energy dissipation associated with crack instability in the dynamic fracture process. With increasing crack propagation velocity, the dynamic elastic energy, which is much larger than the static elastic energy stored, has to be dissipated to create much larger area of fracture surfaces accomplished by the crack waving, branching or bifurcation [see Fig. 12(c)] [24]. The initial featureless mirror-like region becomes misty and then evolves into a rough hackle region with increasing crack propagation velocity. Atomistically, the cleavage fracture mechanism of BMGs is much different from those of covalent glasses. Due to the metallic characteristics, atomic bonds in BMGs can be broken and reformed in the atomic scale, without substantial concerns for the rigidity of bond angles in a covalent solid [8], or the charge balance in an ionic solid. Thus, the crack in the tip during the cleavage of BMGs may not advance simply by the atomic decohesion in tension. In general, the inelastic shear of local atomic clusters or the operation of flow units around the crack tip will dominate the process, leading to local softening and formation of plastic process zones. For some brittle BMGs, cleavage has also been proposed to occur by preferentially breaking the local atomic clusters with the high free volume content. These atomic clusters that could directly break up under the tension stress are termed as the "tension transformation zones" (TTZs) [135] [see Fig. 12(b)]. Through TTZs, the energy is mainly dissipated by forming new surfaces, and their coalescence forms a path of a quasi-cleavage crack. The inherent competition of TTZs and STZs ahead of the crack tip is believed to be responsible for the transition of the energy dissipation mechanism from the local softening to the quasi-cleavage, which has been observed in the dynamic fracture of a tough $Zr_{41.2}Ti_{13.8}Cu_{10}Ni_{12.5}Be_{22.5}$ (Vitreloy 1) BMG [135].

3.4.3. Fragmentation mode

Fragmentation mode has been frequently observed in compression of very brittle BMGs like Mg-, Sr-, Fe-, Co-based BMGs [136–138], where the sample splits or breaks into fine particles or powders after emitting a "bomb-blast-like" sound during fracture. Typical appearance of the fractured sample is shown in Fig. 13(a). The characteristics and mechanism of this fracture mode have been investigated in details by Zhang et al. [138] in compression of Co-based BMGs. They find that the fractured sizes of particles or pieces are uniform and usually less than 50 μm. From SEM picture of some relatively large particles, many small pits, corresponding to fracture sites, can be found on the surfaces of the broken particles. These fracture sites radiate from the center toward to the outer edge as shown in high magnification SEM images in Fig. 13(b). A clear core indicated by arrow can be seen in the center of each fracture site, indicating the fracture sites in the fragmentation has gone through the nucleation and rapid growth processes. The surfaces of these fracture particles are smooth without veins and traces of local melting, suggesting a typical cleavage fracture during fragmentation [103]. The fragmentation mode can be viewed as a variety of the cleavage fracture. The slight difference between the two fracture modes lies in that the cleavage simultaneously occurs in different sites in the fragmentation rather than in one plane. To describe the fragmentation process, a new parameter of fragmentation coefficient, F_n, is defined as the ratio of the summed area of new surfaces A_n to the area of the original surface A_0 [103]: $F_n = A_n/A_0$. Normally, F_n increases if the sample breaks into more particles, and F_n could be used as a measure of the fragmentation degree of brittle fracture for a given BMG. Shear fracture can be regarded as a special failure mode with a fragmentation coefficient $F_n = 0.28$, which is the lowest value among all the fragmental fracture modes [138]. The F_n relates to the surface energy of γ by:

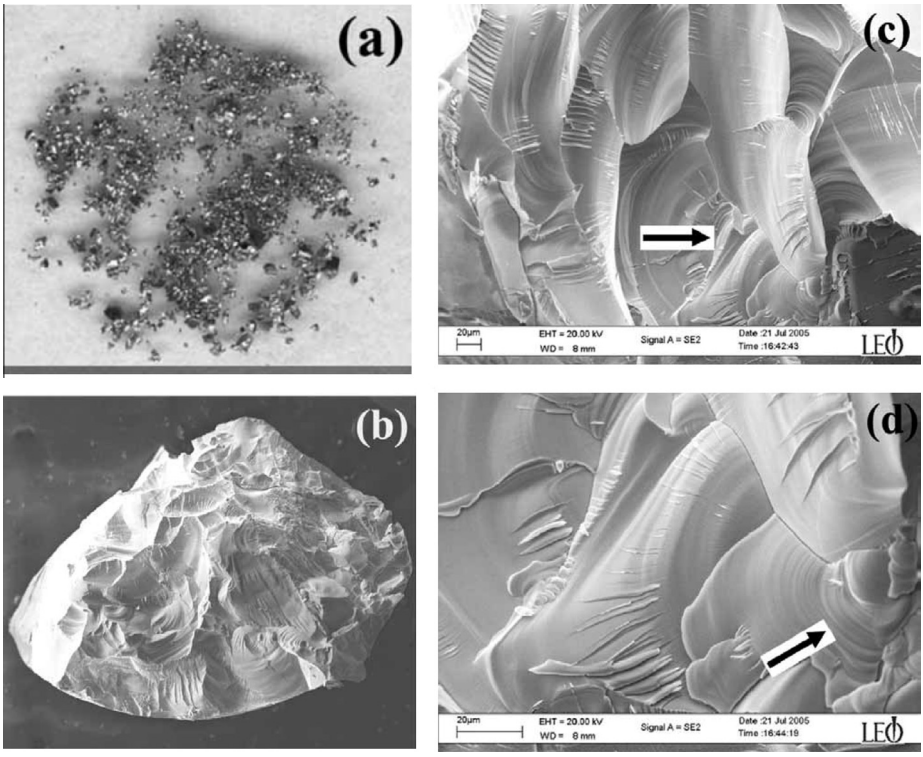

Fig. 13. The fragmentation fracture of a Co-based BMG. (a) The small pieces or particles after the fragmentation. (b–d) The fracture surface of the particle during the fragmentation indicating the radiating cracking (reproduced from Ref. [138] with permission. ©2006. Taylor & Francis).

$$\gamma = \frac{\eta \sigma_F^2 V_0}{2F_n E A_0}, \tag{12}$$

where σ_F is the fracture strength of BMGs, η is the efficiency of the stored elastic energy in creating the new surface during fracture. Eq. (12) shows that the surface energy γ is inversely proportional to F_n (or the number of broken particles), and the sample tends to break into more pieces upon compression if the material has a lower surface energy. As the lower surface energy relates to a lower theoretical cleavage strength ($\sigma_0 = \sqrt{E\gamma/a_0}$, a_0 is the equilibrium distance of atomic pairs), and the critical shear strength τ_0 is essentially unaffected, the fragmentation mode tends to occur for a high ratio of $\alpha = \tau_0/\sigma_0$. The parameter α is called the fracture mode factor [129], which will be discussed in details in fracture criterion section.

3.4.4. Ductile fracture mode with necking instability

Ductile fracture mode with stable homogeneous elongation and subsequent necking instability before final rupture is usually observed in the tension of ductile crystalline alloys [139] or homogeneous viscous flow of BMGs at high temperatures close or above glass transition [8]. During the necking, material seems "pull apart" rather than cracking, and leaving rough surface. In this case, there is a large amount of energy dissipated into the plastic deformation process. At room temperature, BMGs seldom exhibit this fracture mode due to the severe shear localization in nanoscale shear bands. Recent studies [140] have revealed that BMGs are capable of homogeneous plastic deformation without shear banding under special conditions and thus the fracture with necking instability is possible. The significant tensile ductility and extensive necking behavior have been demonstrated by *in-situ* tensile TEM test [124] of a Zr-based metallic glass with the order of 100 nm (see Fig. 14). This finding indicates that metallic glasses are not intrinsically brittle (especially when their size are reduced into micro-or nanometer scales) but may have potential applications as precise micro-devices and

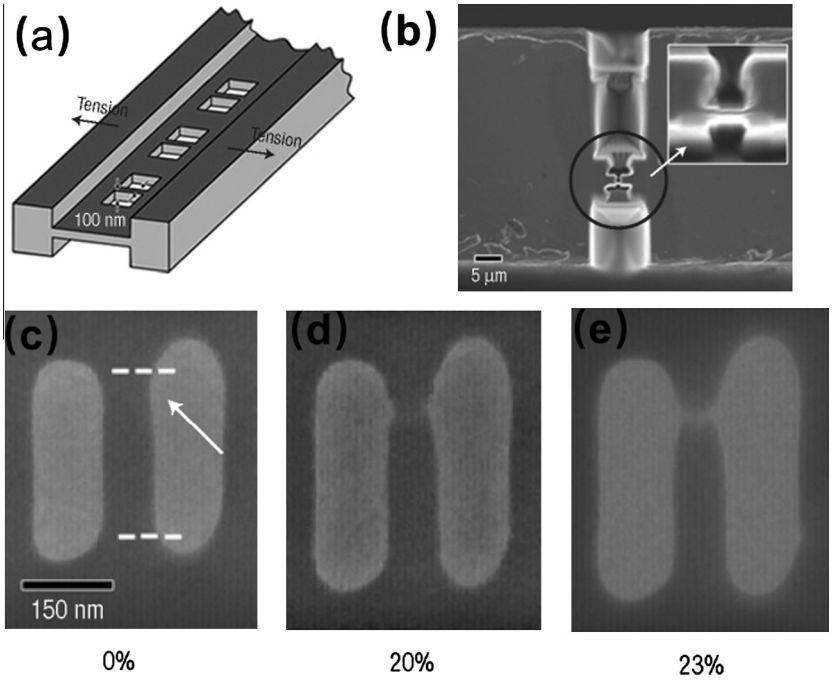

Fig. 14. (a) The schematic diagram of the submicrometer sample in tension tests fabricated by FIB. (b) The SEM images for the small-sized sample from the side view. (c and d) The necking fracture process of the sample observed during the in-situ tensile TEM tests (reproduced from Ref. [124] with permission. ©2007. Nature Publishing Group).

thin-films. The physical mechanism for the large ductility and necking instability in small-sized MGs is still elusive. It is suggested that the mechanism relates to the interplay between sample size and shear banding process, and once the sample size is reduced down to the critical value of shear band size, the shear band cannot be formed, leading to homogeneous plastic flow process and necking instability [140]. The large tensile ductility and necking instability are also observed in some BMG matrix composites [141–143], where the well-designed crystalline dendrites effectively stabilize the glass against the catastrophic failure with limited extension of shear bands, resulting in the formation of dense multiple shear bands and relatively homogeneous deformation before final fracture.

Based on above discussions, we can see that fracture modes correlate well with fracture toughness and fracture morphology, and can be used as a rough estimation for the brittleness of BMGs. However, fracture mode is also influenced by various extrinsic factors and loading conditions, and not invariant for a specific composition. For example, when temperature is near the glass transition, almost all BMGs (including those extremely brittle) will fracture in a ductile mode with necking instability in tension. In contrast, high loading rate renders BMGs become "brittle", and the fracture of ductile BMGs will transform from shear mode at quasi-static strain rates to fragmentation or cleavage mode in high strain rate tests [135].

3.5. Fracture strength

Fracture strength is defined as the ultimate stress at which the materials fracture catastrophically or cracks begin to propagate unstably [19,20]. Although the fracture strength does not reflect the intrinsic fracture ability of materials, it is still an important parameter to evaluate and understand fracture behavior of materials. Due to the lack of strain hardening, BMGs can maintain almost a constant invariant flow stress until catastrophic failure [144]. The fracture strength in some BMGs is thought to be roughly equal to the yield strength, and the use of two strength concepts in some MG literatures is often conflated. However, it should be pointed out the fracture and the plastic yielding are two physically distinct processes. The first is associated with the formation of crack, while the latter with the formation of shear bands, is irrespective of whether they may occur at the same stress level or near simultaneously. Due to stress concentration around the flaws, some brittle BMGs [8,138] could fracture, particularly in tension and bending, in the elastic regime before the global plastic yielding. The fracture strength in such cases is much lower than the plastic yield strength. In general, BMGs usually have much higher fracture strength than that of conventional engineering materials as shown in Table 1, and this is one of attractive attributes that draw much attention in past decades. Table 1 also shows that yield strength is asymmetric between tensile and compressive stress state: the tensile strength is usually 10–20% lower than the compressive strength, indicating the effect of normal stress state on the strength.

3.5.1. Correlation between fracture strength and Young's modulus in BMGs

The elastic moduli of BMGs has been found to well correlate with glass transition temperature, and mechanical properties, and even liquid fragility [18,145]. These correlations could assist in understanding of glassy nature as well as in designing new BMGs with controllable properties [18]. It is generally believed that there is no simple relationship between fracture strength and stiffness in elastically isotropic materials [146], and the reason is that when a conventional material fails under stress, the defects determine its fracture strength. This is not the case for BMGs. A clear correlation between fracture strength σ_f and Young's modulus E has been found in BMGs [19,56]. The data of σ_f and E for typical BMGs and other materials are summarized [18] and shown in Fig. 15 [146]. A linear scaling $\sigma_f \sim E/50$ can be found for BMGs [18,91], and the scaling slope is in the intermediate between the ideal materials without defects ($\sim$1/10) and ductile crystalline alloys ($\sim$1/50). As most BMGs have a nearly constant elastic limit of $\sim$2%, the linear relation $\sigma_f \sim E/50$ obtained from compression experiments comes from the fact that the fracture strength is roughly equal to plastic yielding strength due to the lack of work hardening ability of BMGs. Nevertheless, after careful examination, small but observable scatter or nonlinearity is found in the correlation for brittle and tough BMGs: for the brittle BMGs, the measured σ_f is randomly distributed around $\sigma_f \sim E/50$; while the σ_f of tough BMGs with marginal plasticity tends to be smaller than that expected from $\sigma_f = E/50$. The difference can be

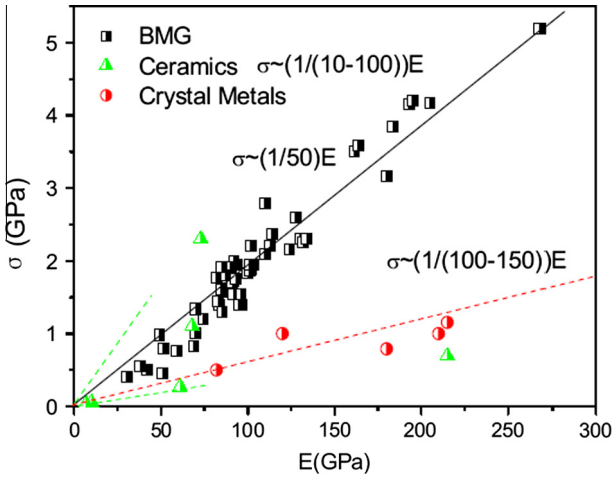

Fig. 15. The ultimate fracture strength (σ_f) versus Young's modulus (E) for various BMGs tested at room temperature. The data of conventional crystalline alloys and ceramics are also shown for comparison (reproduced from Ref. [146] with permission. ©2011. American Institute of Physics).

attributed to the fact that the fracture of brittle BMGs is dominated by the formation of crack surface while the fracture of tough BMGs may involve extensive plastic deformation ahead of the crack tip, and thus is generally understood from the extension of Griffith theory [92]. For brittle materials, the fracture strength and its fluctuation is expressed as $\sigma_f = \sqrt{2E\gamma_s/\pi(c+\xi)}$, where ξ is the fluctuation of the flaw size c due to preparation conditions, the surface energy γ_s is proportional to E. The effect of flaw size fluctuation on the fracture strength should be random in nature, which has been verified by the Weibull statistical analysis of fracture strength in experiments. In contrast, the fracture strength in tough BMGs is determined by $\sigma_f = \sqrt{E(2\gamma_s+\gamma_p)/\pi C}$, where C is the size of plastic fracture stress zone ranging from nanometer to micrometer length scales. The γ_p is much larger than γ_s, and σ_f is mainly dominated by γ_p/C, which contributes to the deviation from the linear scaling of the strength with respect to the moduli data [146]. As E also correlates with other properties [145] such as T_g and the fragility m in BMGs, it is expected that the fracture strength is also related with these properties, which have not been experimentally explored yet.

3.5.2. Temperature, loading rate and pressure dependence of strength

Fracture strength is a complex materials property which could be influenced by intrinsic materials parameters such as inter-atomic interactions (reflected by elastic constants), structures including defects, and various extrinsic factors such as preparation, loading conditions and modes, sample geometry, and flaw size. However, few studies concerning the effects of temperature, loading rate and pressure on fracture strength in BMGs have been performed yet. Instead, most studies in BMG literatures are focused on the effect of these factors on yield strength, partially due to the yield strength is an intrinsic property of a material while the fracture strength is largely affected by extrinsic flaws. It has been found that the yield strength decreases with a temperature dependence $(T/T_g)^{1/2}$ from STZ theory assuming that the activation enthalpy to initiate the shear event is a quadratic function of the shear stress [46]. The temperature dependence can well capture the experimental strength data for various BMGs at different temperatures [8]. Johnson and Samwer also derived a similar temperature dependence of $(T/T_g)^{2/3}$ based on the Frenkel scheme and the fold catastrophe theory [61]. The strength is also weakly related with strain rate $\dot{\gamma}$ in a form of $-\ln(\dot{\gamma})^{1/2}$ or other similar form in BMGs [9], although loading rate could significantly affect their fracture mode and morphology. As shown in Fig. 16(a), a rate-independent strength is obtained over at least six orders of magnitudes,

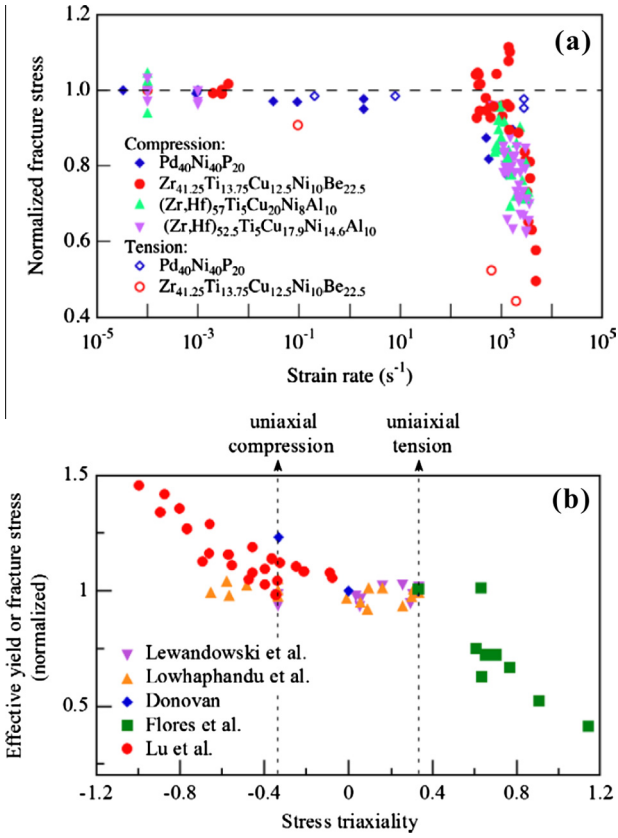

Fig. 16. (a) The variation of fracture stress for a number of metallic glasses tested over a broad range of rates. (b) The experimental data illustrating the effect of pressure on the yielding/fracture stress of metallic glasses with data from different research groups (reproduced from Ref. [8] with permission. ©2007. Elsevier).

covering the entire quasi-static rate range and up to the range of low-velocity imparts. Although the fracture strength is almost equal to the yield strength in most BMGs at room temperature and quasi-static rates, it is generally regarded that the two strengths have different temperature and rate dependences. According to Ludwik–Davidenkow–Orowan hypothesis, fracture strength is less sensitive to temperature or loading rate than that of yield strength. This leads to thermal- or rate-induced ductile-to-brittle transition which will be discussed in Section 4.3.

Pressure or normal stress has effects on plastic flow and fracture of BMG. Table 1 shows that tensile strength is usually 10–20% less than compressive strength for the same BMG. The difference is more significant than that of crystalline alloys indicating that the plastic flow and fracture is not exclusively dependent on the deviatoric part of the stress tensor. There have been intensive studies on the effect of pressure on fracture of BMGs by either directly superimposed the hydrostatic pressure on mechanical testing [147,148] or other indirect methods such as testing under complex stress states [149–151]. Davis and Kavesh [147] performed compression and tension tests with imposed hydrostatic pressure (~6.5 kbar) on a $Pd_{77.5}Cu_6Si_{16.5}$ metallic glass, and observed that the incremental of the fracture strength with the hydrostatic pressure ($\Delta \ln \sigma / \Delta p \approx 5 \times 10^{-6}$ bar^{-1}) is relatively small and close to that of crystalline alloys. Lewandowski et al. [148,152] reported a weak pressure dependence of the fracture stress in Zr–Ti–Cu–Ni–Be BMG. The results obtained from indirect methods reported more significant pressure dependence of the flow and fracture strength. For instance, Flores and

Dauskardt [150] used compression and notched-bar tensile tests and the elastic stress analysis to show that the average failure stress decreases sensitively with increasing mean stress (i.e. rises with pressure), and the failure in metallic glasses appears to be considerably more sensitive to the tensile normal stress or negative pressure than to the compressive normal stress. The pressure dependence of yield strength seems to be more significant than that of fracture strength. For example, Lu et al. [149] conducted confined compression tests on $Zr_{41.2}Ti_{13.8}Cu_{12.5}Ni_{10}Be_{22.5}$, imposing large radial confinement stresses (up to 2 GPa) and resulting in hydrostatic pressure of 2.5 GPa. Their yield stress measurements are well fitted with a pressure-dependent Tresca criterion, giving a relatively large pressure coefficient in 0.6–2.7 GPa. Vaidyanathan et al. [151] examined the pressure sensitivity of the plastic flow of $Zr_{41.2}Ti_{13.8}Cu_{12.5}Ni_{10}Be_{22.5}$ using instrumented indentation method, and the complemented three-dimensional finite-element analysis of the Berkovich indentation with various constitutive relations. They used the Mohr–Coulomb criterion to fit the experimental and simulated results, and obtained a large pressure coefficient ($\alpha_n = 0.13$). Schuh et al. [8] summarized these experimental data in Fig. 16(b) for the stress triaxiality (proportional to $-p$, here p is pressure) dependence of the strength. These data, which are collected from various experiments involving different geometries and various alloys, and include both the yield and fracture strength, are significantly scattered. Nevertheless, a general downward trend can be found for the strength with the stress triaxiality and the fitting slope α_p in the range of 0.03–0.17. The value of α_p indicates a modest pressure sensitivity of the yield/fracture strength in BMGs, which is much lower than that of more strongly dilatant materials such as polymers (for which $\alpha_p \sim 0.2$) and granular materials (for which $\alpha_p \sim 0.3$ or even higher). From the mechanistic point of view, the modest pressure or normal stress dependence observed in BMGs points to an atomic-scale deformation mechanism that involves some degree of dilation [8].

3.5.3. The statistical properties of fracture strength of BMGs

When liquid is quenched into a glassy state, it is trapped in one of many possible megabasins in potential energy landscape and inhabits one of a range of infinitesimally different structural configurations. The mechanical response of BMGs is very sensitive to their cooling rate, thermal history, and extrinsic defects (e.g. inclusions, pores, etc.). The BMGs are then often considered as "brittle" or at least "macroscopically brittle" materials, which is structural materials flaw and extrinsic defects (e.g. inclusions, pores, etc.) sensitive and displays scatter and variability in their mechanical properties based on the statistical distribution of flaws. Therefore, statistical distribution and reliability of mechanical properties are important factors for practical applications. In the mechanical failure, the Weibull approach is commonly used to for evaluating statistical stability of fracture strength or toughness, especially for ceramics and brittle metals. According to the framework of Weibull theory, the fracture probability, P_f, for a given uniaxial stress σ, is described by the Weibull equation:

$$P_f = 1 - \exp\{-V[(\sigma - \sigma_u)/\sigma_0]^m\}, \tag{13}$$

where σ_0 is a scaling parameter, m is the Weibull modulus and V is a normalized volume of the tested sample. The parameter σ_u denotes the stress at which there is a zero failure probability and is usually taken to be zero. Wu et al. [105] used the approach to analyze the statistical distribution of the compression fracture strength of Zr-based BMGs with different ductility. They found that the intrinsically brittle BMG has a very high Weibull modulus of about 25, and the intrinsically malleable one have a value of 75. The Weibull modulus, m, reflects the degree of variation in the strength of the tested sample, and can theoretically range from 0 to ∞. The Weibull moduli for ductile crystalline metals and brittle engineering ceramic materials are in typical order of $\sim$100 and $\sim$5, respectively. The larger value of m represents a narrow range of strength dispersion. The high Weibull modulus of BMGs, especially the ductile one, encourages the use of BMGs in structural applications. Yu et al. [153] also analyzed the statistical distribution of compressive plasticity of a Zr-based BMG, and revealed that the plasticity is less stable ($m \sim 5$) compared to the strength of alloy ($m \sim 42$), and the large variation of plasticity is attributed to the different fraction and distribution of free volume in metallic glass. These results are useful for understanding the large degree of data scattering reported in plasticity of BMGs.

3.6. Failure criterion

BMGs possess high strength but fail in a brittle manner, which is similar with other high-strength brittle materials such as ceramics, intermetallics, rocks, and concretes. In addition, BMGs display multifarious fracture features which are completely different from traditional crystalline alloys. Therefore, a unified failure criterion to describe these features is essential both for understanding the fracture mechanism of BMGs and designing new high-strength BMGs. Many failure criteria have been widely used for the yielding or failure of brittle materials. Among them, the maximum normal stress criterion, the Tresca criterion, the von Mises criterion, and the Mohr–Coulomb criterion [154,155] are the most commonly used. These criteria will be briefly summarized below.

The maximum normal stress criterion predicts that fracture happens when the maximum normal stress of a plane σ_{max} reaches a critical normal fracture stress σ_0 of the material, i.e. $\sigma_{max} \geqslant \sigma_0$. As σ_{max} always occurs on the 90° plane of the specimen, this failure criterion results in fracture angle $\theta_T = 90°$ with respect to applied shear stress under uniaxial tension. In contrast, the Tresca criterion suggests that yielding or failure begins when the maximum shear stress of a plane τ_{max} reaches a critical value, i.e. $\tau_{max} \geqslant \tau_0$ where τ_0 is the critical shear fracture stress of material. This criterion is often used to describe yielding or failure of crystalline materials. According to this criterion, tensile shear failure will occurs at $\theta_T = 45°$ as τ_{max} is on a 45° plane with respect to the tensile stress axis. Another classical criterion for describing the failure of crystalline materials is the von Mises criterion, where the fracture is associated with the second deviatoric stress invariant J_2. Under uniaxial tension condition, the criterion can be expressed as [129]

$$\sigma^2 + 3\tau^2 \geqslant 3Y^2, \tag{14}$$

where Y is a material constant, σ and τ are the normal and the shear stresses of a shear plane, respectively. σ and τ are related to tensile stress σ_T by $\sigma = \sigma_T \sin^2\theta$, $\tau = \sigma_T \sin\theta\cos\theta$ with θ being the angle of the shear plane with respect to the tensile axis. And the tensile shear plane always occur for $\theta = 60°$ according to this criterion. The Mohr–Coulomb criterion [154] suggests a combination influence of the shear stress and the normal stress on the shear failure and is expressed as:

$$\tau + \mu\sigma \geqslant \tau_0, \tag{15}$$

where μ is the friction coefficient on the shear plane. According to the criterion, the effective yield or fracture stress increases for the compression and decreases for the tension due to the effect of normal stress (the term $\mu\sigma$ is negative for compression and positive for tension), and results in a deviation of the shear fracture plane from the maximum shear stress plane, namely, $0 < \theta_C < 45°$, $45° < \theta_T \leqslant 90°$.

The four classic criteria above can describe the different shear modes of BMGs, but neither of them could explain these behaviors in a unified way. Especially in tension, BMGs lacks a well-defined shear fracture plane as in crystalline alloys (for example, slip planes), and this leads to an arbitrary shear plane with the angle $45° < \theta_T \leqslant 90°$. Obviously, the Tresca criterion and von Mises criterion are invalid as they could only explain the case for $\theta_T = 45°$ or $\theta_T = 60°$. The Mohr–Coulomb seems can describe shear failure at arbitrary angles, but fails to explain the case for $\theta_T = 90°$. To uniformly explain tensile fracture behavior of BMGs, Zhang et al. [129] proposed an ellipse criterion by noting the fact that the ratio of τ_0/σ_0 is not necessary a constant such as in von Mises criterion $\tau_0/\sigma_0 = \sqrt{3}/3$ as [94]:

$$\frac{\sigma^2}{\sigma_0^2} + \frac{\tau^2}{\tau_0^2} \geqslant 1, \tag{16}$$

where, $\alpha = \tau_0/\sigma_0$ can be taken an arbitrary value, and the dependence of the shear stress on the normal stress is not linear as in Mohr–Coulomb criterion. As shown in the Mohr circle in Fig. 17(a)–(c), the shape of the ellipse is closely related with the factor α. And θ_T and σ_T also depend on α as shown in Fig. 17(d). When $0 < \alpha = \tau_0/\sigma_0 < 2/\sqrt{2}$, θ_T ranges from 45° to 90°, which is consistent with the Mohr–Coulomb criterion. Particularly, $\theta_T = 60°$ for $\alpha = \tau_0/\sigma_0 = 3/\sqrt{3}$, corresponding to the von Mises criterion. When $\alpha = \tau_0/\sigma_0 \geqslant 2/\sqrt{2}$, the tensile fracture will occurs along the plane perpendicular to the tensile axis, i.e., $\theta_T = 90°$, indicating that the maximum normal stress criterion is also a

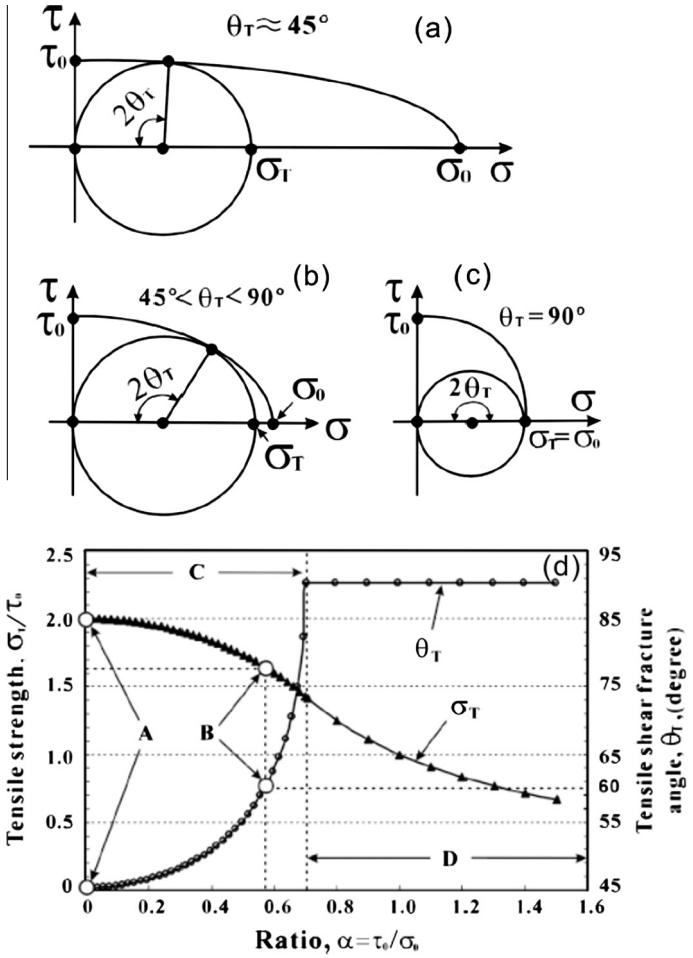

Fig. 17. Schematic illustration of ellipse criterion at different conditions: (a) $\alpha = \tau_0/\sigma_0 \to 0$ or $\sigma_0 \to \infty$, and $\theta_T = 45^\circ$; (b) $0 < \alpha = \tau_0/\sigma_0 < \sqrt{2}/2$; and (c) $\alpha = \tau_0/\sigma_0 \geqslant \sqrt{2}/2$, and $\theta_T = 90^\circ$. (d) Dependence of tensile fracture strength σ_T and tensile fracture angle θ_T on the ratio $\alpha = \tau_0/\sigma_0$ according to the ellipse criterion (reproduced from Ref. [129] with permission. ©2007. American Physical Society).

special case of the ellipse criterion. When $\alpha = \tau_0/\sigma_0 \to 0$ or $\sigma_0 \to \infty$, θ_T is quite close to 45°, and this is equivalent to the Tresca criterion. Thee four well-established classic failure criteria are the special cases of the ellipse criterion in terms of the variation of $\alpha = \tau_0/\sigma_0$. Zhang and coworkers [156] designed a series of tensile tests on BMG specimens with notches of different inclined angles [see Fig. 18], and a wide range of normal stresses on the fracture plane were obtained. The results showed that the critical fracture stress state of the studied BMGs can be precisely described by the ellipse criterion. Furthermore, they find that the ellipse criterion has the capability to predict various contributions of the normal stress effect on the tensile fracture behavior of a large number of compositionally different BMGs, suggesting the ellipse criterion could be a unified tensile failure criterion in BMGs.

In fact, the ratio $\alpha = \tau_0/\sigma_0$ reflects the difference in the bonding property of different materials, and controls the macroscopic fracture modes of materials [129]. Most materials can be divided into three types according to the variation of $\alpha = \tau_0/\sigma_0$: (i) the ductile crystalline materials with a low shear strength and $\alpha = \tau_0/\sigma_0 \to 0$, (the Tresca criterion applies). (ii) High strength materials including BMGs and nanostructured materials with the ratio $\alpha = \tau_0/\sigma_0$ usually in the range of 1/3–2/3. (iii)

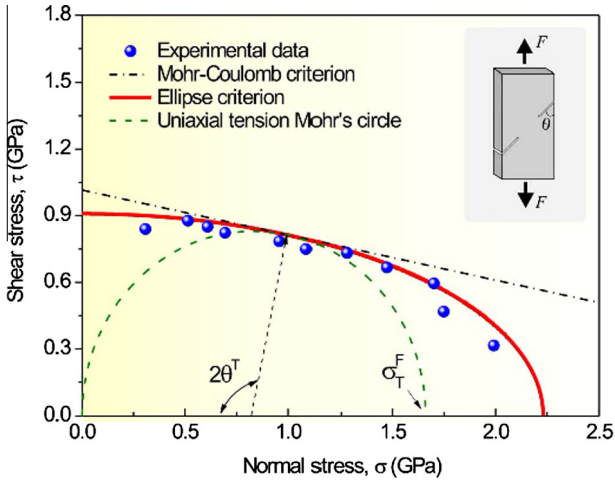

Fig. 18. Experimental data illustrating that the ellipse criterion can well predict the tensile fracture behavior of $Zr_{52.5}Cu_{17.9}Ni_{14.6}Al_{10}Ti_5$ BMG and the inset is the schematic diagram of the designed sample with the inclined notch (reproduced from Ref. [156] with permission. ©2007. American Institute of Physics).

Extremely brittle materials with very high hardness at $\alpha = \tau_0/\sigma_0 \geqslant 2/\sqrt{2}$ such as the rock, intermetallics and ceramics, where the cleavage fracture mode is usually observed.

The ellipse criterion only applies to the case of tensile stress state, i.e., $\sigma_1 + \sigma_2 > 0$, where σ_1 and σ_2 are the maximum and minimum principal stress, respectively. To explain the fracture behavior of BMGs under different various stress conditions, Qu et al. [156] proposed a more general failure criterion based on the ellipse criterion as:

$$\tau^2 + \alpha^2\beta\sigma^2 = \tau_0^2, \tag{17}$$

here, $\alpha = \tau_0/\sigma_0$, reflects the effect of intrinsic factor such as composition and microstructure on the fracture behavior, and β is a parameter describing the effect of extrinsic factors such as the temperature and strain rate [156]. At room temperature and quasi-static strain rates, the β is different for tensile and compressive stress states. For tensile stress state, $\beta = \beta_T = 1$, and the criterion has the same form with the original ellipse criterion of Eq. (16). For compressive stress states, $\beta = \beta_C < 0$ and $|\beta_C| < \beta_T = 1$ due to the fact that the compressive normal stress state always plays a weaker role in the failure of BMGs than that of the tensile normal stress [150,157]. The value of β_C can be achieved from the shear angles θ_C and θ_T by performing the uniaxial tension and compression tests: $\beta_C = (1 - \cot^2\theta_C)/(1 - \cot^2\theta_T)$. They claim that the fracture behavior of BMGs both under compressive and tensile stress states can be uniformly described by this general criterion [156].

It is noted that the physical origin underlying these failure criteria is still poorly understood due to the complicated atomistic structure and bonding nature of BMGs. Recently, by carrying out the interaction analysis on a virtualized cohesive interface based on the nature of short range order (SRO) in metallic glasses, Chen et al. [128] derived a similar criterion with Eq. (16), where all factors involved in the criterion can be expressed as functions of parameters in describing the atomic structure and potentials of metallic glasses. The work sheds lights on the underlying physics of the failure criterion in metallic glasses.

4. Fracture toughness

Fracture toughness is a measure of crack resistance or damage tolerant ability of materials, which plays a critical role in understanding the fracture mechanism of materials and designing structural components in engineering materials. For BMGs, despite extensive studies, the factors which control

fracture toughness as well as intrinsic correlation between toughness and other properties in BMGs are unclear yet. This is largely attributed to the lack of good-quality BMG specimens with sufficient large sizes and quantities and a typical "microstructure" (such as dislocation and grain boundary in crystalline materials). Many factors such as sample geometry, cooling rate used during BMG preparation, and residual stress and structure states, and minor addition in the specimen also have significant influence on the fracture toughness of BMGs. Precise quantification and generalization of these factors are not usually straightforward [22]. In this section, we attempt to summarize and discuss these issues and the research progress in characterizing the fracture toughness in BMGs.

4.1. Fracture toughness measurement and value of BMGs

4.1.1. Procedure for fracture toughness measurement

As discussed in Section 2, many parameters including the fracture energy G_C, the critical stress intensity K_C, the J-integral and the CTOD are used in the measurement of fracture toughness. These parameters are developed for different kinds of materials and are closely connected each other. For BMGs, the most commonly used fracture toughness parameter is K_{IC}, and only in few cases G_{IC} (for very brittle BMGs) and the J_{IC} (for extremely tough BMGs) are used. The standard fracture toughness K_{IC} tests involve large-size notched specimens (generally with a thickness larger than 2 mm) with fatigue pre-crack. The shape of the specimen, the dimensions of the notch and the fatigue pre-cracking procedure have to strictly conform to the ASTM E399. The recommended specimens for the plain strain fracture toughness K_{IC} test are the three-point bend single-edge notched (SENB) specimen, compact-tension (CT) specimen, disk-shaped compact-tension (DCT) specimen, arc-shaped tension (AT) specimen and arc-shaped bend (AB) specimen [38]. The frequently used specimens are SENB and CT, and their geometries are shown in Fig. 19 [158]. A sharp crack is also required for specimens as the fatigue pre-cracking. The initial allowed crack size a (i.e. total size of notch plus the fatigue crack) is $0.45W < a < 0.55W$, where W is the sample width. The specimen is monotonically loaded until the failure, and the load and crack-opening displacement is recorded. The conditional fracture toughness K_Q can be calculated from the standard equations in ASTM E399. For the SENB specimen, the equation is expressed as [42]:

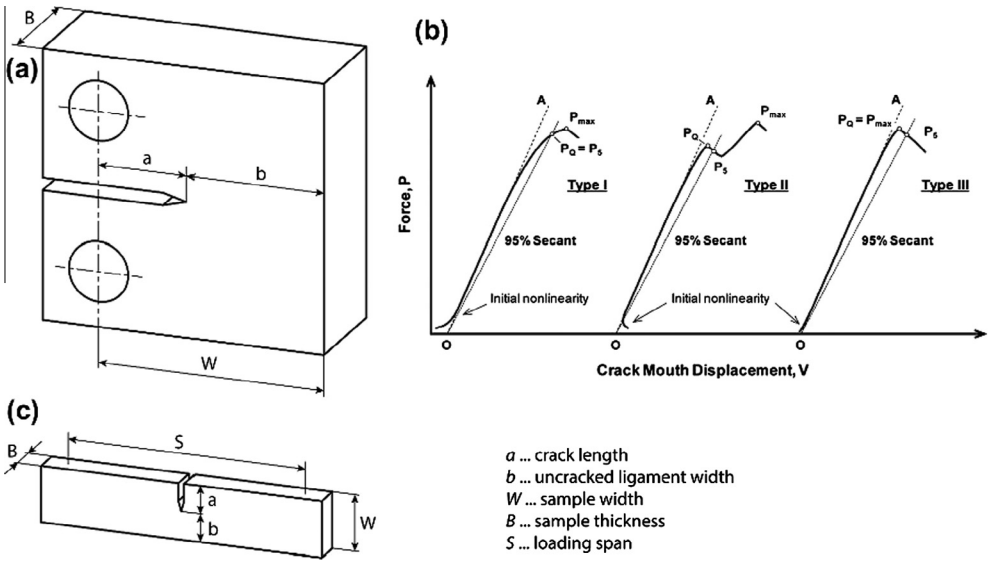

Fig. 19. Tested specimen geometries, showing the nomenclature of their dimensions and failure types by ASTM standard E399. (a) CT specimens as well as (c) SENB specimens. (b) Three types of load–displacement curves with the critical load P_Q defined for each type curve (reproduced from Ref. [158] with permission. ©2014. Elsevier).

$$K_Q = \frac{P_Q S}{BW^{3/2}} f\left(\frac{a}{W}\right), \tag{18a}$$

$$f\left(\frac{a}{W}\right) = 3\sqrt{\frac{a}{W}} \cdot \frac{1.99 - \left(\frac{a}{W}\right)\left(1 - \frac{a}{W}\right)\left[2.15 - 3.93\frac{a}{W} + 2.7\left(\frac{a}{W}\right)^2\right]}{2\left(1 + 2\frac{a}{W}\right)\left(1 - \frac{a}{W}\right)^{2/3}}, \tag{18b}$$

While for CT specimen, the equation is [42]:

$$K_Q = \frac{P_Q}{BW^{1/2}} f\left(\frac{a}{W}\right), \tag{19a}$$

$$f\left(\frac{a}{W}\right) = \frac{\left(2 + \frac{a}{W}\right)}{\left(1 - \frac{a}{W}\right)^{3/2}}\left[0.886 + 4.64\left(\frac{a}{W}\right) - 13.32\left(\frac{a}{W}\right)^2 + 14.72\left(\frac{a}{W}\right)^3 - 5.60\left(\frac{a}{W}\right)^4\right]. \tag{19b}$$

In Eqs. (18) and (19), W and B are the sample width and thickness, respectively, S is the span. P_Q is the critical load. In general, there are three types of load–displacement curves with the critical load P_Q defined for each type curve, as displayed in Fig. 19(b). In Type I, the load–displacement curve is smooth and deviates slightly from linearity before reaching the maximum load (P_{max}). The nonlinearity is caused by the plasticity, subcritical crack growth or both. The P_Q is taken as the intersection of the load with the 95% secant line [Fig. 19(b)]. Type II case shows that slight unstable crack growth (i.e., a pop-in) initiates followed by a further increase in the load before catastrophic failure. Here, P_Q takes the load value at the pop-in initiation. Type III shows a material which behaves nearly linear-elastic before the catastrophic failure. In this case, P_Q takes the maximum load P_{max}.

Since the apparent toughness K_c decreases with increasing specimen size until a plateau is reached, there is specimen size requirement of $0.45W < a < 0.55W$ to ensure that the K_{IC} measurement corresponds to the lower bound at the plain strain plateau. In addition, the following requirements must be met so that the conditional toughness is taken as a valid K_{IC} [38]:

$$B, a \geqslant 2.5\left(\frac{K_Q}{\sigma_Y}\right)^2, \tag{20}$$

$$P_{max} \leqslant 1.1 P_Q, \tag{21}$$

where σ_Y is the yield strength of the material. For other specimens, equations for the calculation of K_{IC} can be found in literature [38] and ASTM E399 [42].

Testing procedure and specimen size limit in ASTM E399 ensure that the obtained K_{IC} is close to the point of crack initiation or a 2% crack extension, without measuring the crack initiation point directly. This procedure is effective for Type II or Type III behavior, but is strongly size-dependent in Type I case as the specimen size is increased. In addition, the size requirement in Eq. (20) often makes it difficult to measure K_{IC}, since the testing specimen must be so large that the W should exceed 1 m to accurately estimate the load at the crack initiation. The second requirement is to assure that the nonlinearity observed in the load–displacement, which relates to the crack initiation and not just the growth of the large plastic zone. This often invalidates good experimental results, especially for the specimen with a large plastic zone [38]. An alternative way is to use J-integral to evaluate K near crack initiation (denoted K_{JC}) in an accurate and size insensitive fashion, which permits valid fracture toughness estimation from invalid K_{IC} tests. According to ASTM standard E1820 [41], the conditional strain-energy release rate J_Q is:

$$J_Q = \frac{K^2(1 - \nu^2)}{E} + J_{pl}, \tag{22}$$

$$J_{pl} = \frac{1.9 A_{pl}}{B b_0}, \tag{23}$$

where A_{pl} is the area under maximum force (P_{max}) versus displacement curve, b_0 is the ligament length, and E and ν are the Young's modulus and Poisson's ratio of the material, respectively. Under mode I, the corresponding fracture toughness K_{JIC} is obtained from the linear elastic, K–J equivalence relationship [159]:

$$K_{JIC} = \sqrt{\frac{E \cdot J_{IC}}{1 - \nu^2}}. \quad (24)$$

There is also an extra size requirement for the *J*-integral-based fracture toughness testing in addition to the size requirement in Eqs. (20) and (21):

$$B, b \geqslant \frac{MJ_Q}{\sigma_Y}, \quad (25)$$

where σ_Y is now defined as the mean of the yield and ultimate tensile strengths, and for Prandtl-field geometries, i.e. CT and SENB. M is an empirically determined coefficient in the range of 10–100, depending on whether the fracture occurs in a stable or unstable manner [158].

4.1.2. Fracture toughness values of BMGs

In the early studies, there have been attempts to measure fracture toughness of MGs with non-standard test methods (such as tensile testing of the edged- or center-notched ribbon specimens) [147,160,161]. The advent of BMGs with large specimens enables the true fracture toughness measurements with standard testing methods to become possible. However, only few compositions (mainly concentrated on Zr-based) for which the valid fracture toughness values are reported, as these alloys simultaneously have enough high glass-forming ability and fracture toughness to fulfill the requirements for standard fracture toughness test procedures. For many other BMGs, even they have sufficiently large sample size needed for fracture toughness test, they are not tough enough to survive in the fatigue pre-cracking [22]. In these cases, the toughness of BMGs has been assessed using notched sample without the pre-fatigue procedure. Although the notch toughness K_Q obtained for BMGs cannot be compared with the standard fatigue pre-cracked toughness K_{IC}, K_Q is a convenient parameter for comparison of the resistance to crack propagation among different BMGs if the samples are uniformly tested under the same experimental condition (e.g., the same sample geometry and bluntness of the notch-root radius).

Among all glassy alloy systems, the fracture toughness of Zr-based BMGs is the most extensively studied. Cornner et al. [162] first reported mode I notch toughness K_{IQ} for $Zr_{41.2}Ti_{13.8}Cu_{12.5}Ni_{10}Be_{22.5}$ BMG (Vitreloy 1), which is in the range of 54–59 MPa $m^{1/2}$. Based on the K_Q values, they estimated the size of plastic zone ahead of the notch root, r_p, to be 102 μm, which is equivalent in size to that observed on the fracture surface morphology. Subsequently, Gilbert et al. [23,163] measured the fatigue pre-cracked toughness K_{IC} on CT samples with two different thicknesses (4 mm and 7 mm) for Vitreloy 1. Although all samples are prepared following ASTM E399 standard, significant variability was observed in the K_{IC} values ranging from 30 MPa $m^{1/2}$ (measured in a 4 mm-thick sample) to 68 MPa $m^{1/2}$ (measured in a 7 mm-thick sample). The measured toughness value seems increase with increasing sample thickness. This variability may be likely associated with the residual stresses at the surface of castings, compositional variation (particularly oxygen), crack branching and ligament bridging, and sensitivity to loading rate. In contrast, Lewandowski et al. [164,165] reported a much lower $K_{IC} \sim 18.4 \pm 1.4$ MPa $m^{1/2}$ for the same alloy while using a SENB sample. Currently, it is not clear if these differences are due to the specimen geometry effects, slight compositional and internal-state difference, differences in the fatigue pre-cracking procedures, or a combination of these factors. They also found that the fracture toughness strongly depends on the notch root radius, and the reported toughness values are significantly increased from 18.4 ± 1.4 MPa $m^{1/2}$ for the fatigue pre-cracked specimen to 101–131 MPa $m^{1/2}$ for that containing the notches with radii of 65, 110 and 250 μm, as shown in Fig. 20 [164]. The notch root radius dependence of the fracture toughness is closely related with shear banding and crack branch behavior ahead of the notch root: the fatigue pre-cracked specimens exhibit a very planar crack front, while the notched specimen exhibits extensive shear banding at the notch as well as significant crack bifurcation [164] (see Fig. 20). These micromechanical processes should absorb more plastic energy than the planar fracture mode, contributing to the difference in measurements.

The fracture toughness of Be-free Zr-based BMGs was also measured with the reported K_{IC} generally similar with that of Vitreloy 1. For example, the K_{IC} is reported to be in the range of 28–69 MPa $m^{1/2}$ for $Zr_{52.5}Al_{10}Ti_5Cu_{17.9}Ni_{14.6}$ (Vitreloy 105) BMG [166] with a SENB sample, and was

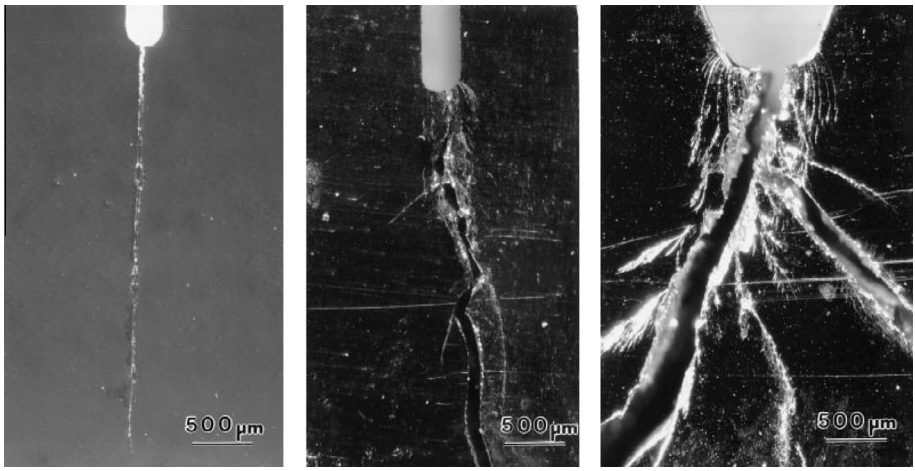

Fig. 20. Typical macroscopic crack path profiles of specimens tested with different notch root radii: (a) fatigued pre-cracked; (b) 65 μm; (c) 250 μm (reproduced from Ref. [164] with permission. ©1998. Elsevier).

estimated according to the length of crack proceeding. Similar values of K_{IC} (35.9–50.3 MPa $m^{1/2}$) are also reported in a $Zr_{55}Al_{10}Ni_5Cu_{30}$ (Z2) BMG [167]. Some studies also reported much higher fracture toughness values in Zr-based BMGs. For example, Kim et al. [168] have claimed to observe the K_{IC} values in excess of 80 MPa $m^{1/2}$ in Ni-free Zr–Be based BMGs. Recently, by a systematic investigation on the chemical effects on the fracture toughness in the quaternary Zr–Ti–Cu–Al systems, He et al. [159,169] developed a $Zr_{61}Ti_2Cu_{25}Al_{12}$ with the K_{IC} (in excess of 100 MPa $m^{1/2}$) among the highest in the reported monolithic BMGs and a significant non-linear elastic fracture behavior in the resistance curve, which are attractive for potential engineering applications. Various factors such as processing conditions of samples, sample geometry and size, minor composition variations as well as testing procedures, all have effects on the measured fracture toughness values. Therefore, it should be prudent to compare these values among different BMG compositions, or to compare with that of commonly used engineering alloys, as have been commonly done in some BMG literatures.

The work above was concentrated on the mode I fracture toughness tests of Zr-based BMGs, there are also a few fracture toughness tests performed under other fracture modes (such as the mode II or the mixed mode) conditions. For instance, Flores et al. [170] measured the mode II fracture toughness on Vitreloy 1 and reported $K_{IIC} \sim 75 \pm 4$ MPa $m^{1/2}$, exceeding the reported mode I fracture toughness (tested for the same BMG material) of 4 times, suggesting that the normal or mean stress plays a significant role in the deformation process at the crack tip. They explained this effect in light of a mean-stress modified free volume model for shear localization in metallic glasses. Varadarajan et al. [171] reported the significant increase both in the notched and fatigue pre-cracked fracture toughness in two Zr-based BMGs (Vitreloy 1 and Vitreloy 106) under mixed mode condition, e.g., the mixed mode I/II test with a mixed mode ratio of 4/6. The notched toughness value of 166.1 MPa $m^{1/2}$ is almost twice that of average results of the notched mode I test (86.0 MPa $m^{1/2}$) for Vitreloy 1. The fatigue pre-cracked mode I tests exhibited much higher fracture toughness values (e.g. 64.0 MPa $m^{1/2}$ with a mixed mode ratio 1/6) than the mode I value (e.g. 37.2 MPa $m^{1/2}$). The increased fracture toughness under mixed-mode conditions is associated with the stress state which could result in different shear banding and crack branching behavior at the crack tip under different loading modes, and mode I is generally considered as the most severe case of loading.

The values of fracture toughness reported in other BMG systems are most in terms of the notch toughness K_Q and in limited compositions. The BMGs based on the noble metals seem to exhibit a much high toughness. For example, the $Pt_{57.5}Cu_{14.7}Ni_{5.3}P_{22.5}$ BMG [172] has a K_Q of 80 MPa $m^{1/2}$ with a large plastic zone about 1.4 mm, which is nearly an order of magnitude larger than that of Vitreloy 1. Demetriou et al. [122] even reported a K_Q as high as 200 MPa $m^{1/2}$ (in term of the J-integral,

$J_C \sim 460$ kJ m^{-2}) in a $Pd_{79}Ag_{3.5}P_6Si_{9.5}Ge_2$ BMG, which is comparable to the toughest engineering metals known (for example, low-carbon steels). However, the critical casting thickness of the alloy is below the width required for direct J-integral measurement. They used a crack tip opening displacement (CTOD) approach for evaluating the toughness, which requires the non-linear elastic fracture mechanics to characterize contribution from plasticity, and the resistance curve analysis to characterize the toughness associated with the crack growth. In contrast, Mg-based and Rare-earth-based BMGs [103,133,173] have the toughness as low as that of traditional brittle materials, for example, the $Mg_{65}Cu_{25}Gd_{10}$ and $Dy_{40}Y_{16}Al_{24}Co_{20}$ BMGs have the K_Q of 1–2 MPa m$^{1/2}$, which is almost close to the ideally brittle glasses [133]. The fracture toughness of Cu-based and Ti-based BMGs have also been studied only in few compositions with good GFA. The reported notched toughness values are generally in the same order of magnitude with that of Zr-based BMGs. For example, the notch toughness in Cu-based BMGs is in the range of 31–65 MPa m$^{1/2}$ [174]. Gu et al. [175] reported the toughness in excess of 100 MPa m$^{1/2}$ in a $Ti_{40}Ni_{25}Cu_{12}Ni_3Be_{20}$ BMG both for the fatigue pre-cracked and notched sample. The fatigue pre-cracked toughness (110 MPa m$^{1/2}$) seems to be slightly higher than the notch toughness (e.g. 102 MPa m$^{1/2}$) for this alloy. It should be noted that these toughness values are not obtained in pure plane strain state but in a mixed plane stress/strain state.

Table 2 compiles the experimental values of K_{IC} and K_Q for various BMGs from literatures. The values of yield strength and plastic zone size r_p ahead of the notch root available for various BMGs are also listed. It is noted that all the data were measured at room temperature. The fracture toughness of BMGs varies in a much larger range than any other kinds of materials. The values of the toughness almost covers the range from the most brittle to the toughest material. This remarkable and diverse property makes BMGs the model system to investigate fundamental issues in fracture mechanics. Although these toughness values (including the K_{IC} and K_Q) are measured under various conditions, a general correlation between the toughness and the size of plastic zone r_p [38,176] from the available data in the table can be found in the form:

$$r_p = \frac{K_C}{\pi\sigma_y^2}, \tag{26}$$

where K_C could be the K_{IC} or K_Q. We note that the plastic zone ahead of the crack tip in BMG are different from that of crystalline alloys, as the zone is formed by multiple shear bands and thus inhomogeneous in the plastic deformation in nature. The correlation indicates that the plastic energy

Table 2
The fracture toughness values (K_{IC}, K_Q), the yielding strength and the size of plastic zone at the crack tip for various BMG compositions and other materials (oxide glasses, engineering crystalline alloys) collected from literatures.

BMGs	K_{IC} (MPa m$^{1/2}$)	K_Q (MPa m$^{1/2}$)	σ_y (MPa)	r_p (mm)	Refs.
Vitreloy 1	–	55–59	1.9	0.102	[162]
	30–68	–	–	–	[23]
	18.4	101–131	–	–	[164]
Vitreloy 105	28–69	–	1.65	0.15	[166]
$Zr_{55}Al_{10}Ni_5Cu_{30}$	35.9–50.3	39.1–48.1	1.7	–	[167]
$Zr_{33.5}Ti_{24}Cu_{15}Be_{27.5}$	69.2–96.8	–	1.75	–	[168]
$Zr_{44}Ti_{11}Cu_{20}Be_{25}$	83.9–85.5	–	1.8	–	[168]
$Zr_{44}Ti_{11}Cu_{9.3}Ni_{10.2}Be_{25}Fe_{0.5}$	21.7–27.5	–	1.86	–	[168]
$Zr_{61}Ti_2Cu_{25}Al_{12}$	112	–	1.6	1.7	[159,169]
$Zr_{56}Co_{28}Al_{16}$	–	77	–	–	[159]
$Zr_{60}Cu_{28}Al_{12}$	–	93	–	–	[159]
$Pt_{57.5}Cu_{14.7}Ni_{5.3}P_{22.5}$	–	80	1.4	1.4	[172]
$Pd_{79}Ag_{3.5}P_6Si_{9.5}Ge_2$	–	200	1.49	6	[122]
$Cu_{49}Hf_{42}Al_9$	–	65 ± 10	2.33	–	[174]
$Ti_{40}Zr_{25}Cu_{12}Ni_3Be_{20}$	110	102	1.65	–	[175]
$Dy_{40}Y_{16}Al_{24}Co_{20}$	–	1.26	–	–	[268]
$La_{55}Al_{25}Ni_5Cu_{10}Co_5$	–	5	0.7	10^{-3}	[173]
$Mg_{65}Cu_{25}Tb_{10}$	–	2	0.66	10^{-4}	[173]
$Fe_{46}Ni_{32}V_2Si_{14}B_6$	–	4	3.8	2×10^{-5}	[173]

dissipation during the shear banding process plays a critical role in blunting the crack tip and shielding the crack propagation. For BMGs of the same alloy system with similar yield strengths, the fracture toughness or energy is mainly determined by the material ability of shear-band extension and multiplication which is manifested as plastic zone size in front of crack tip [139].

The size of plastic zone is a useful guide for judging the plasticity of a BMG sample upon its thickness. If r_p at the tip of the crack is much smaller than the sample size, the fast fracture occurs. If r_p is greater than the sample size, the brittle fracture is not expected. Fig. 21 shows the Ashby's plot of the fracture toughness versus the elastic limit (or yield strength) for BMGs and various engineering materials including metals and alloys, ceramics, polymers and oxide glasses [176]. The diagonal contours show the r_p which can be estimated from Eq. (26). Although the fracture toughness of BMGs is comparable to that of some engineering alloys (e.g. steels, Mg alloys), their r_p is about one order of magnitude smaller, which is attributed to the high strength of BMGs. The small r_p also contributes to the macroscopically brittle behavior of BMGs besides the inhomogeneous flow or shear banding process, despite their high fracture toughness. In terms of the r_p, a brittle BMG (e.g. $Fe_{40}Ni_{40}P_{14}B_6$ with the $K_C \sim 10$ MPa $m^{1/2}$ [103]) is even worse than conventional silicate glasses.

4.1.3. Effects of sample geometry, size, and testing conditions on fracture toughness measurement

In general, fracture toughness is an intrinsic materials parameter, which should not be significantly influenced by sample geometry and testing parameters if the standard procedures (ASTM E399 and E1820) described above are strictly observed. However, the size criteria in these standards are developed based on the common behaviors of polycrystalline alloys such as steels, aluminum and titanium alloys [41,158]. In contrast, BMGs display completely different deformation behaviors from that of crystalline alloys. The ductility or toughness of BMGs is positively correlated with the number of shear bands formed during the deformation. The thick plates of BMGs fail catastrophically in bending without significant plastic deformation, while when the thickness t is below the size of plastic zone r_p, the BMGs could be bent in a ductile manner with increased shear band number and increased ductility prior to fracture with decreasing plate thickness [120]. This thickness-dependent bending ductility makes BMGs quite distinct from crystalline alloys. However, the developed minimum

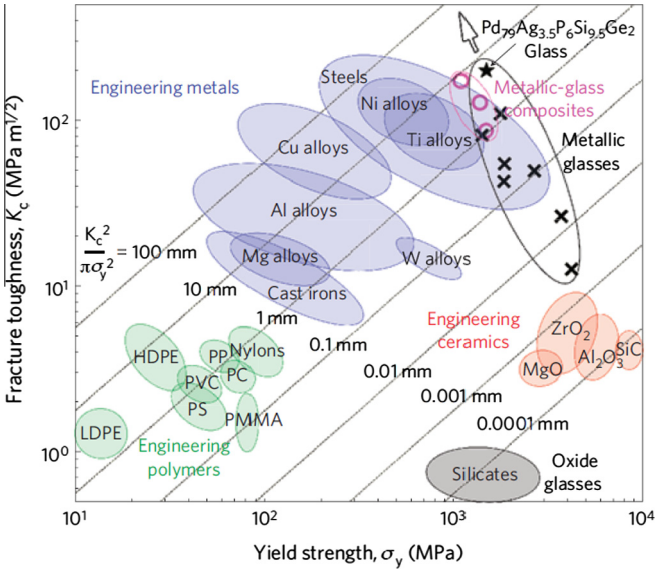

Fig. 21. The Ashby map for the fracture toughness and elastic limit for metals and alloys, glasses, ceramics, polymers and metallic glasses. The contours show the plastic zone size d in mm (reproduced from Refs. [122,176] with permission. ©2006. Elsevier).

size-requirements in ASTM E399 and E1820 are based on the common behavior of crystalline alloys, and do not distinguish between BMGs samples that are above or below the critical bending thickness. Another major difference between BMGs and crystalline alloys is that BMGs shows typical strain softening behavior, in contrast to the work hardening of crystalline alloys. The strain softening is the main attribute of the shear localization of BMGs under various deformation modes (compression, tension and bending) [8]. Yet, the calculation of some fracture toughness parameters (such as the *J*-calculation in E1820) often assumes a strain hardening law of the materials. Considering these differences, it is suspected that whether the ASTM standard procedures can be directly applied to determine the fracture toughness of BMGs without conservation.

Table 3
Summary of sample dimensions and pre-cracking condition as well as fracture toughness results, failure type and required sample thickness, B_{crit}, and ligament size, b_{crit}, for plane strain and small-scale yield conditions [158].

B (mm)	W (mm)	a/W	b (mm)	K_{IC}, K_{JIC}, K_Q (MPa m$^{1/2}$)	B_{crit}, b_{crit} (mm)	Failure type (ASTM, E399)	Pre-cracking
CT, K_{IC}							
1.99	21.45	0.50	10.8	18.7	0.3	III	Tension
2.03	21.42	0.50	10.77	28	0.68	III	Tension
2.26	19.85	0.50	9.95	28.8	0.72	III	Tension
2.34	19.83	0.50	9.91	25.7	0.57	III	Tension
Mean: 25.3 MPa m$^{1/2}$, standard deviation: 4.6 MPa m$^{1/2}$							
SENB, K_{IC}							
2.01	4.23	0.55	1.91	36.5	1.15	III	Tension
2.05	4.15	0.49	2.1	26.2	0.59	III	Tension
2.3	3.94	0.54	1.8	35.3	1.08	III	Tension
2.34	4.08	0.47	2.18	44.9	1.74	III	Tension
Mean: 35.7 MPa m$^{1/2}$, standard deviation: 7.7 MPa m$^{1/2}$							
SENB, K_{JIC}							
2.04	4	0.58[a]	1.66	31.1[c]	0.84	III	Tension
2.33	3.95	0.45	2.18	46.5	1.87	III	Tension
1.28	2.34	0.56[a]	1.03	35.2	1.07	III	Tension
2	2.07	0.45	1.14	43	1.6	III	Tension
Mean: 39 MPa m$^{1/2}$, standard deviation: 7.0 MPa m$^{1/2}$							
SENB, K_Q, sub-sized							
1.99	4.22	0.51	2.07	63.5	3.49	III	Tension
2.2	4.1	0.48	2.12	66.4	3.81	III	Tension
1.33	2.25	0.63[a]	0.84	39.9	1.38	III	Tension
1.1	2.13	0.7[a]	0.65	66.6	3.84	III	Tension
1.92	1.93	0.44[b]	1.08	45.5	1.79	I	Tension
1.87	4.03	0.52	1.93	72.6	4.56	I	Tension
2.04	2.03	0.58[a]	0.86	37.2	1.2	I	Tension
2.23	2.03	0.54	0.94	33.9	0.99	I	Tension
2.07	3.97	0.48	2.06	81.6	5.76	I	Tension
1.93	2.06	0.39[b]	1.26	66.6	3.84	I	Compression
2.02	2.14	0.37[b]	1.35	66.3	3.8	I	Compression
Mean: 58.2 MPa m$^{1/2}$, standard deviation: 16.1 MPa m$^{1/2}$							
SENB, K_Q, notched only							
2.16	4.61	0.45	2.54	91.6	7.26	III	–
2.15	4.08	0.45	2.23	95.9	7.96	III	–
2.72	4.14	0.49	2.09	94.1	7.66	III	–
Mean: 93.9 MPa m$^{1/2}$, standard deviation: 2.2 MPa m$^{1/2}$							

[a] Sample with $a/W \approx 0.55$–0.7.
[b] Sample with $a/W < 0.45$.
[c] Not a valid K_{IC} value due to $a/W > 0.55$.

Recent dedicated work of Gludovatz et al. [158] systematically studied the effect of sample geometry and size on the measurement of fracture toughness of BMGs. With a typical $Zr_{52.5}Cu_{17.9}Ni_{14.6}Al_{10}Ti_5$ (Vitreloy 105), they measured the K_{IC} values according to ASTM E399 and J_{IC} values according to ASTM E1820 using CT and SENB specimens with different sizes. We reproduced their results in Table 3, which shows the K_{IC}, K_{JIC} and K_Q data for all valid and invalid tests. The K_{JIC} values are obtained from J_{IC} toughness values using the standard model I, linear-elastic, and K–J equivalence relationship (Eq. (24)). As can be seen, the mean valid K_{IC} value of the BMG is 25.3 MPa $m^{1/2}$ using four CT specimens of which the crack length, a, the ligament size, b, and the sample thickness, B, are well above the minimum size requirement of Eq. (20). In contrast, the valid fracture toughness tests from four SENB specimens with exactly the same samples as that of CT yields a K_{IC} = 35.7 MPa $m^{1/2}$, which is 41% increase compared to the CT sample results. Other four SENB samples are smaller than that required by ASTM E399 for K_{IC} testing and are allowed by the J-integral-based standard E1820. Such tests give significantly higher toughness values K_{IJC} = 39 MPa $m^{1/2}$, which is 51% larger than the valid K_{IC} values measured with CT samples. This clearly indicates that the sample geometry has a significant influence on the measured fracture toughness values, even if the sample meets the size requirement according to ASTM standards. In addition, the measured conditional K_Q toughness values with SENB samples smaller than that required by ASTM standard E399 for valid tests have a mean value of ~58.2 MPa $m^{1/2}$ with a standard derivation of 16.1 MPa $m^{1/2}$, which are much larger than the valid K_{IC} and K_{JIC} values. The samples failed with significant plastic deformation and multiple shear bands ahead of the pre-crack tip, similar with the behavior observed in the bending of thin plates. The largest value of K_Q almost approaches those of SENB samples tested only with notches as listed in Table 3 [158].

From Table 3 and Fig. 22, one can see that the K_Q values increase with progressively decreasing uncracked ligament width, b, in contrast to the behavior of crystalline metals. The K_Q values of aluminum, titanium and steel samples with different sizes remain constant until the sample ligament size reaches the lower bound, and then K_Q starts to decrease [177]. This is attributed to the effect of applying linear-elastic fracture analyses to undersized samples where small-scale yielding is not achieved. However, if one calculates the fracture toughness in terms of the J-integral by taking into account the full elastic–plastic response of an individual sample, indistinguishable results for K_{IC} and K_{JIC} will be obtained, indicating that there is no sample-size effect. The increased K_Q values with decreasing ligament size of BMGs, unlike crystalline alloys, implies that the J-integral approach may be unable to guarantee reproducible size-independent toughness values in small-sized BMG samples. On the other hand, the K_Q values vary widely for the same-sized samples [see Fig. 22(a)], and show extensive ductility that cannot produce valid fracture toughness result using ASTM standard. This

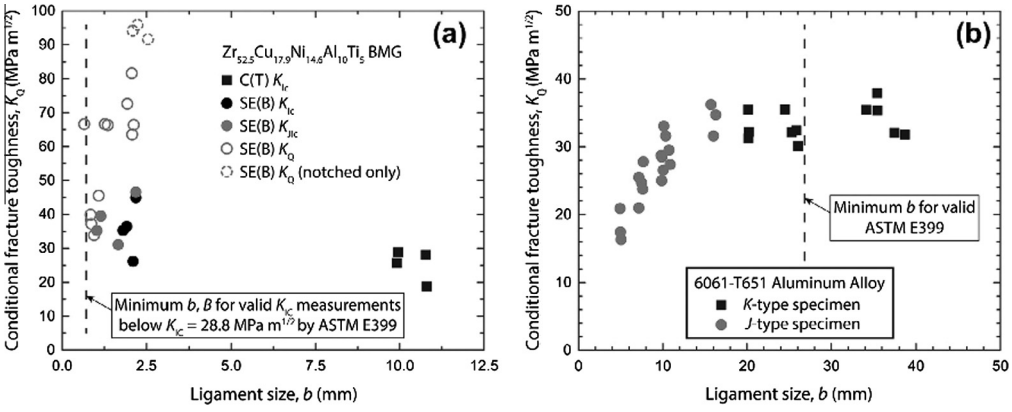

Fig. 22. Conditional fracture toughness, K_Q, data for (a) $Zr_{52.5}Cu_{17.9}Ni_{14.6}Al_{10}Ti_5$ BMG and (b) 6061-T651 (polycrystalline) aluminum alloy as a function of the uncracked ligament width. The polycrystalline 6061-T651 aluminum alloy data were taken from Ref. [177] (reproduced from Ref. [158] with permission. ©2014. Elsevier).

indicates that the lower sample size limits of ASTM E399 appear to be near a point of transition where the BMG achieves gross plasticity and high ductility. Therefore, a portion of samples lies on each side of the transition point, where extensive crack blunting occurs for some sample but not for others. It is suggested that the ASTM E399 sample size requirements should be cautiously accepted for providing size-independent K_{IC} results. The sample with smaller size could present a wider scatter in K_Q values and possibly somewhat elevated toughness values [158].

In summary, the sample geometry and size have more significant effect on the fracture toughness measurement of BMG compared to that of crystalline alloys. Such behavior is likely related to the size-dependent bending ductility and strain softening found for BMGs. The variability of the fracture toughness values for the same BMG composition, even accords with the ASTM standards, can be partially attributed to the sample geometry and size, in addition to the processing conditions and thermal history (to be discussed in Section 4.3). Toughness values measured using sample smaller than that required by ASTM E399 should be considered as size dependent, even for J_{IC} measurements. So, to compare the fracture toughness values of new BMG compositions with other compositions, one should use the exactly same sample geometry and testing configurations to obtain fair comparison.

The testing configurations such as loading rate and testing modes (displacement- or load-controlled) and testing temperature also affect the measured fracture toughness [8,22]. For example, Henann et al. [178] investigated the effects of changes of these factors on the fracture toughness of Vitreloy 1. The test was conducted at displacement rates ranging from 0.01 to 10 mm/min, and loading rate ranging from 31.5 to 5700 lb/min and test temperatures from 298 to 693 K. Significant changes of the fracture toughness are observed by varying these parameters. A fracture mechanism map with the normalized toughness (versus the toughness at room temperature) is plotted against the normalized testing temperature (versus the glass transition temperature T_g), as shown in Fig. 23.

4.2. Crack initiation and growth during toughness tests

Crack initiation and growth process during the toughness test is crucial for understanding the physical origin of fracture toughness. For BMGs, cracks preferentially initiate from shear bands in the plastic zone ahead of the notch root due to the shear softening, and then propagate or branch along these bands. Microscopically, this often involves cavitation process in shear bands associated with the

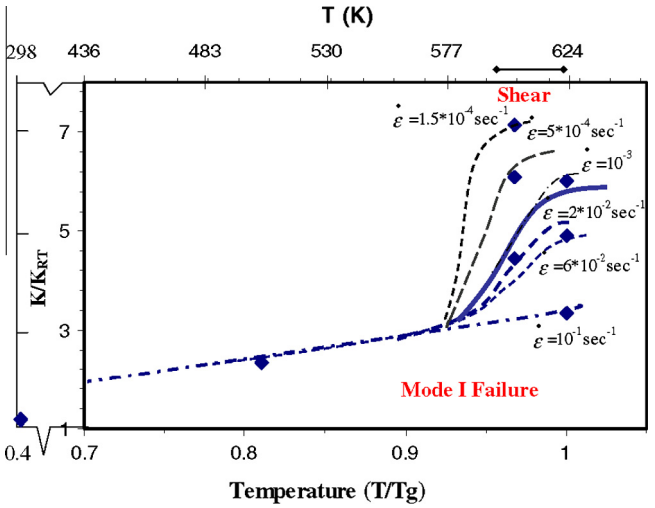

Fig. 23. The fracture mechanism map for the Vitreloy 1 tested at different temperatures and strain rates. Individual data points shown along with transition from higher toughness (shear fracture) to lower toughness mode I fracture. Solid line delineates approximate position of transition (reproduced from Ref. [296] with permission. ©2008. Springer).

significant softening caused by the shear dilation (free volume increase) or temperature rise in metallic glasses [179]. However, the detailed atomic process is still poorly understood due to the experimental difficulties in characterizing the highly localized shear banding both spatially and temporally. Generally, the shear band extension direction closely connects with the stress field ahead of the notch root and can be analyzed with slip line theory by assuming metallic glass as non-hardening materials under plastic strain and plastic conditions [180]. According to the McClintock's analysis [181], in pure tension, the slip lines form at the angle of 45° with the loading axis, while in bending, a complex arc results in the fan shaped Prandtl slip line fields, which agrees well with the observed shape of plastic zone formed by shear bands in experiments [180] (see SEM micrographs in the crack tip in Fig. 24). However, in this case, as the slip lines bend back to the crack plane, they tend to force the crack to remain stable in the plane if a crack forms along the shear band. Thus, the crack branching is not expected for the CT or SENB geometries. Flores et al. [180] used the single-edge notched tension (SENT) sample to *in-situ* examine the crack growth behavior with a CCD camera, and analyzed the results with the slip line theoretical solutions. The *in-situ* images for crack branching are shown in Fig. 24. The branches initially make an angle of up to 80° with the main crack plane. When the branches grow away from the main crack, they become parallel and are evenly distributed, which agrees with the prediction from the slip line theory. Instead continuously growing with increasing load, the branches sporadically jump forward, although on average the branches remain equal in length from the main crack tip until the final stages of the experiment. The extensive blunting of the main crack tip, gives rise to the extraordinarily high stress intensity factor ($\sim$134 MPa $m^{1/2}$), which is most likely compromised by the blunted tip. The branched zone is approximately 370 μm wide prior to failure, which is significantly smaller than the estimates of the plastic zone size with Eq. (26) from homogeneous plastic deformation. Although the onset of branching is not directly captured in their experiments, the analysis of the stress intensity of the branched crack tips in the damage zone reveals lower value ($\sim$15 MPa $m^{1/2}$), which is consistent with other studies and estimates based on Argon's variant of Taylor's fluid meniscus instability [28].

For some BMGs with high fracture toughness values [122,159,169], a significant non-linear elastic fracture behavior can be observed, and this is often manifested as a stable crack growth behavior in the crack-resistance curve (*R*-curve). A typical *R*-curve in the form of fracture toughness K_J (converted from *J*-integral) plotted against the crack extension length Δa for tough $Pd_{79}Ag_{3.5}P_6Si_{9.5}Ge_2$ BMG [122] is shown in Fig. 25(a). Demetriou et al. [122] investigated the crack growth behavior in the BMG with the highest toughness K_J almost approaching 200 MPa $m^{1/2}$ by carrying out fracture toughness tests *in situ* in SEM. Their observations indicate that the evolution of the damage ahead of the crack tip for this alloy can be described in term of a three-step process: shear bands firstly form along fan-shaped (Prandtl field) slip lines that bend back to the crack plane, and large shear offsets occur along the evolved slip planes [Fig. 25(c)] similar with that observed by Flores et al. [144]. When a critical sliding strain is reached with the increasing load, an extended shear band opens at the notch tip

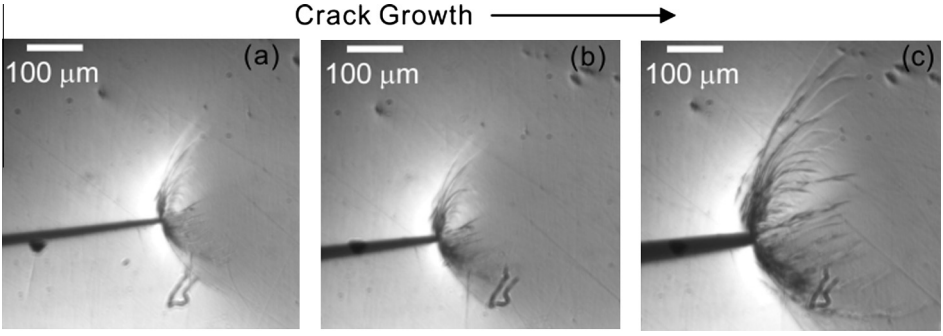

Fig. 24. In-situ image of crack branching for a SEN(T) Vitreloy 1 specimen from Flores's experiments at a displacement rate 0.5 μm/s. The stress intensities at the main crack tip are (a) 58 MPa $\sqrt{m}$, (b) 81 MPa $\sqrt{m}$ and (c) 116 MPa $\sqrt{m}$ (reproduced from [180] with permission. ©1999. Elsevier).

and evolves as a crack [see Fig. 25(d)]. Meanwhile, extensive shear banding is observed to persist ahead of the evolved crack tip to promote significant crack-tip blunting. Finally, stable crack extension is attained until the final fracture due to the slip bands bend back to the crack plane. Although the mechanism controlling the development of plastic zone for this glass is not fundamentally different from other BMGs, the extent of shear sliding and observed shear offsets are unprecedented (as large as 50 μm) for this Pd-based BMG.

He et al. [169] also obtained similar *R*-curve in fatigue pre-cracked $Zr_{61.6}Ti_{4.4}Cu_{24}Al_{10}$ BMG which has a toughness as high as that of Pd-based BMG. From the laser-stereomicroscope micrograph of the fracture surface for the BMG, they found three distinct regions (regions I–III) along the direction of crack extension, as shown in Fig. 26. Region I is the fatigue pre-cracked region contains the typical fatigue striation; Region II exhibits a laminar feature with a larger interspacing, and region III is the re-fatigue region where rougher surface with finer striation than region I can be found. A further examination on the surface profile indicates that region II is caused by the shear band shear-off rather than real crack propagation. The bending regime in the nominal *R*-curve arises from the shear-off in shear bands (corresponds to region II) ahead of the crack tip, instead of the usually assumed physical crack extension. To illustrate the high fracture toughness observed for this alloy, they also analyzed the crack deflection and the consequent change of local load condition at the crack tip [135]. The maximum shear stress can be applied to determine the shear band formation and thus the plastic zone

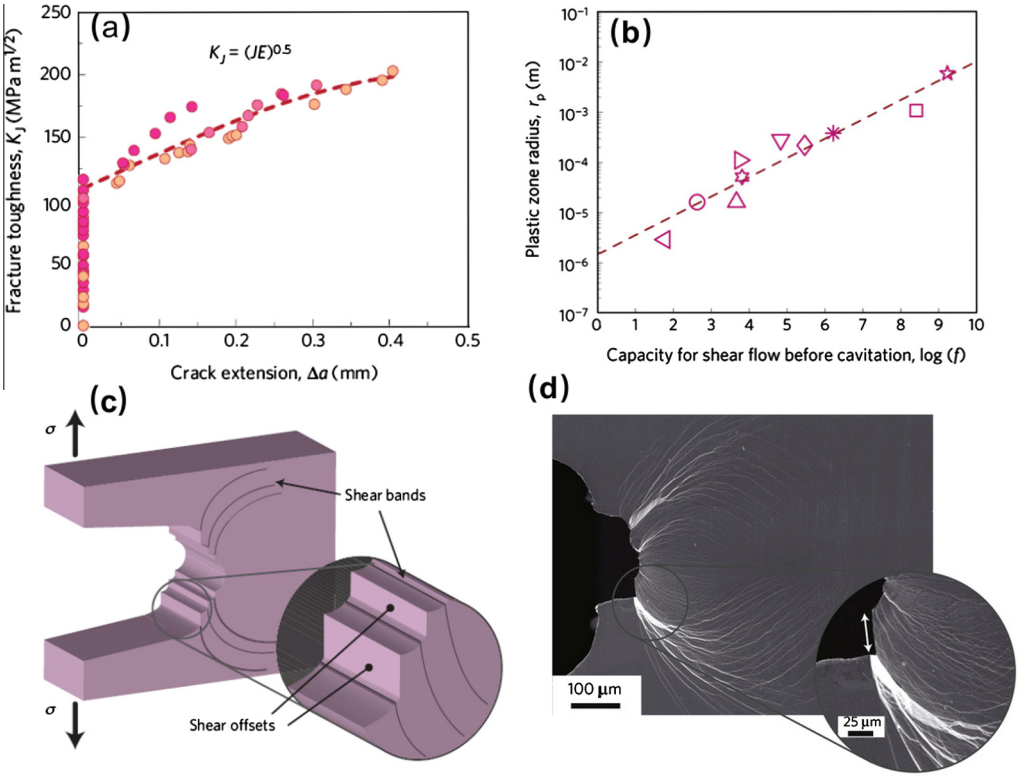

Fig. 25. (a) A typical the crack resistance-curve (*R*-curve) for $Pd_{79}Ag_{3.5}P_6Si_{9.5}Ge_2$ BMG. (b) Logarithm of the plastic-zone radius, plotted against the estimated capacity for shear flow before cavitation for different BMGs. (c) Schematic diagram illustrating the process of the crack blunting through shear sliding under open stress. (d) SEM micrograph of a deformed notch in a glassy $Pd_{79}Ag_{3.5}P_6Si_{9.5}Ge_2$ specimen showing extensive plastic shielding of an initially sharp crack. Inset: Magnified view revealing a 50 μm shear offset (arrow) developed during plastic sliding (reproduced from Ref. [122] with permission. ©2011. Nature Publishing Group).

contour. Under purely mode I testing and the plane stress condition, it is easily shown that $T = \frac{K_I}{\sqrt{2\pi r}} \cos\frac{\theta}{2} \sin\frac{\theta}{2}$, where r and θ are the distance and angle from the crack tip, respectively, and T will reach the maximum at $\theta = 90^\circ$. During the testing, the crack deflects and cause the change of the stress state and loading mode at the crack tip. The change is from pure mode I to a mixed one, involving both mode II and mode I. Based on the solution of fracture mechanics, the reduction in driving force at the crack tip can be calculated as [169]:

$$k_I = a_{11}K_I + a_{12}K_{II}, \tag{27a}$$

$$k_{II} = a_{21}K_I + a_{22}K_{II}, \tag{27b}$$

where k_I and k_{II} are the local stress intensity factors at the crack tip, K_I and K_{II} are the global stress intensity factors and a_{ij} are the coefficients related to the crack deflection. The load mixture can be described by parameter, $M = (2/\pi)\tan^{-1}(k_I/k_{II})$. For purely mode I loading, $M = 1$; for pure mode II

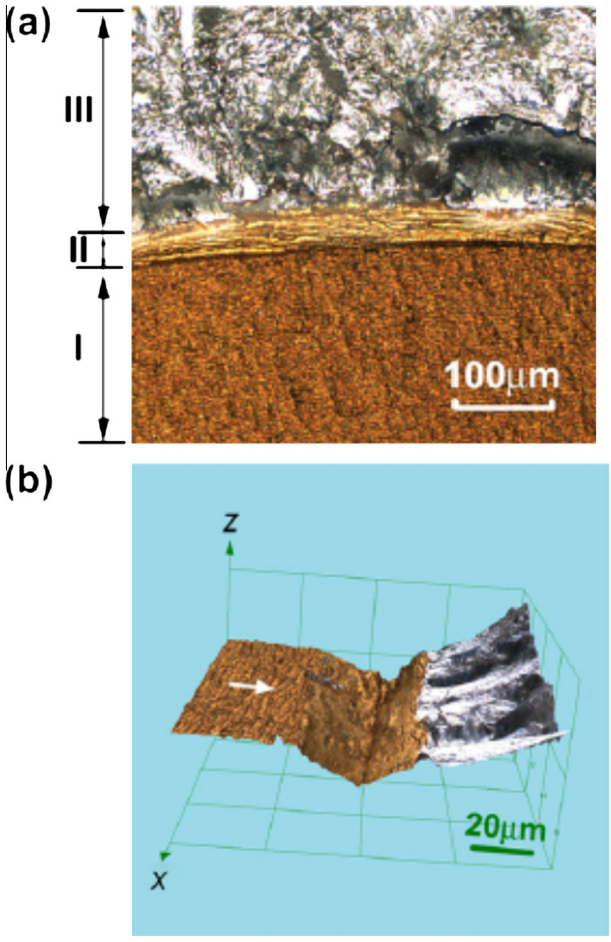

Fig. 26. (a) Laser optical micrographs of fracture surface for $Zr_{61.6}Ti_{4.4}Cu_{24}Al_{10}$ BMG specimen subjected to heat-tinting and re-fatiguing (a) three distinct regions along the crack propagation direction from bottom to top. (b) 3-D image of a half specimen, showing shear offsets ahead of fatigue pre-crack, deviating from crack propagation direction from left to right (indicated by the white arrow) (reproduced from Ref. [169] with permission. ©2012. Elsevier).

loading, $M = 0$, and for mixed mode loading, $0 < M < 1$. Under the mixed mode I and II loading, T at the crack tip can be written as:

$$T = \frac{K_I}{\sqrt{2\pi r}} R(\theta), \tag{28}$$

where $R(\theta)$ is the angular function related to the ratio, $\xi = K_{II}/K_I$. If the shear band is assumed to form when the shear stress reaches a critical value T_c, the contour of plastic zone is given by

$$r_c = \frac{K_I^2 R(\theta)}{2\pi T_c}. \tag{29}$$

The calculation results [169] (see Fig. 27) show that pure mode I loading may have turned into mix mode (I/II) loading due to the appearance of shear-off zone and the meandering crack paths. As shown in Fig. 27(c), even though the far-field or global loading is mode I, the real local loading at the crack tip has evolved into a different loading condition, far from matching the olive-like shape. In contrast, the calculated contour under mix-loading condition [see Fig. 27(d)] is in good agreement with that of the fan-shape plastic zone induced by the multiple shear bands. The high propensity for the crack reflection and spontaneous change in loading mode (more pronounced than that of other BMGs) is also proposed as a major reason for the high fracture toughness of this BMG, as crack propagation becomes much more difficult in mix-loading condition [170,171].

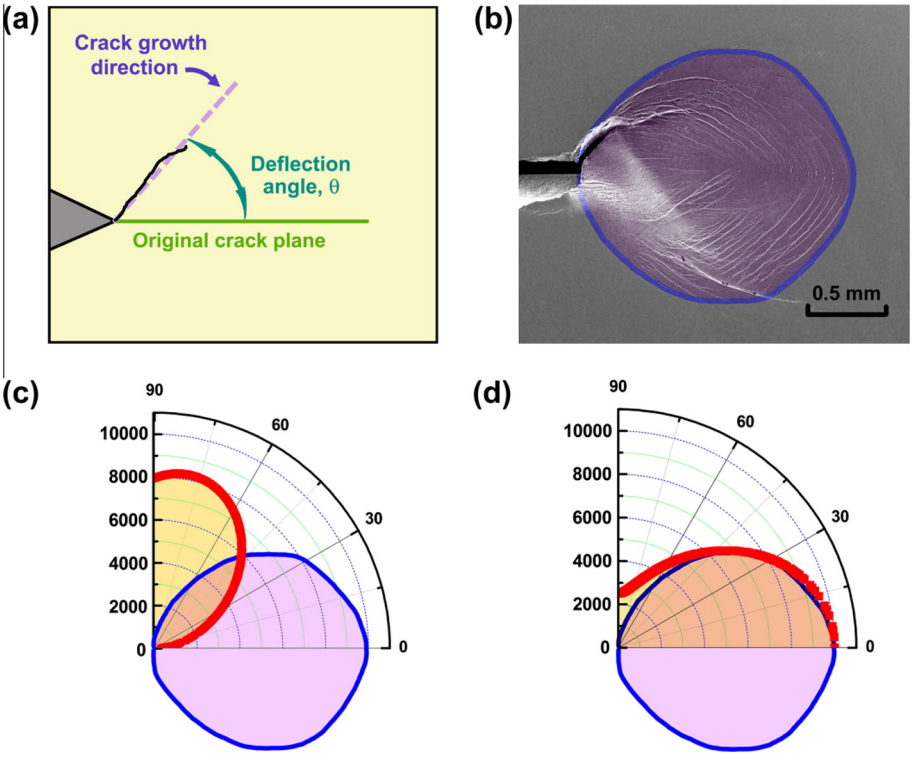

Fig. 27. (a) Schematic diagram of shear-induced crack deflection with respect to the original plane of the crack. (b) SEM image showing the olive/fan-shaped plastic zone at the crack tip in ZT1 BMG. The (blue) boundary of this (light-purple) zone is evidently very different from the (red) contour for the maximum shear stress calculated in (c) under predominantly mode I loading, but closely matches that calculated in (d) under a highly mode II loading condition (reproduced from Ref. [169] with permission. ©2012. Elsevier).

4.3. Factors affecting fracture toughness

There is significant variability in the measured values of fracture toughness even for BMGs with the same nominal composition. It is important to identify the factors (intrinsic or extrinsic) that influence the toughness, which could act as a useful guideline for the material selection and design in BMGs. The correlation between the measured values of fracture toughness and plastic zone size ahead of the notch root indicates that the toughness is closely related with the material ability for the plastic deformation (shear banding) and the crack branching in the notch area. Both effects could effectively lower the stress concentration factor in the crack tip and absorb the released elastic energy during fracture. In this aspect, the fracture toughness depends not only on the intrinsic amorphous structure and composition, but also on other factors such as the internal state (free volume content, structure inhomogeneity, impurities, etc.) caused by the preparing conditions of alloys, as these factors could greatly affect the shear band behavior in the crack tip. The experimental factors such as sample geometries, loading rate, mode of testing (displacement- or load-controlled) also influence the shear banding and crack branching. Various factors that influence the fracture toughness of BMGs are discussed in details as below.

4.3.1. Composition and structure

The fracture toughness of BMGs varies significantly with the composition, especially when alloys of different systems are compared. For example, the K_C varies at least two orders of magnitude from brittle Dy-, Mg-based BMGs [25,173] to the tough Pd or Pt-based BMGs [122,172]. The fracture energy G_C [$G_C = K_C^2/E$, for the plane stress, and $G_C = K_C^2/E(1-\nu)$, for the plane strain] variation range is even broader and reaches four orders of magnitude [91,103]. This large variability is attributed to the intrinsic atomic structure and bonding nature in different BMGs. BMGs have short-range order (SRO) or medium-range order (MRO)] atomic structure [16,182,183], and the atomic clusters of SRO can be viewed as the building blocks of amorphous structure of BMGs. Many types of building blocks in the amorphous structure of different BMGs have been found from experimental structural characterization (e.g. X-ray diffraction or neutron scattering) [184–186] and molecular simulations [16,182]. For example, icosahedra cluster, which has a high packing efficient or density comparable with face centered cubic (fcc) or hexagonal close-packed (hcp) structure but is not accepted in crystalline symmetry, usually prevails in some BMGs [182,187], while the main local SRO unit is the tri-capped trigonal prism for some Fe-based or Ni-based metallic glasses [16,188] (e.g. nine Ni atoms in the shell with six for the trigonal prism and three for the caps and one P atoms in the center for the Ni–P metallic glass [189]). Both the atomic configuration of SRO units and the MRO (SRO units connect and form MRO) have a significant influence on the macroscopic properties of BMGs [182]. The chemical short range order also has an effect, especially when some non-metallic elements are added into alloys [16]. A clear correlation between the atomic-level structure and macroscopic properties including the fracture toughness in BMGs is still ambiguous, and researchers [18,103] have to turned into seeking the correlation between the toughness and some parameters that indirectly reflect the structure of BMGs (such as elastic constants [18]), which will be discussed in Section 4.4.

4.3.2. Preparation conditions of BMG

Preparation conditions of BMGs are the major factors for the variation in the reported fracture toughness values for BMGs with the nominally same composition [22]. The origin is that the measured properties of BMGs are highly sensitive to the internal structural states (such as free volume content and distribution, dynamic and static heterogeneities) which are induced from different preparing conditions [91,190]. These factors include cooling rate during the cast, residual stress, slight composition variation and impurities such as oxides and minor carbon and silicon [22].

BMG in the non-equilibrium state contains the excess volume (or free volume) compared to the corresponding equilibrium crystalline state [45,191]. The amount of quenched free volume in the glass depends on the quenching rate. The cooling rate can be changed by casting the sample into different sizes during the processing of BMGs as illustrated by Gu et al. [192] in a Ti–Zr–Cu–Ni–Be BMG. The changes in cooling rates results in large variation of fracture energy, ranging from 148.9 to

0.2 kJ m^{-2}. The sample with a higher cooling rate has a less density or more free volume contents, and thus a higher toughness. Similar effects of the cooling rate are also recently reported in a $Cu_{49}Hf_{42}Al_9$ BMG [193]. By increasing the cooling rate during the casting of the metallic glass liquids with a mixed argon and helium atmosphere, the notched toughness of the resultant BMG can be tripled relative to that obtained at slower cooling rate. The elevated toughness is accompanied with a ten-fold increase in the size of the plastic zone at the crack tip, as well as the reduced shear modulus and microhardness of the BMG. All of these can be attributed to the lowered density and increased frozen-in excess volume in the BMG with a higher cooling rate. Tan et al. [190] reported a similar correlation between the toughness and the average free volume content in a Zr–Co–Al BMG. A large stable plasticity found in the sample cast with the higher cooling rate, and corresponds to the internal state with more average free volume as revealed by lower density, high enthalpy change and higher Poisson's ratio. These factors facilitate the plastic flow and multiple shear bands formation when stress is applied.

The high quenching rate could also induce large thermal ingredients, especially when the large-section sample is processed. The ingredients, together with the large changes in the viscosity over a narrow temperature change near the glass transition, result in "thermal tempering stress" [194]. As shown by Aydiner et al. [195], the compressive residual stress at the surface of Vitreloy 1 plate due to thermal tempering reaches several hundreds of MPa, which is balanced by the tension stress in the mid-plane. Such residual stress will imposed on any applied stress, potentially affects the fracture behavior. It is found that the K_{IC} decreases from 51 to 34 MPa $m^{1/2}$ after the removal of residual stress in a $Zr_{44}Ti_{11}Cu_{10}Ni_{10}Be_{25}$ BMG [196]. The processing of large sections of BMGs could also generate slight composition variation at different parts of a casting specimen [22]. Such composition inhomogeneity could lead to different glassy structure or configuration and hence affects the measured toughness values. Kawashima et al. [167] showed that the fracture toughness values of $Zr_{55}Al_{10}Ni_5Cu_{30}$ BMG lie in a wide range from 35.9 to 76.2 MPa $m^{1/2}$, depending not only on the casting lot but also on specimens taken from the same casting. There is a sample orientation dependence of the fracture toughness both for the notched and pre-fatigue samples for this BMG. For most tested specimens, the measured fracture toughness values for the orientation, in which the crack propagates in the melt flow direction, seems to be higher than that for the orientation where the crack propagates across the melt flow direction. The essential cause may be the microstructure inhomogeneity due to the composition variation across the sample during casting.

The oxygen content is another important factor for the preparation of BMGs [162,164]. Generally, oxygen is harmful not only to the glass-forming ability but also to the mechanical properties [13]. The oxygen can be either chemically solved in the BMG alloy or form oxides with an oxidizing element and precipitate as the inclusions, and thus has different effects on the toughness of BMGs. In the first case (more typical in early transition metal/metal glass), the oxygen is presented as one of constituents in the alloy and thus deteriorates the toughness or ductility of BMGs intrinsically. For example, Conner et al. [197] found that $Zr_{57}Nb_5Al_{10}Cu_{15.4}Ni_{12.6}$ alloy with no oxygen demonstrated a significant compressive and bending ductility, while that with higher oxygen content lost virtually all ductility. The ductility degradation can be attributed to the precipitation of the intermetallic compounds due to the solving of oxygen in the amorphous matrix. Similar toughness degradation due to the solving of oxygen in a $Zr_{55}Al_{10}Ni_5Cu_{30}$ BMG was also reported by Keryvin et al. [198] where even very limited amount of oxygen can modify mechanical properties such as elasticity, hardness or compressive failure stresses and dramatically change the toughness. While for the latter case (more typically in metal/metalloid glasses such as Fe-based glasses), oxygen inclusions often form and distribute homogeneously in the metallic glass. As these inclusions tend to catalyze the formation of cracks, the toughness of BMGs can be degraded extrinsically. The detrimental effects of oxide inclusions and porosity on the toughness have been demonstrated in Fe-based BMGs [199]. Madge et al. [200] argued that the apparent brittleness of the Mg- and rare earth-based BMGs can be attributed to oxide particles dispersed in the glassy matrix and, thus is partially extrinsic in nature. The intrinsic toughness of these glasses is higher than previous reports suggested.

4.3.3. Effects of thermal-annealing and structural relaxations

BMG undergoes structural relaxation or aging and relaxes into the more deep local minima in the potential energy landscape when is annealed below T_g [201,202]. The thermal annealing is often used

to reduce the residual stresses in BMG induced in the rapid solidification process and to tune some functional or mechanical properties (such as magnetic properties) [203]. The low-temperature annealing is also found to cause the embrittlement or the largely reduction of toughness in BMGs [196,203]. The severe thermal annealing-induced embrittlement can be attributed to various factors, and is better interpreted from the reduction of the deformation flow units such as free volume after the annealing. At the atomic level, the plastic flow of BMGs is known to occur through the operation of flow units which are easily activated in some local atomic sites with large density of free volume and low flow resistance [46,87,88]. It is expected that large amount of free volume or local density fluctuation in BMGs promote easy operation of the flow units at different sites, leading to profuse shear bands. When these flow processes occurs at the crack-tip region, they can mitigate the stress concentration, and in turn result in high fracture toughness [22]. For example, Murali et al. [203] found a one-to-one correspondence between the enthalpy changes at the glass transition and the impact toughness Γ during the sub-T_g annealing of Vitreloy 1. Severe embrittlement, with the losses of up to 90% in Γ, occurs with annealing. The decreased toughness in the annealed sample is consistent with the reduced shear band activity in the instrumented indentation experiments. Launey et al. [196] reported a similar correlation between the free volume reductions and the fracture toughness degradation in $Zr_{44}Ti_{11}Cu_{10}Ni_{10}Be_{25}$ BMG by similar enthalpy recovery measurements, as shown in Fig. 28.

The continuous heating or holding a BMG at higher temperature could also annihilate the free volume quenched from rapid solidification process, and often leads to an abrupt drop of toughness or ductile-to-brittle transition (DBT) in BMGs. Wu and Spaepen [204] first theoretically rationalize the correlation between DBT and free volume change during the structure relaxation by employing the free volume theory. By a series of theoretical deductions, they showed that the fraction change of free volume can be expressed as a function of the annealing time t_A and annealing temperature T_A:

$$\frac{\Delta v}{v_0} = \frac{\ln[1+\tilde{\eta}^{(0)}(T_A)t_A]}{\gamma v^*/v_0 + \ln[1+\tilde{\eta}^{(0)}(T_A)t_A]}, \tag{30}$$

where v^* is critical free volume fluctuation, γ is a geometrical factor, $\tilde{\eta}^{(0)}(T_A)t_A$ is annealing parameter which can be expressed as:

$$\tilde{\eta}^{(0)}(T_A)t_A = A_0 \exp(\tilde{Q}/RT_A), \tag{31}$$

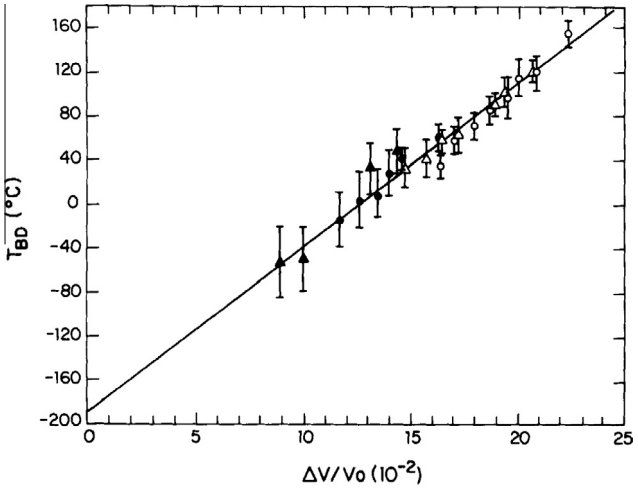

Fig. 28. The correlation between the brittle-to-ductile transition temperature T_{BD} of a $Fe_{79.3}B_{16.4}Si_{4.0}C_{0.3}$ glass as a result of isothermal annealing treatments at various annealing temperatures and the fractional change in free volume calculated from the model (reproduced from Ref. [204] with permission. ©1990. Taylor & Francis).

where $\widetilde{Q}$ is the apparent activation energy, A_0 is a prefactor that depends on initial configuration state. By assuming a minimum free volume for ductility, a linear correlation between DBT temperature T_{DB} and free volume change $\Delta v/v_0$ is found:

$$T_{DB} = \frac{v_0}{\alpha\Omega}\left(\frac{\Delta v}{v_0}\right) + \text{constant}. \tag{32}$$

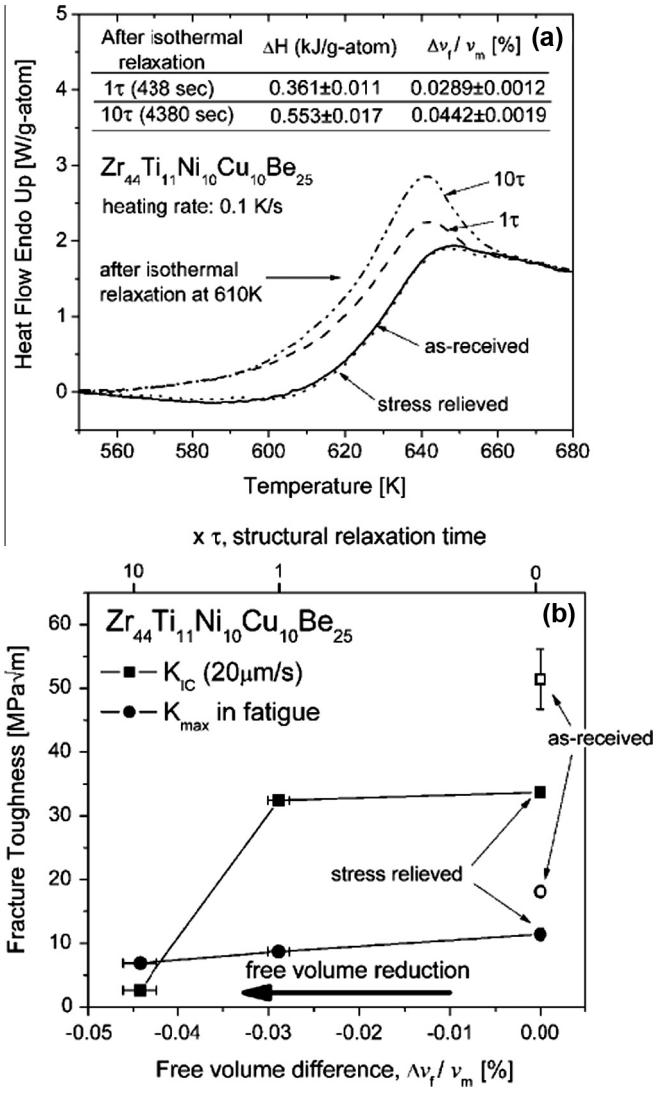

Fig. 29. (a) The enthalpy recovery measurement in the glass transition region after isothermal relaxation at 610 K for 1τ and 10τ of the $Zr_{44}Ti_{11}Ni_{10}Cu_{10}Be_{25}$ BMG, respectively. Quantification of the free volume relaxation are reported in the table (inset). (b) The measured fracture toughens versus free volume changes after the annealing of this alloy (reproduced from Ref. [203] with permission. ©2008. Elsevier).

This correlation was experimentally verified by isothermal annealing a $Fe_{79.3}B_{16.4}Si_{4.0}C_{0.3}$ glass at different temperatures [see Fig. 28] and subsequently performing the bending tests [204]. We additionally note that annealing embrittlement is gradual and systematic process, and to a large extent is associated with the relaxation of glass to an equilibrium configuration. In contrast, DBT is sharp and abrupt as it more closely resembles a "phase transition".

Some indirect methods such as differential scanning calorimetry (DSC) and positron annihilation spectroscopy (PAS) can be used to estimate the evolution of the amount of free volume. Suh et al. [205] used PAS to measure the free volume change during annealing of a Zr-based BMG. Both positron lifetime and Doppler broadening experiments revealed the decreased free-volume regions as a result of annealing. Meanwhile, plane-strain fracture toughness was significantly decreased and fatigue crack-growth rates were dramatically increased. The free volume annihilation during structural relaxation can also be reflected by enthalpy change before glass transition in DSC curve of a BMG. Van Den Beukel et al. [206] developed a model that describes functional form of the DSC curves based on free volume theory in which a similar exothermic peak is observed. According the model, an equilibrium free-volume v_{fe} exists for the supercooled liquid at a given temperature is:

$$v_{fe} = A(T - T_0), \tag{33}$$

where, T_0 is the ideal glass temperature and A is a proportionality constant. During the non-equilibrium processing, the as-cast alloy possesses an excess amount of free volume $v_f > v_{fe}$, which will annihilates and approaches v_{fe} in the continuous heating DSC experiments (See Fig. 29). The reduction in v_f, gives rise to the heat release ΔH, and they generally have a linear correlation [203]:

$$\Delta H = \beta \Delta v_f. \tag{34}$$

This has been experimentally verified by Slipenyuk and Eckert [207] and other researchers [190,203].

Free volume reduction is not the only factor responsible for the thermal-induced DBT. Other scenarios are proposed recently. For example, based on the cooperative shear model [56], Pan et al. [208] characterized the volume of STZs by the indention technique and found a close correlation between the ductility and the STZ volume in various BMGs as shown Fig. 30, where the larger STZ volume corresponds to more ductile BMGs with large Poisson's ratio [208]. They applied this concept to the structural relaxation process of a $Zr_{70}Ni_{16}Cu_6Al_8$ BMG and found that the measured STZ volume dramatically decreases upon annealing, which is consistent with the relaxation-induced embrittlement [209]. This idea has also been corroborated by the molecular dynamics (MD) simulations on

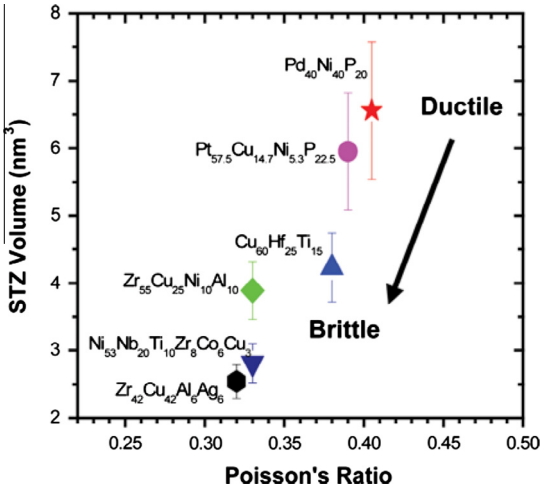

Fig. 30. The correlation between the measured STZ volume and the Poisson's ratio in BMGs. The STZ volume of plastic flow are found to increase with Poisson's ratio (reproduced from [208] with permission. ©2008. National Academy of Science).

the fracture of a model glass by Falk et al. [26,210] and other experimental studies [210,211]. Recently, Rycroft et al. [212] theoretically calculated fracture toughness of metallic glasses as a function of the degree of structural relaxation at different annealing times near the glass transition by solving complex free-boundary problems on the STZ model of plastic deformation. Their results show that there exists elastoplastic crack tip instability for sufficiently relaxed glasses, resulting in a marked drop in toughness, which can be interpreted as thermal-induced DBT similar to experimental observations.

BMGs are also prone to DBT upon lowering test temperature below a critical temperature, similar to the DBT commonly observed in bcc crystalline metals [22]. As illustrated by Raghavan et al. [213], the impact toughness of Vitreloy 1 undergoes an abrupt reduction when the testing temperature is below 150 K. One important feature of the temperature-induced DBT is that it occurs in an abrupt manner rather than in a gradual way. This can be generally interpreted from the Ludwik–Davidenkow–Orowan hypothesis that could explain many aspects of DBT in the mechanical behavior of conventional materials. The hypothesis assumes that the brittle fracture occurs when the yield stress of the material exceeds a critical value. Brittle fracture (fracture strength σ_F) and the yielding (yield strength σ_Y) are assumed to be independent processes with different dependence of σ_F and σ_Y with temperature or other variables. The intersection of the two strengths defines the position of DBT. Usually, the σ_Y depends on temperature in a pronounced manner while the σ_F is insensitive to temperature and usually determined by the modulus of the material. Therefore, the DBT usually occurs in the abrupt manner. For crystalline alloys, the DBT upon lowering temperature is explained in term of reduced dislocation activity at low temperatures [214]. For BMGs, however, the abrupt reduction of toughness should be associated with the suppressed plastic deformation or shear band activity at lower temperatures [213,215], which results in the rapid variation of the yield strength. There are also reports on the anomalous brittle-to-ductile transition observed in some BMGs, such as in an Au-based BMG where the alloy becomes more ductile upon lowering the temperature [216]. The detailed origin responsible for this anomalous transition is still unclear and deserves further investigations.

4.3.4. Microalloying effects

Minor element additions or micro-alloying, which has a long history in metallurgical application, has also been well practiced in the field of metallic glass research [217]. Minor addition (usually below 2 at%) in BMGs has been found to significantly affect their glass-forming ability, thermal stability, strength, plasticity, fragility, corrosion resistance and physical properties [13]. The ductility and toughness of BMGs are also susceptible to the minor additions. For example, the minor addition of Al into a binary $Cu_{50}Zr_{50}$ metallic glass not only to increases its glass-forming ability, but also significantly improves its ductility, resulting in a large macroscopic plasticity under compression at room temperature [126,218]. Similar effects of plasticity enhancement have also been obtained by addition of Ti in CuZr metallic glasses [219], addition of Ta in ZrCuNiAl alloy [220], and additions of Hf, Zr, Si in $Ti_{50}Cu_{50}$-based metallic glasses [221]. Recently, Demetriou et al. [222] demonstrated that the glass-forming ability of a Pt-rich metallic glass can be greatly improved by only incorporating 0.3 at% Ag, as the critical rod diameter increases by more than twice. More interestingly, the resulting glass displays an unusual capacity for "liquid-like" deformation characterized by low resistance to shear flow and high resistance to cavitation, with extensive bending ductility in the absence of fracture and an estimated fracture toughness value of $\sim$125 MPa $m^{1/2}$. In contrast to the plasticity enhancement by the microalloying, the minor addition can lead to a sharp decrease of toughness in BMGs. For example, as illustrated by Kim et al. [168], both quaternary $Zr_{33.5}Ti_{24}Cu_{15}Be_{27.5}$ (Var1) and $Zr_{44}Ti_{11}Cu_{20}Be_{25}$ (Var2) BMGs that are derived from Vitreloy 1 have a high fracture toughness exceeds 80 MPa $m^{1/2}$. However, a small addition of Fe (0.5 at%) in Vitreloy 1 results in a significant degradation in the fracture toughness from 48.5 to 25 MPa $m^{1/2}$. The fracture toughness of these BMGs tends to exhibit a sharp "transition" with slightly varying composition. Garrett et al. [217] also studied the effect of minor addition of Si and Sn on the toughness of a Cu–Ti based metallic glass and reported a sharp decrease in the fracture toughness, even these minor additions can effectively improve the GFA of this glass [13].

A possible explanation for the microalloying effect is that it can alter the structural organization of the glass at the atomic level, not to be chemical but rather topological [16,223]. Indeed, the enhancement in GFA by microalloying has been found to correlate well with the changes in the medium-range

order of the atomic structure [13,16]. By minor adding some appropriate elements, the atomic-scale inhomogeneity can be induced in the glass structure, and consequently these inhomogeneities could serve as sites that facilitate the initiation of plastic flow, leading to profuse shear banding and the enhanced toughness. This idea has been recently modeled by Dasgupta et al. [223] in which the addition of some foreign atoms is viewed to act as the pinning centers in the glassy matrix that cause long-range elastic stress distribution. A very strong effect on the toughness is shown via the increase of both the shear modulus and the yield stress as a function of the density of pinned particles. This concept was experimentally demonstrated recently by Zheng et al. [224]. They find that the ductility of a Ti–Zr–Cu–Pd BMG is greatly enhanced by minor addition of relatively large atoms in size, and these adding larger atoms are believed to act as the "soften" local heterogeneities with less shear resistance.

The DBT induced by microalloying may also relates with the change of electronic structure [13,225]. Yuan et al. [225] investigated the evolution of bonding states for composition-induced DBT in a $ZrCuNiAlSn_x$ BMG by employing ^{27}Al NMR spectroscopy. As shown in Fig. 31, the ^{27}Al knight shifts, which reflects the degree of the hybridization of Al 3*p* with *d* states of TM (Cu or Ni), significantly change as a function of Sn addition, and this change correlates well with the variation of fracture energy. The Sn minor addition strongly perturbs the *sp* bands and the bond mobility, and thus affects the shear modulus and mechanical properties of the BMG.

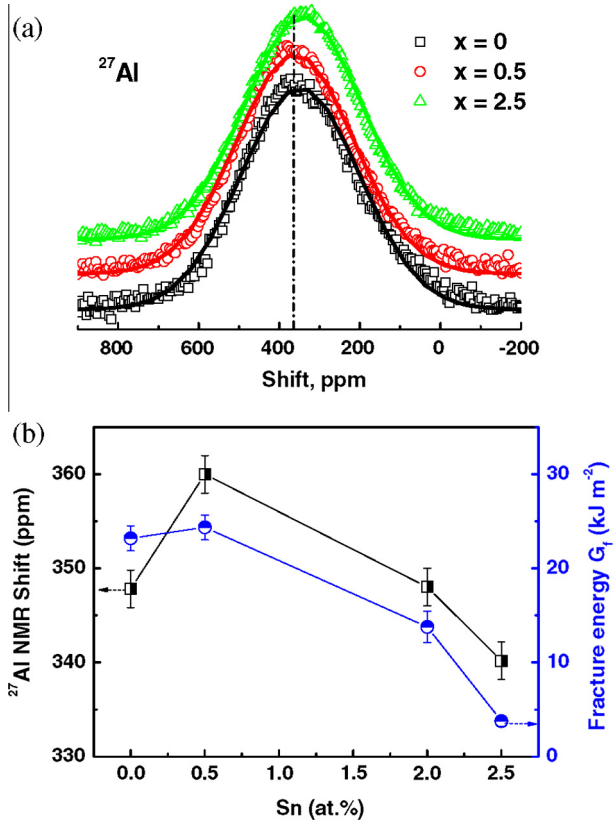

Fig. 31. (a) Representative ^{27}Al NMR central line shape of powder spectra of $Zr_{61}Cu_{18.3-x}Ni_{12.8}Al_{7.9}Sn_x$ MGs with $x = 0$, 0.5 and 2.5. The ^{27}Al NMR spectra are normalized to the maximum intensity for various Sn additions. The solid lines are fitted with Gaussian distribution. (b) The correlation of ^{27}Al NMR line shift (left coordinate) and fracture energy (right coordinate) with Sn addition (reproduced from [225] with permission. ©2011. American Physical Society).

4.4. Intrinsic correlation between elastic constant and fracture toughness

The nature of fracture toughness of BMGs is complex, which is not only related with compositions and structures, but also affected by internal states induced by preparing conditions, structural relaxation and so on. Due to the difficult to observe the changes of atomic structure during deformation and fracture process, a clear structure–property relationship similar with that of crystalline materials is still absent in BMGs [17]. Therefore, it is important to find some parameters, which are easily measured and quantified, to comprehensively reflect the effects of structure and internal states on the toughness [18]. The elastic moduli of a glass are related to the curvature of the potential energy minima and the anharmonic force contributions [226,227], and are very sensitive to structure change (especially the SRO and MRO) and the atomic bonding [227]. In crystalline metals, it has long been known that the intrinsic plasticity correlates with the ratio of the elastic shear modulus G to the bulk modulus B, G/B, or equivalently the Poisson's ratio ν, as the two parameters are related by $G/B = (3/2)(1-2\nu)/(1+\nu)$ for isotropic materials [103,228]. At low temperatures, the plastic flow occurs by glide of dislocation on the close-packed planes and the resistance to plastic flow is controlled by G, while the brittle fracture which often involves the tensile separation of non-close packed atomic planes due to the dilation caused by hydrostatic stress state near the crack is controlled by B [103]. Thus, higher G/B favors brittleness and vice versa. This correlation has been verified by ranking the data of polycrystalline pure metals from ductile (e.g. Ag, Au, Cd, Cu) to brittle (e.g. Be, Ir) behavior as G/B increases [229]. Rigorous and quantitative analysis has been carried out by Kelly et al. [230], Rice and Thomson [228,231]. Similar studies on the relationship between E and shear modulus or Poisson's ratio for cracked brittle materials (such as ceramics) have also been reported [231].

The correlation between G/B or ν and toughness is also applicable to BMGs. As early as 1975, Chen et al. [232] had pointed out that the high Poisson's ratio are responsible for the ductile behavior of many metallic glasses. Lewandowski, Wang and Greer [103] summarized the data of toughness and elastic moduli of μ/B (shear modulus is also often represented by μ) and ν for various BMGs, as shown in Fig. 32(a). As the failure is energy-limited rather than load-limited [176], the appropriate material index for the toughness is not K_C, but rather the fracture energy G_C. $G_C = K_C/(1-\nu)$ under the plane strain state, where ν is the Poisson's ratio. G_C is the energy required to create two new fracture surfaces, and for ideal brittle materials, $G_C = 2\gamma$ with γ being the surface energy per unit area [103]. From Fig. 32(a), the correlation between the ratio μ/B and the toughness can be well seen. Higher μ/B favors the toughness or plasticity of BMGs. With low values of μ/B, the glasses based on Zr, Cu or Pt all have fracture energies in excess of 1 kJ m^2, exhibit extensive shear banding during deformation. While those Mg-based or Fe-based BMGs, which approaches the ideal brittle behavior ($G_C = 1$ J m^2) of oxide glasses, have high ratio μ/B. A critical value for μ/B, that divides the brittle and ductile fracture, lies in the range of 0.41–0.43. The correlation between the fracture energy and the elastic constants can also be expressed in terms of Poisson's ratio. Higher values of Poisson's ratio give higher fracture energy, and the critical Poisson's ratio for the transition between brittle and tough regime is 0.31–0.32 [74,110].

It should be noted that the data is little more diffuse as a wide range of glass compositions is used. There is much scatter in the measured values of G_c due to the difference in experimental factors and preparing conditions. To eliminate the composition as a state variable, the correlation was also tested in annealing process of a single BMG [103]. As presented in Fig. 32(b) on Vitreloy 1, the annealing-induced embrittlement correlates well with the change of μ/B. The critical value of μ/B for the abrupt drop of the toughness is also similar with that found in the different glasses. Gu et al. [233] extended the correlation between the toughness and Poisson's ratio to individual Fe- and Ti-based BMGs which display crossover from brittle to ductile transition with the alloy contents. An anomalous compositional dependence of elastic moduli was found considering the elastic moduli of alloying elements and the same critical value of ν or μ/B was obtained, which corresponds well to the transition from brittle to ductile behavior of BMGs. The correlation has also been reported in other BMGs systems where the internal states are tuned (such as varying formation conditions) [22,192]. The increased trend of the toughness with μ/B or the Poisson's ratio in BMGs reflects the similarity in the deformation and fracture mechanism between various metallic glasses with marked difference in toughness [18,103].

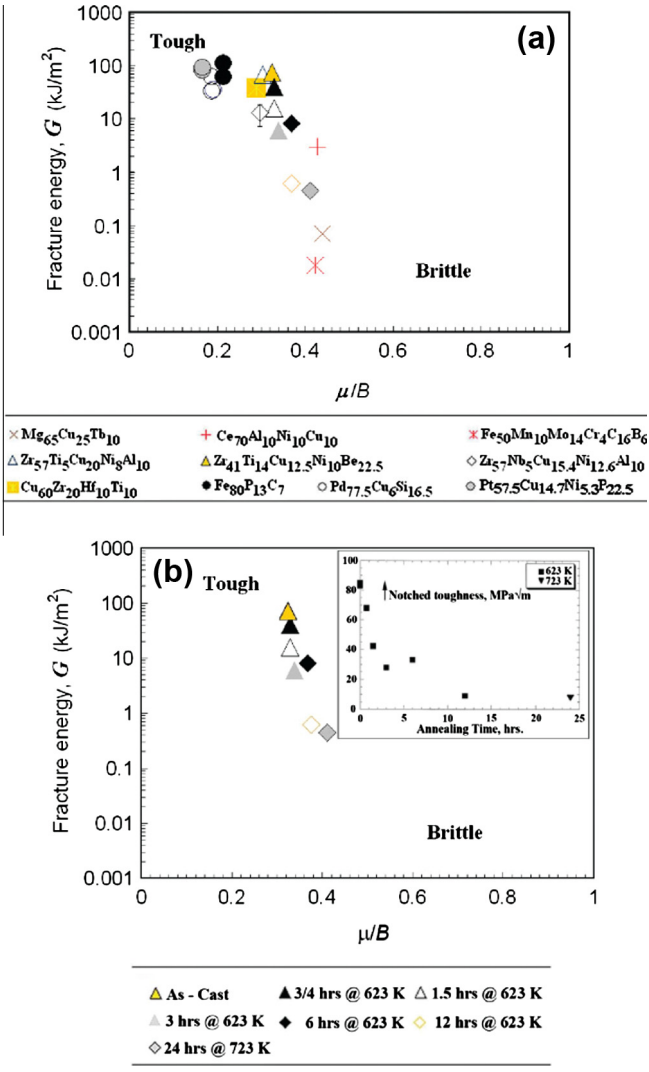

Fig. 32. (a) The correlation of fracture energy G with elastic modulus ration μ/B for all as-cast (unannealed) metallic glasses (compositions listed in at%). (b) The correlation of fracture energy G with the ratio μ/B as the Vitreloy 1 is annealed. The inset shows the decrease in notch toughness as a function of annealing time (reproduced from Ref. [103] with permission. ©2005. Taylor & Francis).

The physical origin for the correlation between the toughness and the Poisson's ratio lies that the plastic flow and fracture behavior are closely related with the elastic properties of metallic glasses [18]. The plastic flow of metallic glasses occurs through the cooperatively shearing of unstable STZs under shear stress, and the energy barrier for the plastic flow links the instantaneous G [18,56]. Wang et al. [234] also proposed an extended elastic model for the plastic flow in BMGs from the view of energy landscape. According to the elastic model, the flow activation energy in BMG is determined not solely by shear modulus but also by bulk modulus as $\Delta E \propto (10\mu + B)/11$. These models indicate that a lower value of μ implies the weak resistance to the plastic shear. While the B is a reflection of the resistance to the dilation during mode I fracture. Thus, the correlation can be interpreted in term of the competition between plastic flow and fracture, or in terms of shear and dilation. The higher

value of v suggests an increased tendency for plastic flow over the fracture in BMG, and thus a higher toughness. Recently, it is found that the Poisson's ratio also correlates with the measured STZ volume in six BMG systems indicating the intrinsic correlation between the Poisson's ratio and the ductility in BMGs. As a constant elastic strain (~2%) is required for the formation of an embryonic shear band in BMGs that consists of a local collection of STZs, a large STZ volume, when compared with a small one, enables a smaller numbers of STZs to be activated for the nucleation of a shear band in the yielding of BMGs. Consequently, the large sized STZs reinforce the shear capability of BMG and promote the formation of multiple shear bands, which concurs with the fact that a higher Poisson's ratio represents a higher possibility for the material to shear under applied stress [18,208]. In addition, it has been argued that the Poisson's ratio is linked with the nature of chemical bonds in metallic glasses [235]. The low v values seem to be associated with a covalent-like contribution to the chemical bond, which has a "rough" energy surface in energy landscape model and a more difficult movement among structure units, as expected for metal–metalloid metallic glasses. As a result, the plastic flow becomes difficult and the material shows a brittle behavior. On the other hand, a higher Poisson's ratio is often related to a more isotropic bonding behavior, where a more "flat" energy landscape is expected and the plastic flow becomes easier [18,235].

To measure the capacity for shear flow or the number of net shear-transformation events before the cavitation of an operating shear band for different BMGs, a dimensionless parameter f, defined as the $f = \exp[-(W_s - W_c)/k_BT]$, has been recently introduced, where W_s and W_c are the activation energy barriers for shear flow and cavitation, respectively. By further assuming the shear flow barrier $W_s \sim 37k_BT_g$ [56] and the ratio of barrier height W_s/W_c is dominated by the ratio of respective elastic curvatures B/G, f can be further expressed as:

$$\log(f) \sim \frac{W_s}{k_BT}\left(\frac{W_s}{W_c} - 1\right) \sim \frac{T_g}{T}\left(\frac{B}{G} - 1\right), \tag{35}$$

where f is estimated for a set of ten BMG alloys (including $Pd_{79}Ag_{3.5}P_6Si_{9.5}Ge_2$ BMG) with values of fracture toughness varying over two orders of magnitude, and the f is found to show a one-to-one correspondence with the plastic zone size r_p. This indicates that the f is a good measure of the capacity for shear flow before cavitation in shear bands. Interestingly, the ratio of B/G (or equivalently, the Poisson's ratio), which has been identified to be a key parameter associated with the fracture toughness of BMGs, also appears in the expression of f in Eq. (35).

All evidences indicate that the elastic moduli could indirectly reflect the atomic-level structure in BMGs and thus have a close correlation with the toughness/ductility. The established trend between the plastic deformation and elastic constants could assist in elucidating flow and fracture mechanism, in understanding annealing-induced embrittlement in metallic glasses, and guiding alloy design to alleviate brittleness [18,103].

4.5. Intrinsic and extrinsic toughening of BMGs

The BMGs have much higher strength and elastic limit than those of their crystalline counterparts, which are very attractive in structural applications. However, exploiting these superior mechanical properties of BMGs is largely limited in practices by their intrinsic brittleness or poor ductility arising from the shear localization and work softening, even the combination of these properties could yields a high toughness comparable to that of crystalline alloys. In past decades, tremendous efforts have been made to improve the toughness/ductility of BMGs and to explore their application as structural materials. The approaches employed can be generally classified into intrinsic toughening and extrinsic toughening. The former mainly involves those techniques to achieve high toughness/ductility in monolithic glassy phase, often by gradually tuning the structure or the composition in BMGs; the latter are resort to the introduction of secondary phases into the BMG to enhance its crack shielding ability, both of which are discussed below in details.

4.5.1. Intrinsic toughening of BMGs

By the investigation on available data of various BMGs, Wang et al. [145] show that the elastic constants of a BMG can be roughly predicted by a weighted average of the elastic constants of its constitute elements. The "rule of mixture" can be expressed as

$$M^{-1} = \Sigma f_i M_i^{-1}, \tag{36}$$

where M can be any elastic constant of the BMG, and M_i and f_i denotes the corresponding elastic constant and the atomic percentage of the constituent, respectively. This simple rule indicates that BMGs can be considered as highly dense packing structure [10]. In searching for BMGs compositions with a high intrinsic toughness, the aforementioned correlation between the Poisson's ratio v is a useful guideline as it is possible to obtain the high v in BMGs by appropriately adjustment of the composition in known or unknown BMG-forming alloys based on the rule of mixture of elastic constants [18]. This strategy has been successfully applied to ZrCuNiAl BMG-forming system by Liu et al. [125] where the ductile BMGs were synthesized on the basis of the appropriate choice of composition for controlling Poisson's ratio. The excellent plastic BMGs with relative high Poisson's ratio are found to possess a unique microstructure composed of strongly bonded hard regions surrounded by weakly bonded soft region, which render the BMG undergo the true strain larger than 30% without failure, a feature that could only be observed in high temperatures [18,125]. However, it is worth noting that although the "rule of mixtures" can be used to roughly estimate the magnitude of the elastic moduli of BMGs of different alloy systems, it seems fail to capture the elastic moduli of BMGs with varying compositions in a single alloy system, as recently studied by Liu and Zhang [236]. They found an almost linear softening of elastic moduli of BMGs with the increasing content of the base element. It is possibly because that the "rule of mixtures" usually utilizes the elemental properties in their crystalline state rather than in their amorphous state while metallic glasses may have intrinsic nanoscale fluctuations or heterogeneities structures, which is fundamentally different from their crystalline constitute elements. Based on this picture, they assume that the structure of BMG is composed of the tight-bonded clusters with higher stiffness and the base-element solvent matrix with loose bonding. A new "rule of mixtures" between the two phases could well resolve the observed softening with the increased content of base element in a single metallic glass forming system.

The rule of mixture can be used to design ductile BMGs by estimating their elastic constants, but such approach may not always lead to correct prediction [22], since the rule of mixture only considers the content of alloy elements or mixing phases, and ignores many important factors such as the heat of mixing particular pairs of elements in the glass formation [91]. As shown in Fe-based BMGs, the toughness can be significantly improved (K_{IQ} increased from 5.7 MPa $m^{1/2}$ to 52.8 MPa $m^{1/2}$) by systematic adjustment of composition and tuning the elastic constants. However, this dramatic change in toughness is only accompanied by a slight increase of v from 0.314 to 0.320 [237]. Kim et al. [168] showed that the fracture toughness in four Vitreloy-type BMGs with different chemistries exhibits significant variation, yet their elastic constants and yield strength are comparable. Nevertheless, the pursuit of higher Poisson's ratio remains worthwhile for achieving greater toughness [91]. The strong evidence is the recent development of a tough Pt-based BMG with $K_{IQ} \approx 125$ MPa $m^{1/2}$ [172] and of a tough Pd-based BMG with $K_{IQ} \approx 200$ MPa $m^{1/2}$ [122]. These alloys, without exception, all have an impressive high v (0.41–0.43), underpinning the validity of the correlation between elastic moduli and the fracture toughness in intrinsic toughening of BMGs.

4.5.2. Extrinsic toughening of BMGs

Some BMGs exhibit high fracture toughness, however their plastic flow is still localized into shear bands and undergoes shear softening during deformation. There are no intrinsic "microstructures" (e.g. the grain boundaries in crystalline alloys) in BMGs to act as barriers to inhibit shear band propagation and crack growth. The toughness of most BMGs, even some are comparable to engineering alloys, are regarded to be much low considering their high fracture strength. To further improve the intrinsic toughness of BMGs and overcome the intrinsic softening behavior, many extrinsic toughening methods have been developed in past decades. Among them, fabricating BMG composites containing the discontinuous crystalline phases is the commonly used. These secondary phases introduced into

the glassy matrix by different ways (e.g. *in-situ* devitrification or crystallization and *ex-situ* added) and in various forms (e.g. dendrite phases, particles or laminates) are effective to hinder shear band propagation and promote the initiation of new shear bands, thus increase the toughness/ductility of BMGs.

As early as 1990s, there have been some attempts made to develop "*ex-situ*" BMG matrix composites. Choi-Yim et al. [238] showed that Zr- and Cu-based bulk glass forming melts could be processed with dispersion of added particles or wires to create two-phase mixtures. By choosing some particulate phases (such as SiC, TiC, Ta or W) that react little with the melt, the composition and properties of the glass matrix were unaffected, and they showed that the formed composites display some improvement in compressive plasticity over the monolithic BMGs, but no significant plastic flow in tension tests [91,239]. The major breakthrough in the BMG composites is the development of "*in situ*" BMG matrix composites, where the primary crystalline phases are devitrified from glass-forming melt upon cooling, and the residual liquid then solidifies as the BMG matrix. Hays et al. [240] pioneered the work by *in situ* devitrification of the melt of Vitreloy 1 enriched by Zr, Ti and Nb. The resultant composite contains a ductile bcc β phase which distributes in the glassy matrix homogeneously in the form of dendrites with the trunk length of 50–150 μm and secondary dendrite arm spacing 6–7 μm. The volume fraction of the dendrites is about 25%. The ductile and soft secondary phase are very effective in mechanically stabilizing shear localization and crack propagation in the composite, yielding a dramatic improvement of plasticity in compression and bending tests compared to that of the monolithic Vitreloy 1. More importantly, the composite exhibits a significant tensile plastic strain of approximately 5%, in contrast to the zero tensile ductility of monolithic BMGs. As shown by Flores et al. [241], the BMG matrix composite also has a much higher fracture resistance (approximately double the toughness of the glassy matrix material) and fatigue endurance limit than that of matrix materials. Later, Hofmann et al. [143] found that the morphology of dendrite phase (characterized by the dendrite size L and inter-dendrite spacing S) has an important influence on the plastic flow and fracture behavior of BMG matrix composites, and the optimal length scales L and S should be less than, but of the order of the characteristic plastic zone size, R_p (estimated from Eq. (26)) in the crack tip of the matrix glass. They successfully synthesized a series of Zr–Ti-based BMG matrix composites (denoted as DH1, DH2 and DH3 in Fig. 33) by matching fundamental mechanical and microstructure length scales with a semi-solid processing technique. The designed composites exhibit room-temperature tensile ductility exceeding 10%, yield strengths of 1.2–1.5 GPa (see Fig. 33), K_{IC} up to 170 MPa $m^{1/2}$, and fracture energies for crack propagation as high as $G_{IC} \approx 340$ kJ m^{-2}. The K_{IC} and G_{IC} values equal or surpass those achievable in the toughest titanium or steel alloys. They also successfully developed low-density Ti-based BMG composites with tensile ductility by the similar strategy [143].

However, the tensile ductility achieved in some BMG matrix composites still displays macroscopic strain softening behavior with an early onset of necking as shown in Fig. 33(c). The lack of work

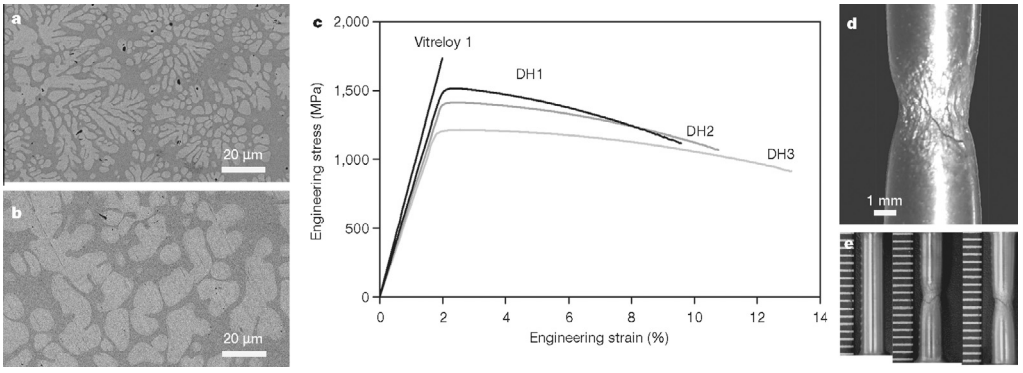

Fig. 33. The backscattered SEM micrographs showing the microstructure of BMG matrix composites of DH1 (a) and DH3 (b), respectively. (c) Engineering stress–strain curves for Vitreloy 1 and DH1, DH2 and DH3 in room-temperature tension tests. (d) Optical micrograph of necking of DH3 during tension (reproduced from Ref. [141] with permission. ©2008. Nature Publishing Group).

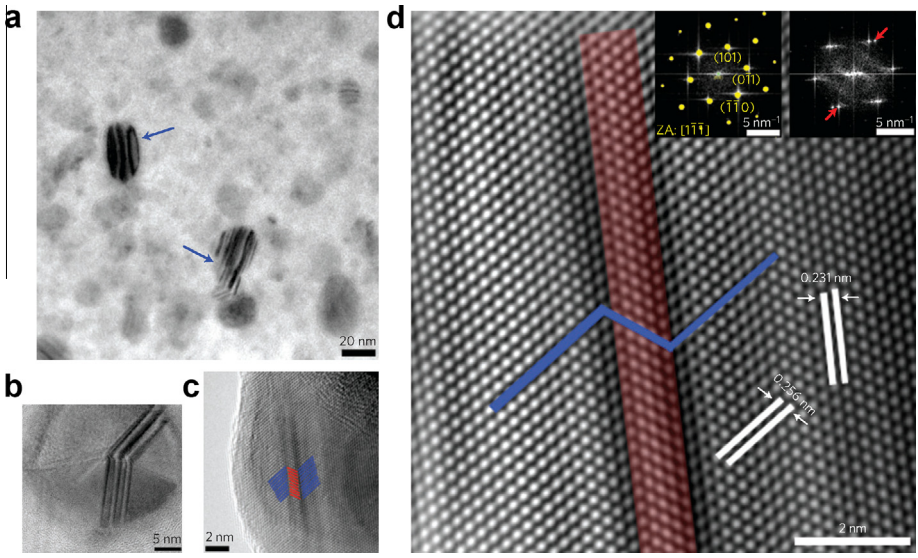

Fig. 34. The microstructure of a $Cu_{47.5}Zr_{47.5}Al_5$ BMG specimen with work hardening behavior deformed to fracture. (a) The low resolution TEM micrograph reveals that the nanocrystals with size between 10 and 50 nm after fracture. (b and c) The twinning of nanocrystals at a higher magnification. (d) The high-resolution micrograph reveals the stacking sequence of lattice planes, corroborating the presence of twins (reproduced from Ref. [242] with permission. ©2010. Nature Publishing Group).

hardening mechanism endows the material with minimum damage tolerance and gives rise to serious engineering problem [142]. Recently, Pauly et al. [242] developed the Cu–Zr based BMGs with a pronounced work hardening ability in tension, which can be attributed to the precipitation of B2-structure CuZr nanocrystals during deformation and their subsequent twinning (see Fig. 34), a mechanism similar to the transformation-induced plasticity (TRIP) in steels [243]. The transformation-mediated plasticity was also reported in parallel by Wu et al. [142] and other researchers [244,245] in CuZr-based BMG matrix composites where micrometer-size B2 crystalline particles undergo the martensitic transformation during deformation and induce large tensile ductility (as large as 10%) and significant work hardening ability. This unique deformation mechanism, which is believed to be not just limited to Cu–Zr based BMGs, offers a new paradigm for developing BMG composites as engineering materials.

Another toughening method is to fabricate BMG composite in the form of laminates. In 1990s, the $Ni_{79}Si_{80}B_{12}$ glassy ribbons (few tens of μm thick) were interleaved with polycrystalline copper. This geometry significantly enhances the crack growth resistance with respect to monolithic metallic glasses and induces the formation of multiple shear bands, leading to an estimated plastic strain of 4.2% before rupture in tension. Similar laminate composites are also reported, where the metallic glassy layers were laminated with various crystalline layers [91,246] or fiber/epoxy layers [247]. Significant ductility or toughness improvement were also observed, for example, the laminate composites of Vitreloy 1/crystalline (Nb, Zr and Al) layers display a toughness of 70 MPa $m^{1/2}$, much higher than that of monolithic BMGs [246]. Considering size effect on the plasticity of metallic glasses, the improvement on the ductility should be much better if the thickness of glassy and crystalline layers is reduced to nanoscale. This has been recently verified by Wang et al. [248], and they developed a Cu–Zr nanolaminate which consists of alternate 5 nm thick glassy $Cu_{75}Zr_{25}$ layers and nanocrystalline Cu (about 35 nm thick) with the magnetron sputtering technique. Such a composite displays a nearly elastic-perfectly plastic behavior without necking and a tensile elongation of 13.8 ± 1.7%. More interesting, the shear band instability is no longer observed in the 5- to 10-nm-thick nanolaminate glassy layers and the amorphous-crystal interfaces exhibit unique shear (slip) transfer characteristic, fundamentally different from those of grain boundaries. Donohue et al. [249] also obtained similar results in a nanolaminates of $Pd_{77}Si_{23}$ glassy layers and nanocrystalline Cu.

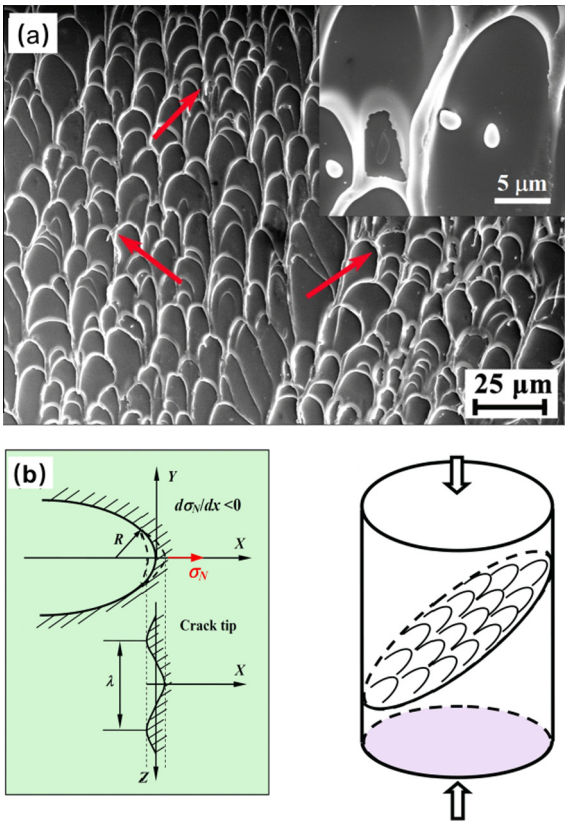

Fig. 35. (a) The fracture surface of a typical Zr-based BMG showing the vein-like pattern. The arrows and the inset shows the liquid features distributed in the pattern. (b) The illustration of the fluid meniscus in the crack tip and the formation of vein-like pattern during fracture (reproduced from Ref. [132] with permission. ©2012. American Institute of Physics).

5. Fracture surface morphology

After fracture, the crack propagation will leave some traces or patterns on the fracture surface of materials [19,20]. The fracture surface morphology provides important information on dynamic fracture process and fracture mechanism. The investigation of the fracture surface morphology has been one of the most direct and effective methods to understand the fracture behavior and mechanism of materials. In parallel with their remarkable and diverse mechanical properties, BMGs also exhibit unique and diverse fracture surface patterns such as vein-like patterns, nano- to micro-scale striations and periodic corrugations [98,139,142,214–222]. Some nanoscale structures such as nanocones, nanospheres and nanowires are also observed on the fracture surface of different BMGs depending on their ductility, toughness, deformation rate, and fracture mode. BMGs thus are model systems for studying the origin of surface roughening and the crack instability in the fracture of disordered glassy materials. In addition, these patterns also closely correlate with other fracture properties (e.g. the toughness) in BMGs [139], and provide important information for understanding possible plastic flow and fracture mechanism of this material. In this section, we introduce the main features of these fracture patterns. The formation mechanism of these patterns and their implication for understanding the dynamic fracture process and crack instability are also discussed.

5.1. Vein-like or dimple patterns

Vein-like pattern, which is also called the dimple structure, is the mostly observed surface morphology on the fracture surface of BMGs, especially on some load-constrain deformation modes (i.e. compression, bending modes). A SEM micrograph of the vein-like pattern for a typical Zr-based BMG after the catastrophic failure in the compression test is shown in Fig. 35 [132]. The patterns can be found on the whole fracture surface. In the edge of the fracture surface, the pattern slightly varies, changing into the "river-like" pattern. Similar features can also be observed in the fracture surface of other BMG systems such as Ti-, Pd-, Cu-based BMGs [22]. The shape of the pattern is analogous to the fracture features formed by separation of the grease between two solid plates of materials [250]. And it is believed that the formation of the vein-like pattern is closely related with the significant softening or reduced viscosity in the shear bands, which is similar to the case of a thin viscous layer between two solids (such as a layer of honey between two glassy plates) [250]. The origin responsible for the softening can be largely attributed to shear-induced structural disordering or temperature rise. Experimental studies on the shear banding before the final fracture indicate that the structural disordering may be the main cause of the softening, and the temperature rise seems to be the consequence of the softening. However, in the final fracture stage, the temperature rise is still believed to be significant, since the whole elastic energy stored in the sample is released instantaneously during the runway fracture, and may dissipate as the heat when the final fracture occurs. Actually, some liquid features such as molten droplets and wires are observed in the vein-like pattern [see the inset of Fig. 35(a)], indicating that the temperature at least reaches the melting point of the materials during catastrophic failure. The temperature rise during the unstable fracture process can be roughly estimated if the elastic energy release is assumed to be fully converted to the heat in the fracture plane. For compression tests, the total elastic energy per unit volume can be expressed as $\Delta E_c = \sigma_y \varepsilon_{el}/2 = E\varepsilon_{el}^2/2$, where σ_y is the yield stress, and ε_{el} is elastic strain at yielding. In the case of Zr-based BMGs, $E \sim 90$ GPa and $\varepsilon_{el} \sim 2\%$, one get $\Delta E_c \sim 18\ \mathrm{J\ cm^{-3}}$. Assuming the volume specific heat $c_p \sim 3\ \mathrm{J/K\ cm^3}$ and the thickness of the fracture plane $\lambda \approx 2\ \mu\mathrm{m}$, the estimated temperature rise reaches thousands of degrees [132]. This was verified by the direct measurement of temperature with high-speed infrared camera or other techniques [50,52].

The glass phase in the front of crack tip can be treated as viscous fluid due to the significant temperature rise in fracture, and the blunt-up of crack tip can be viewed as a variant of ubiquitous fluid meniscus instability, where a fluid meniscus penetrating into another more dense fluid and breaking up into a series of fingers as initially discussed by Taylor [251]. Argon was the first to note this and analyze the critical conditions for the formation of vein-like patterns [28]. As shown in Fig. 35(b), the meniscus has a curvature of radius R at the steady state, which is governed by the surface tension χ and the negative pressure (suction) gradient $d\sigma/dx$. Considering a perturbation of the fluid meniscus by giving it an infinitesimal wave in the z direction with the wavelength λ and amplitude ε, this will produce a slight variation of the pressure at different points. The pressure difference can act as the driving force for the growth of perturbation. Theoretical analysis shows that the critical wave length for the growth of perturbation must satisfy

$$\lambda_{crit} = 2\pi\sqrt{\frac{\chi}{d\sigma/dx}}. \tag{37}$$

Any perturbation with an initial wavelength $\lambda > \lambda_{crit}$ will grow into a finger shape penetrating into the glassy materials in front of the crack tip, and finally develop into a stable vein-like pattern in the fracture surface. The significant temperature rise and a large negative pressure gradient along the direction of crack advancing are two indispensible ingredients for the formation of vein-like patterns during fracture.

The surface tension χ and the negative pressure gradient $d\sigma/dx$ reflect the fracture resistance of glasses and the externally applied load, respectively. In principle, the scale of the vein pattern on the fracture surface should be indicative of the toughness of given metallic glasses [8]. Indeed, the vein patterns have been observed in less tough metallic glasses (such as RE-, Mg-based BMGs) but appear in a much smaller scales or even in nanoscales [173]. For example, as shown in Fig. 36(a)–(c), the

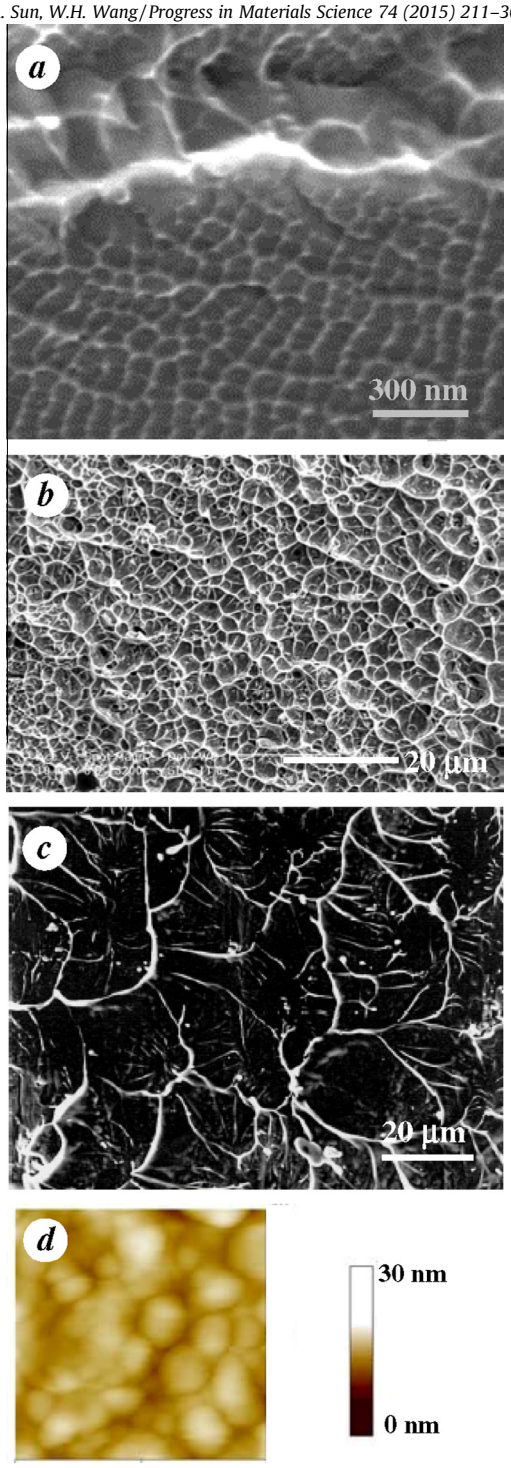

Fig. 36. The SEM image of vein pattern of the Mg-based BMG, (a) Ce-based BMG, (b) and a Ti-based BMG (c), respectively (d). The AFM image of dimple pattern corresponding to (a) (reproduced from Ref. [173] with permission. ©2005. American Physical Society).

average dimple size of a Ce-based BMG ($K_{IQ} \sim 10$ MPa $m^{1/2}$) is about ~5 μm, much less than that of Zr- or Ti-based BMGs. The nanoscale dimple structure (~100 nm) has also been observed on the fracture surface of Mg-based BMGs with almost ideally brittle behavior by SEM technique [see Fig. 36(b)] [173]. This suggests that for BMGs with extremely brittle behavior, the fracture still proceeds by a local softening mechanism but a much finer scale. With the available data, they find a correlation between the average dimple size w measured from the fracture surface and the fracture toughness K_{IC} in various BMGs [173],

$$w = \frac{1}{6\pi}\left(\frac{K_{IC}}{\sigma_y}\right)^2. \tag{38}$$

A further illustration of this correlation is shown in Fig. 37. The w measured as the average width of the dimple (or wavelength of vein features) of these glasses as single edge notched by tension or bending can be estimated directly from the SEM morphology of their fracture surfaces. As can be seen, w ranges from nm scale in extremely brittle Mg–Cu–Tb BMG to μm scale in tough Zr-based BMGs. Such a correlation also exists in the same sample measured at different temperatures. For example, in Pd–Ni–P BMGs, both K_{IC} and w decrease upon temperature and show a similar correlation [252]. So far the nature of structure feature that control the plastic zone size remains to be clarified, while the correlation permits the direct estimation of the toughness based on the plastic zone size on the fracture surfaces of BMGs [139]. The similar relation between the fracture surface morphology and the toughness are also studied by Suh et al. [253] in three-point bending of the precracked BMGs, where the length and roughness of the jagged region observed adjacent to the precrack correlate well with the plastic zone size. In addition, the correlation also indicates that, for metallic glasses, the failure at the microscopic level does not depend on stress and strain but involves a characteristic length related to the microstructure [173]. It is possible to get large plasticity in brittle metallic glasses as long as the cracks are within the process zone or the dimension size of sample is less than the characteristic length. This has been verified in Zr-based BMGs where thin ribbons show ductility in bending while its thick plates of the same composition show brittle fracture under similar loading [120]. It is believed that thin film Mg-based metallic glasses would be much tougher when their size is reduced to μm or nm scales comparable to the size of plastic zone. Indeed, significant plasticity has been recently observed during the compression of micro-sized Mg-based glassy pillars [101].

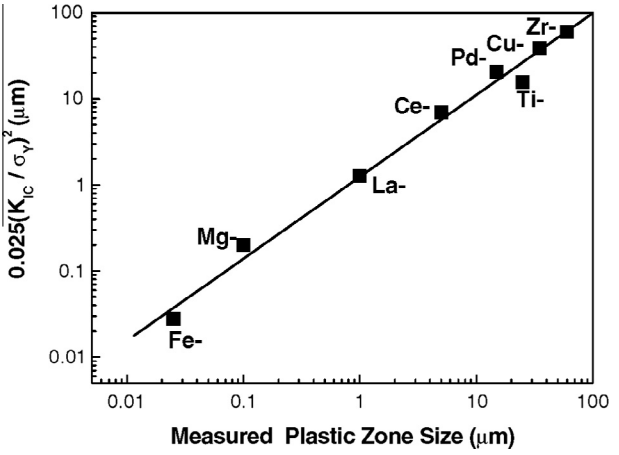

Fig. 37. The correlation between the fracture toughness and the plastic zone size estimated from the average dimple size on the fracture surface of various BMG systems (reproduced from Ref. [173] with permission. ©2005. American Physical Society).

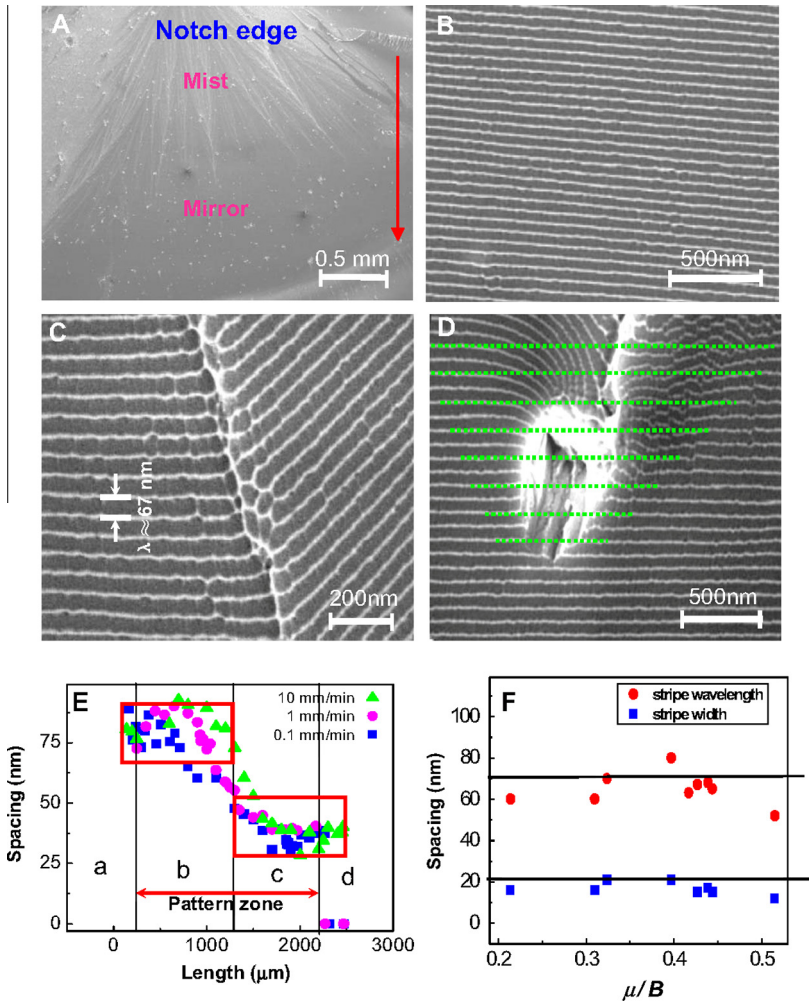

Fig. 38. (a) A typical fracture surface of Mg-based BMG shows distinct mist, transition, and mirror regions along the crack propagation direction (marked by arrow). (b) The typical periodic striped pattern on the mirror region. (c) The higher magnification of the encountering border. (d) The periodic striped pattern around a large flaw. (e) Size of the dimple structure or spacing of periodic corrugation d as a function of crack propagation distance L under different fracture rates V. (f) The wavelength and width of the stripes in metallic glasses with different ratios of μ/B (reproduced from Ref. [257] with permission. ©2009. American Institute of Physics).

5.2. Nanoscale periodical corrugations

In contrast to "tough" BMGs, the fracture surfaces of brittle BMGs (such as Mg-based, Re-based) are much flatter, which usually have two distinct regions: the mist zone and the mirror zone (sometimes the rougher hackle zone can also be observed) [see Fig. 38(a)] for single-edge notched samples under bending or tension [133]. In mist zone, the fractographies are mainly nanoscale dimple structures. While when one carefully examine the mirror zone by using high resolution SEM, a unique and beautiful nanoscale structure of periodical corrugations or stripes can be seen [254–256]. The typical features of the nanoperidical corrugations for a Mg-based BMG are shown in Fig. 38 [257]. The stripes are remarkably straight and periodical with an exact spacing of 70 nm [Fig. 38(b) and (c)], aligning along

the direction perpendicular to the crack propagation. Further AFM topography studies reveal that these nanostripes, are very shallow, with an average depth of around 12 nm. It is amazing that these stripes are almost perfect, and the ridges/grooves of the corrugation are smooth even at the nanoscale [258]. All the features indicate that the straight crack experiences a steady propagation state and remains nearly constant during the fracture process. In addition, the typical stripe period seems have no obvious relation with the loading modes (compression, tension or bending) or loading rates. For example, during compression of Mg-based BMGs, the sample shatter into many fragments, while approximately 80 nm period stripes can be readily found on the surfaces of the most pieces [138]. In bending tests, the stripe spacings are also nearly constant as the loading rate change from 0.01 to 10 mm min^{-1} [257]. Fig. 38(e) shows the stripe or dimple size of the Mg-based BMG as a function of crack propagation distance L at different loading rates V. It is obvious that the fracture surface shows four distinct zones with different fractographic feature from the notch point to the edge: dimple structure in zone *a*, periodic corrugation in zones *b* and *c*, and featureless zone *d*. The dimple structure in zone *a* has an average size of 70–100 nm. With the crack propagating, the dimple evolve into the periodic stripes with the spacing of 70 nm in zone *b* and 40 nm in zone *c*, and eventually decreases to zero in the featureless zone. The relative area of the four zones on the fracture surface can be changed with V. For instance, the area of dimple zone increases with increasing loading rates, and the mirror region outspread over almost the entire fracture surface. Nevertheless, the average spacing between period stripes keeps nearly constant of ~70 nm in zone *b* and ~40 nm in zone *c*, which is independent of V [218,219].

Similar nano-scale periodical feature is also widely observed in fracture surfaces of various brittle BMGs (such as Fe-, Dy-, Tb-, Ca-based) and even in relatively tough Zr-based BMGs [24,25,257]. Wang et al. [24] systematically examined the characteristic features of these nano-scale periodical stripes for various BMGs, and find that these stripes display nearly constant spacing λ (60–80 nm), stripe width w (10–20 nm) and stripe height h (5–10 nm), regardless of composition, sample size and the loading conditions. A typical example can be found in Fig. 38(f) and Table 4, which show the values of λ and w of the stripes for BMGs with markedly different mechanical properties as characterized by the ratio of shear modulus μ to bulk modulus B, μ/B. The values of λ and w as well as the ratio w/λ almost unchanged with the variation of μ/B, suggesting that the nanoscale periodic stripes generated in the dynamic crack propagation process is a common signature and a universal pattern formation mechanism for various BMGs, regardless of their loading conditions and mechanical properties [24,218]. The stripes are very robust and stable, and their periodicity and propagation direction are not obviously influenced by introducing flaws as shown in Fig. 38(d). This suggests that the straight crack front of the periodic stripe pattern is stable to the isolated perturbations of internal stress field during the dynamic fracture process.

Considering the remarkable similar characteristic of the nano-scale stripes observed in various BMGs, it is interesting to discuss their underlying formation mechanism which may be important to understand the dynamic fracture and crack propagation process in brittle BMGs. X-ray diffraction analysis of the fracture surface shows glassy nature, excluding the influence of crystallization on the fractographies [133]. The observed nanostripes cannot either be attributed to the Wallner lines that usually appear on fracture surfaces of brittle materials due to the interaction of crack propagation front with shear waves [259]. Since the oscillatory wave length for Wallner lines is $W = 2hVc_l/\sqrt{1-(V/c_l)^2}$, where h is the distance from the crack tip to the boundary, V is crack propagation speed and c_l is longitudinal wave speed. For BMGs, the V is estimated to be $(1.3-5.5)\times 10^{-3}$ m/s^{-1}, which is unreasonably low for generating Wallner lines [260]. By matching the area on both fracture surfaces through dedicate AFM and SEM observations (some flaws are chosen as the reference point, see Fig. 39), Wang et al. [133] show that the peak-to-peak separation during the formation of the nanostripes, rather than a peak-to-valley mechanism. This result indicates that local plastic deformation still plays a critical role in blunting initially shape crack where progressive local separation still occurs by a sequence of vein pattern formation, followed by plastic growth and linking of such vein patterns or coalescence of damage cavities along the extension of the crack. They then proposed that the formation of these nanostripes is a consequence of the failure of meniscus instability, which is determined by two competing factors: the initial wavelength of the perturbation

Table 4
Summary of observations of periodic striped corrugation in metallic glasses [249].

Metallic glasses (compositions in at%)	Experimental methods	Fracture mode	Stripe spacing λ (nm)	Width of stripes w (nm)	Double height $2h$ (nm)	w/d	μ/B	K_C (MPa m$^{1/2}$)	σ_Y (MPa)	Ref.
$Fe_{73.5}Cu_1Nb_3Si_{13.5}B_9$	Uniaxial tension of ribbon with a crack	I	~60	~16	...	0.27	~0.21	~5	>3000	[218]
$Mg_{65}Cu_{25}Gd_{10}$	Three-point bending of single-edge notched rod	I	~67	~15	~15	0.22	~0.43	~2	~672	[218]
$Mg_{65}Cu_{25}Tb_{10}$	Three-point bending of single-edge notched rod	I	~68	~17	~15	0.25	~0.44	~2	660	[257]
$Ca_{65}Mg_{8.5}Li_{10}Zn_{16.5}$	Three-point bending of single-edge notched rod	I	~65	~15	...	0.23	~0.44		530	[218]
$Tb_{36}Y_{20}Al_{24}Co_{20}$	Three-point bending of single-edge notched rod	I	~80	~21	...	0.26	~0.4		~1450	[218]
$Dy_{40}Y_{16}Al_{24}Co_{20}$	Three-point bending of single-edge notched rod	I	~63	...	~12	...	~0.42		~1110	[218]
$Zr_{41.2}Ti_{13.8}Cu_{10}Ni_{12.5}Be_{22.5}$	Planar shock wave; testing of thin disk	I	~70	~21	~20	0.26	~0.32	~86	1800	[135]
$Fe_{40}Ni_{40}P_{14}B_6$	Compression of a rod	I	~80	...	...	...	...		~2330	
$Ni_{42}Cu_5Ti_{20}Zr_{21.5}Al_8Si_{3.5}$	Compression of a rod	I	~60	~16	...	0.27	~0.31		~2800	[173]
$Fe_{65.5}Cr_4Mo_4Ga_4P_{12}C_5B_{5.5}$	Compression of a rod	I or II	~52	~12	...	0.23	~0.52	<5	~3000	[24]
$Mg_{65}Cu_{20}Ni_5Gd_{10}$	Three-point bending of single-edge notched rod	I	~50	~11	...	0.22	...	1–2	~400	[294]
Annealed $Fe_{73.5}Cu_1Nb_3Si_{13.5}B_9$	Three-point bending of a ribbon	I	~80	...	...	...	...			[249]

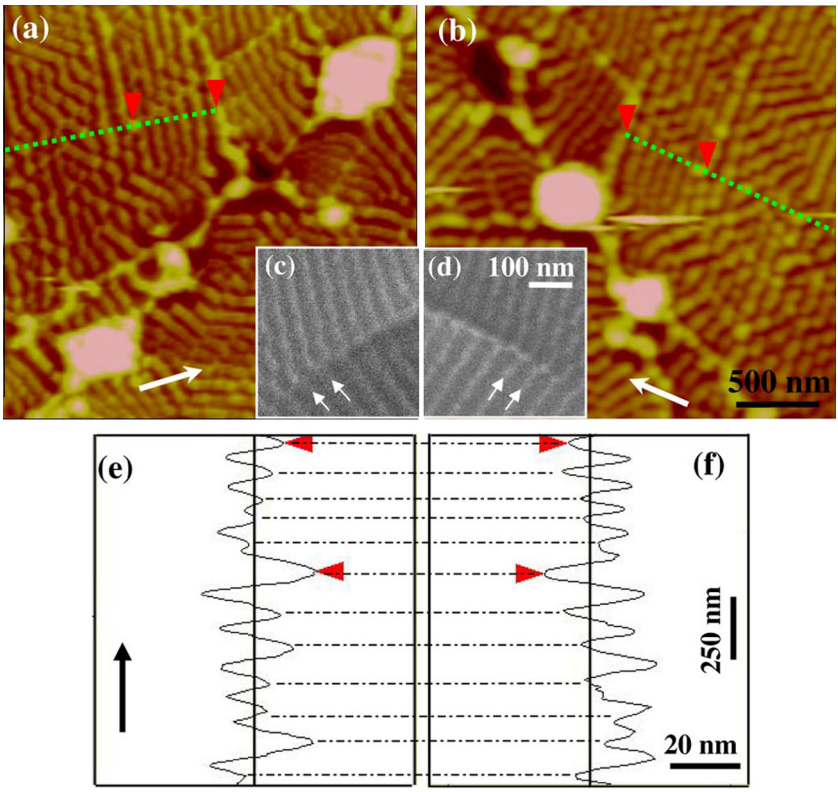

Fig. 39. The AFM and SEM observation reveals a peak-to-peak match during the formation nanoscale periodic stripes. (a and b) The comparison of left and right surface of Mg-based BMG observed by AFM. (c and d) The comparison of left and right surface of Mg-based BMG by SEM. (e and f) Section shapes of the corrugation along the dotted line in (a and b) (reproduced from Ref.[133] with permission. ©2007. American Physical Society).

of the meniscus λ and the radius of plastic zone in the front of crack tip R. The λ in the range of 60–80 nm can be regarded as the wavelength of the nanoscale corrugations, while R is related to fracture toughness K_{IC} by $R = 1/6\pi(K_{IC}/\sigma_Y)^2$ for the plane strain condition, where K_{IC} can be estimated from the crack tip open displacement (CTOD) during the fracture $K_{IC} = \sqrt{(CTOD)\pi\sigma_Y E/2.7}$. Near notch, for Dy- and Mg-based BMGs, the CTODs estimated from AFM measurements are 21.6 and 22.4 nm, respectively, and the R values respectively are calculated to be 89 and 104 nm, which are larger than or at least equal to the dimple size near the notch. The meniscus instability will develop into the dimple structure confined in the plastic zone due to the stimulation of microvoids once the maximum stress on the front of crack tip reaches the yield stress of the materials as shown in Fig. 40. With crack propagating, the dynamic process results in the change of fractography from the dimple to the periodic corrugation. The increase of the crack velocity is accompanied by the reduction of local K_{IC} and R, meanwhile the λ or the spacing of periodic corrugation is also reduced from about 80 to 35 nm. When $R < \lambda$, the plastic zone restrains the development of meniscus instability, and as a result, the periodic corrugation other than the dimple structure appears on the fracture surface. Similar scenario based on the competition between the meniscus instability and the cavitation was also proposed by Xia et al. [258] recently.

Inspired by the observations of the formation of the periodic patterns observed in various non-equilibrium systems such as oscillating granular and colloidal suspensions, it is proposed that the self-organized assemble of the fundamental units of nanoscale dimples at the crack tip could lead

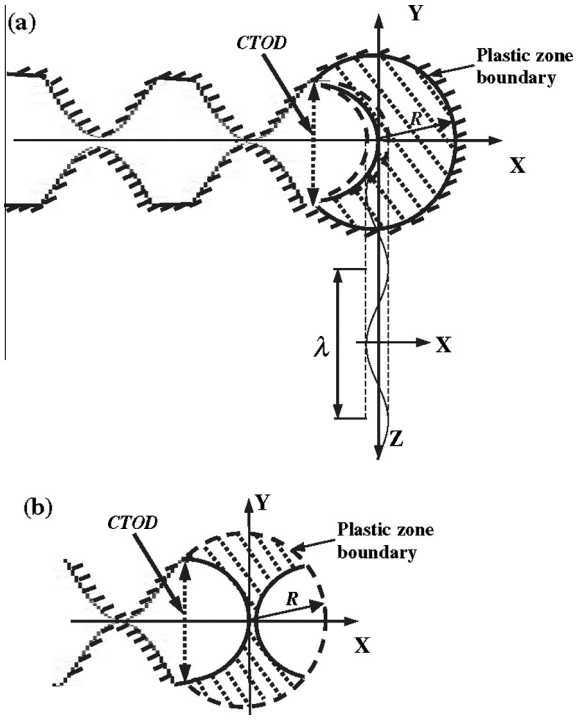

Fig. 40. Sketch illustrating the crack tip opening mechanism (crack propagates along the *X* direction). Crack extension by the peak-to-peak separation of the corrugation on the *X*–*Y* plane and the infinitesimal perturbation on the crack front on the *X*–*Z* plane. (b) The microvoid formation mechanism in the plastic zone (reproduced from Ref. [133] with permission. ©2007. American Physical Society).

to the formation of the periodic striped pattern on the fracture surface of various BMGs [257]. The STZs or flow units has been proved valuable for describing deformation physics of metallic glasses [46,65,66]. The similarity between stripe width/height and thickness of shear bands for various BMGs indicates that the nanoscale striped pattern is correlated with the basic unit of plastic flow. Due to relative motion of the basic flow unit, the plastic deformation in a metallic glass is analogous to that of randomly packed particles in a granular system. Under mode I loading, the fracture of metallic glass can be considered to occur in a confining liquid layer containing a collection of flow units in a grease model. The case is similar to nanoscale bilayer granular thin film confined to two rigid plates. It has been shown that the bulk block copolymer systems, granular materials and colloidal suspensions can all display periodic striped pattern under the influence of shear (see Fig. 41(D1)–(D5)), and the use of shear to induce alignment is a powerful strategy for producing high-quality masks for nanopatterning applications. By analogy to the shear-induced alignment patterns in variety of granular materials, the periodic striped pattern in metallic glass could be regarded as an orderly assembly of numerous individual and regular dimples highly confined between two flat fracture surfaces under shear. Nevertheless, the above proposed models generally stay in a qualitative level, a comprehensive and quantitative understanding of the formation of nanoperiodic stripes, combining the dynamics of crack propagation and micromechanism for plastic flow and fracture in BMGs, still needs further studies.

5.3. Other fracture patterns

In addition to the vein-like patterns and nanoperiodic corrugation introduced above, there are many other patterns that could appear on the fracture surface of BMGs. These patterns can only be

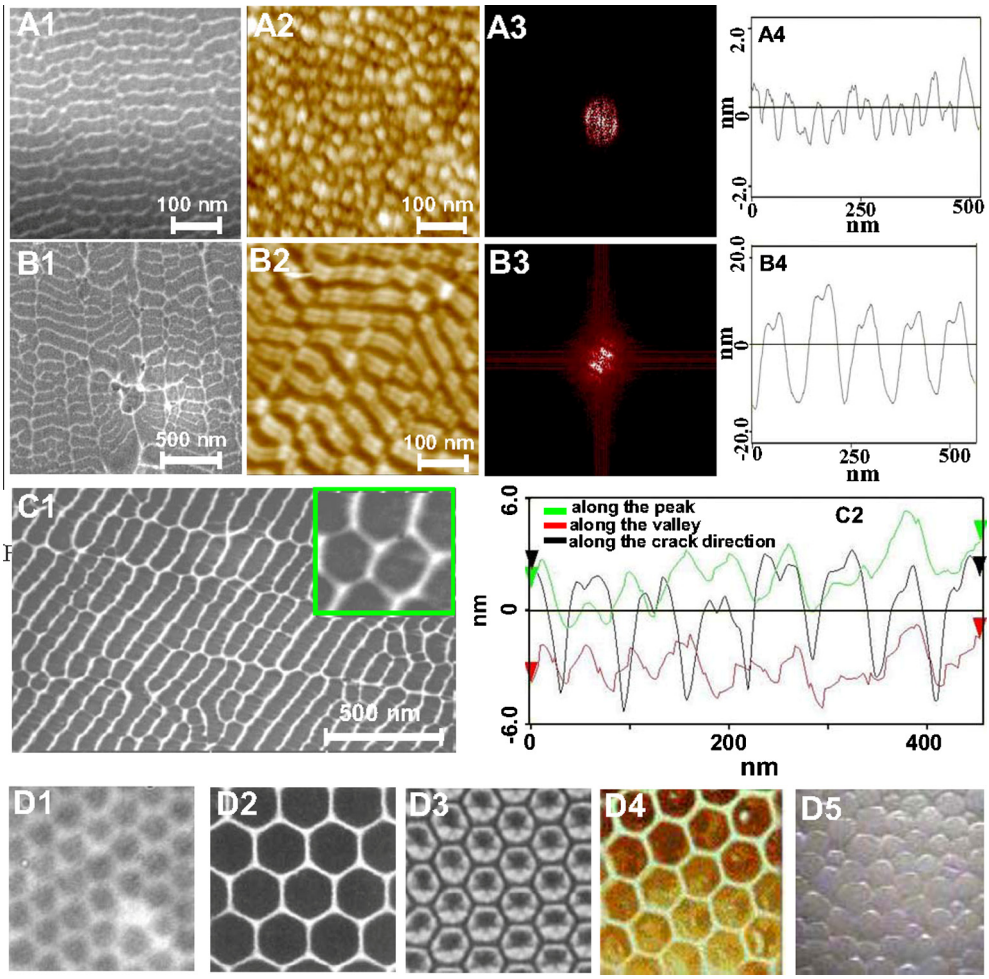

Fig. 41. The formation mechanism of nanoscale periodic stripes based on the self-organized STZs. (A1 and B1) are the SEM observations, respectively. (A2 and B2) are the AFM observations, respectively. (A3 and B3) show the Fourier transforms of the AFM results, respectively. (A4 and B4) show the section shape of the corrugation along crack propagation direction. (C1) shows the coexistence of ordered stripes and dimples between zones *a* and *b* in Fig. 34. (C2) shows the section shape of the periodic corrugation along the crack propagation direction. (D1) The ordering in concentrated colloidal suspensions of hard sphere subjected to oscillatory shear in a parallel plate geometry. (D2) The oscillating granular materials with two-frequency forcing. (D3) The silicon oil surface under convection. (D4) The honey comb and (D5) the bubble bath, all showing the similar formation mechanism with that of periodic corrugations in BMGs (reproduced from Ref. [257] with permission. ©2009. American Institute of Physics).

observed in some specific compositions or loading conditions. Under tensile loading, most BMGs seldom exhibit ductility after yielding, which is completely different from that of compression of BMGs which could have some plasticity with stable shear banding. The tensile fracture morphology is also slightly different from that observed in compression. In addition to the vein-like patterns, a unique pattern of radiate cores, also appears on the fracture surface, as shown in Fig. 42(a) for a typical Zr-based BMGs. These cores coexists with the vein-like patterns and the veins seems radiate from these cores and propagate toward outside. Zhang et al. [90] suggested that the fracture in the regions of cores takes place in a normal fracture mode, rather than a pure shear mode. From this morphology,

it could be inferred that the fracture of BMGs should first originate from these cores induced by normal tensile stress on the plane, and then catastrophically propagate toward outside of the cores in a shear mode driven by the shear stress. Therefore, the above morphology reflects the difference in the fracture mechanisms of metallic glasses under compressive and tensile loading and indicates that the normal stress plays an important role in the fracture process [90].

Generally, the fracture of BMGs under compression often occurs catastrophically along the shear plane due to the instability of the main shear band. In this process, the elastic energy stored in the sample will be released instantaneously, and results in a significant temperature rise in the dominant shear band, and the formation of the vein-like pattern. In few cases, the shear band along which the sample ruptured does not cover the whole cross section but rather touches the basal plane of the sample during deformation. Once a crack is formed in the dominant shear band, the rupture of the sample will be constrained by the crossheads of the testing machine. Consequently, the fracture of the sample is not catastrophic but occurs in a stable manner, manifesting as the slow release of the stress and elastic energy in small steps in the stress–strain curves. In such a case, a new fracture morphology is observed on the fracture surface, which is totally different from vein-like patterns, as shown in Fig. 42(b). The shape of pattern is similar to that of fishbones with the trunk aligned along the shear direction and the regularly spaced branches aligned nearly perpendicular to the trunk. There are relatively smooth regions with featureless contrast between the fishbone-like patterns, suggesting a relatively planar and straight crack path in these regions. As discussed by Sun et al. [132], the formation of this novel pattern during stable fracture of BMGs is closely related with the low crack propagation speed compared to that of catastrophic failure process, which results in a low temperature rise and

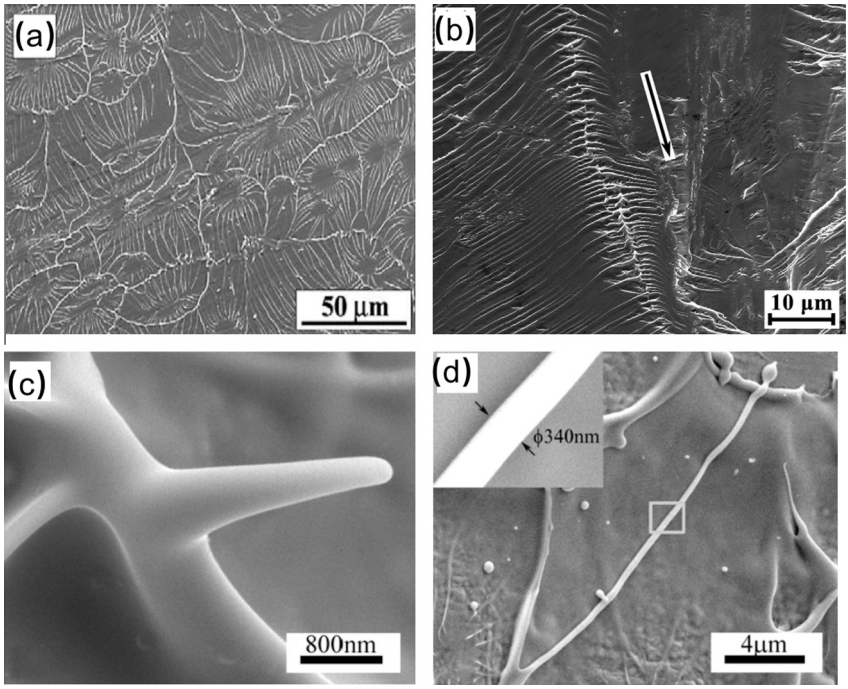

Fig. 42. (a) The radiate cores observed on the fracture surface of a Zr-based BMGs under tensile loading (reproduced from Ref. [90] with permission. ©2003. Elsevier). (b) The fishbone-like patterns observed in stable fracture of a Zr–Co–Al BMG due to crosshead constraint (reproduced from Ref. [132] with permission. ©2012. American Institute of Physics). Fine nanostructures on the fracture surface of a Ce-based BMG including a nanocone in the vicinity of a ridge intersection (c) and an uniform nanowire with a diameter of 340 nm (reproduced from Ref. [261] with permission. ©2011. Cambridge University Press).

thus the failure of meniscus instability during stable fracture. The change of pressure gradient ahead of the crack tip due to geometrical confinement of shear band also have an contribution. The melting features are only found at the edge of fracture plane where the sample ruptured finally and the crack propagation velocity is relatively high.

Other various nanostructures such as nanoridges, nanocones, nanowires and nanospheres can also be spontaneously formed on the fracture surface of BMG at room temperature [261]. The typical features of these nanostructures for a brittle Ce-based are shown in Fig. 42(c) and (d). The nanoscale cone with a symmetrical profile is oriented nearly perpendicular to the crack plane. Such configurations clearly show that on the nanoscale the fracture of BMGs is ductile with the peak-to-peak separation analogous to the ductile fracture of polycrystals. A nanowire with the diameter of 340 nm and a length of about 19.6 mm is found on the fracture surface, implying that viscous flow has readily occurred during its formation [261]. Many nanospheres have also been observed in the fracture surface, and the formation of these nanostructures is closely related with the temperature rise in the plastic zone during fracture [261]. Similar structures such as nanoridges and nanocones can also be observed on the fracture surfaces of various BMGs but at different length scales. A clear correlation between the dimensions of these nanostructures and the size of the plastic zone at the crack tip has also been found, which provide a way to control nanostructure sizes by controlling the plastic zone size intrinsically or extrinsically. The spontaneous formation of the nanoscale structures through fracture of BMGs might also open up a new avenue for fabrication of amorphous metallic nanoscale structures with high strength and high corrosion resistance, which might be applicable and provide building blocks for the development of small devices. The fabrication of these metallic glassy nanostructures may also extend the investigative domain of nanostructure science and technology. For example, a great challenge is assembling and positioning nanoparticles or nanowires in desired locations to construct complex, higher-order functional structures. Controlled positioning of nanoparticles or nanowires has been achieved on pre-defined templates fabricated by top-down approaches. The spontaneous formation of nanoscale metallic glass striped patterns has various applications such as nanoscale gratings or ultra-miniaturized integrated circuits [261]. The nanostructure formation also further confirms that there is nanoscale local softening during the fracture of brittle BMGs.

5.4. Dynamic instability of crack and energy dissipation in BMGs

Once a crack starts to propagate in a brittle solid, its velocity may quickly reach several thousands of mm/s. Consequently, the moving crack results in 3D acoustic wave, crack oscillating and branching, leading to a rough fracture surface, which is not the 2-D surface formed by the crack moving along a planar, straight-line path as predicted by the classical linear fracture mechanics [25]. With the increment of crack speed, the rougher fracture surfaces have to be created to dissipate the released elastic energy. The non-linear plastic behavior in the crack tip also makes the crack instability process complicated. In the fracture of glassy materials, there has long been debating that whether the fracture roughness is caused by the cleavage process or the cavitation due to the plastic flow in the crack tip [262]. For BMGs, the formation of dimple-like structure and nanoscale corrugations suggests that the plastic deformation in the crack tip dominates the cracking process, and these processes are characterized by the peak-to-peak matching on two opposite fracture surfaces [133].

Based on the local plastic softening in the crack tip, the crack instability process and energy dissipation during the fracture of brittle BMGs are discussed in details in Ref. [25]. According to the Irwin-Orowan small-scale zone model, when a crack is blunted, a semicircle-like shape fracture process zone with radius R will be formed in the front of the crack tip as shown in Fig. 43(a). The crack tip open displacement (CTOD), which can be measured from the intersection at a 90° vertex with the crack flanks, is associated with the critical stress intensity factor. The glassy materials in the fracture process zone can be viewed as viscous fluid due to the local temperature rise during crack propagation, which is estimated as high as several hundreds of kelvins, much higher than the T_g [133]. A fluid meniscus shape is formed with the crack advances to the negative pressure direction. There exists a critical wave length λ_{crit}, determined by the negative pressure and surface energy (see Eq. (37)), for the initial perturbation to penetrate into the fracture process zone. Assuming a fluid is flowing in a channel with height H, the dominant wavelength λ can be deduced as [28]:

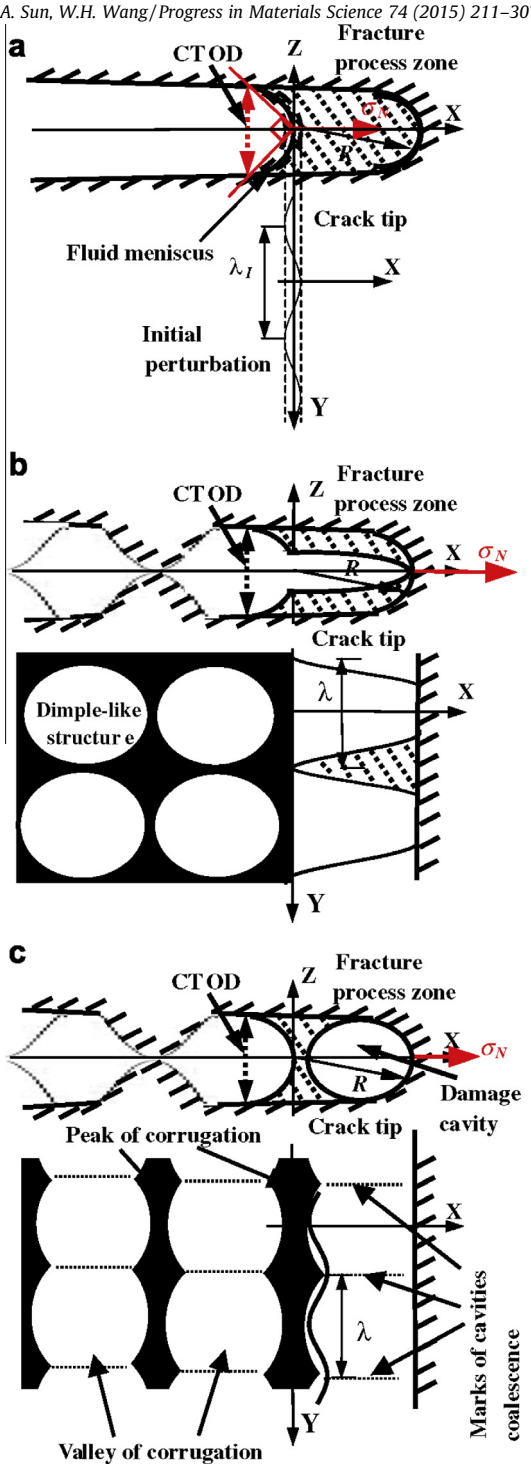

Fig. 43. (a) Sketch of the crack propagation process. Crack propagation direction is *X*-axis and the *X*–*Y* plane is the fracture surface plane. (a) Initial stage of the crack propagation. (b) Formation mechanism of the dimple-like structure. (c) Formation mechanism of the periodic corrugation pattern (reproduced from Ref. [25] with permission. ©2008. Elsevier).

$$\lambda = 2\pi\sqrt{\sqrt{3}\left(\frac{H\chi}{\eta_0}\right)\left[\frac{n}{2(1+2n}\right]^n\left(\frac{\sqrt{3}H}{U_0}\right)^n}, \tag{39}$$

where n is the non-linear exponent of fluid, U_0 is the average integrated flow velocity of the meniscus profile, and η_0 is the viscosity coefficient. Once the initial perturbation is developed, it will penetrate into the crack front with a steady state furrow with the wavelength of λ_S [28]:

$$\lambda_S = 12\pi^2 A(n)\frac{\chi}{\tau_Y}, \tag{40}$$

where τ_Y is the yield shear stress, $A(n)$ is the wavelength coefficient depending on the non-linear exponent n. The height of the channel H is roughly equal to the CTOD as:

$$H = \mathrm{CTOD} = 24\pi^2 B(n)\left(\frac{\chi}{\tau_Y}\right) = \frac{K_C^2}{mE\sigma_Y}, \tag{41}$$

where $B(n)$ is the CTOD coefficient associated with the non-linear exponent n, m is a dimensionless constant depending on material properties and stress states. According to the Taylor's meniscus instability criterion, if the developing wavelength λ is larger than a critical value, $\lambda_S/\sqrt{3}$, the perturbation will develop into a steady furrow with a finger shape, and result in a dimple-like structure. However, if $\lambda < \lambda_S/\sqrt{3}$, the development of perturbation will stop, and the coalescence of the damage cavities will result in the periodic corrugation pattern, as shown in Fig. 43(b) and (c), respectively. The formation of the damage cavities and coalescence are confined to the fracture process zone, and the size of the fracture process zone determines the size of the dimple-like structure and spacing of the periodic corrugation pattern.

Wang et al. [25] studied the fractographic evolution on the fracture surface of a brittle Mg-based BMG generated by different loading modes, i.e. pre-notched three point bending, bending without notch and tension. Under the pre-notched three point bending, a decreased fracture surface toughness is observed with the fractograph evolution sequence: a dimple-like zone, a dimple and corrugation mixture zone, a periodic corrugation pattern zone and a featureless mirror zone. In contrary, the fractograph under tension and bending without notch shows an evolving sequence of the period corrugation pattern, the mixture zone, the dimple-like structure and the hackle zone, which have also been frequently reported by other studies. This suggests that the stress state plays a critical role in the crack instability and energy dissipation process. In addition, the non-linear elastic behavior (hyperelastic stiffening or softening) also has contribution. The fracture energy dissipation mechanism in the dimple-like zone and corrugation pattern zone is dominated by the local plastic flow mechanism as discussed above, whereas in the pure mirror zone, the energy dissipation mechanism is dominated by the quasi-cleavage fracture when the size of the fracture process zone approaches a characteristic length of the local quasi-cleavage zone [135]. These findings are crucial for understanding the fracture mechanism of brittle BMGs.

5.5. Fractal nature of fracture surface in BMGs

The relation between the geometrical structure of fracture surface and quantities describing fracture energetics is of fundamental importance to understand the nature of fracture [263]. Since the pioneering work of Mandelbrot et al. [264], extensive studies have been done to correlate the roughness of fracture surface with the mechanical properties using the fractal geometry analysis. The fracture surface of various materials (metallic alloys, silicate glasses, quasi-crystals, rocks, sea ice and wood, etc.) are found to be self-affine with a roughness exponent $\zeta = 3/4$ [265], indicating a fractal nature of fracture surfaces. The scaling exponent is also weakly dependent on the nature of fracture mechanism of materials and failure modes. Considering the remarkable impressive mechanical properties of BMGs and the diverse patterns on their fracture surfaces, it is interesting to study their fracture morphology with the fractal geometry analysis method and correlate it with their fracture properties.

Bouchaud et al. [266] first investigated the fracture surface of a typical Zr-based BMGs by the height correlation method which is commonly used in the self-affine fractograph analysis. The roughness of fracture surface is estimated along directions parallel (x axis) and perpendicular (z axis) to crack propagation through the computation of the second-order moments $\Delta h(\Delta x)$ and $\Delta h(\Delta z)$ of height difference between points distant of Δx and Δz, respectively. The calculation results show that $\Delta h(\Delta x)$ and $\Delta h(\Delta z)$ exhibit a power-law increase with roughness exponents of $\beta \approx 0.55$ and $\varsigma \approx 0.54$, respectively, which is a multi-affine scaling contrary to the common observation in other materials. They suggests that the mismatch between two facing fracture surfaces as a function of distance indicates that the fracture occurs mostly through the growth and coalescence of damage cavities. The fractal nature of these damage cavities is shown to control the roughness of the fracture surfaces. The similar height-profile analysis is also performed by Jiang et al. [267] on the nanoscale periodic corrugation pattern generated on the dynamic fracture surface of a tough BMG. The valley landscape of the corrugation pattern is shown to exhibit a similar fractal character with a dimension of about 1.48 and Hurst parameter of 0.52.

Recently, Gao et al. [268] performed a systematic fractal geometrical analysis on the dimple structures on the fracture surface of different typical BMGs with significant different toughness ranging from 1.26 to 200 MPa $m^{1/2}$ as shown in Fig. 44. Different from the height-profile analysis, they analyzed the SEM micrographs of the fracture surface using the fractal geometrical method

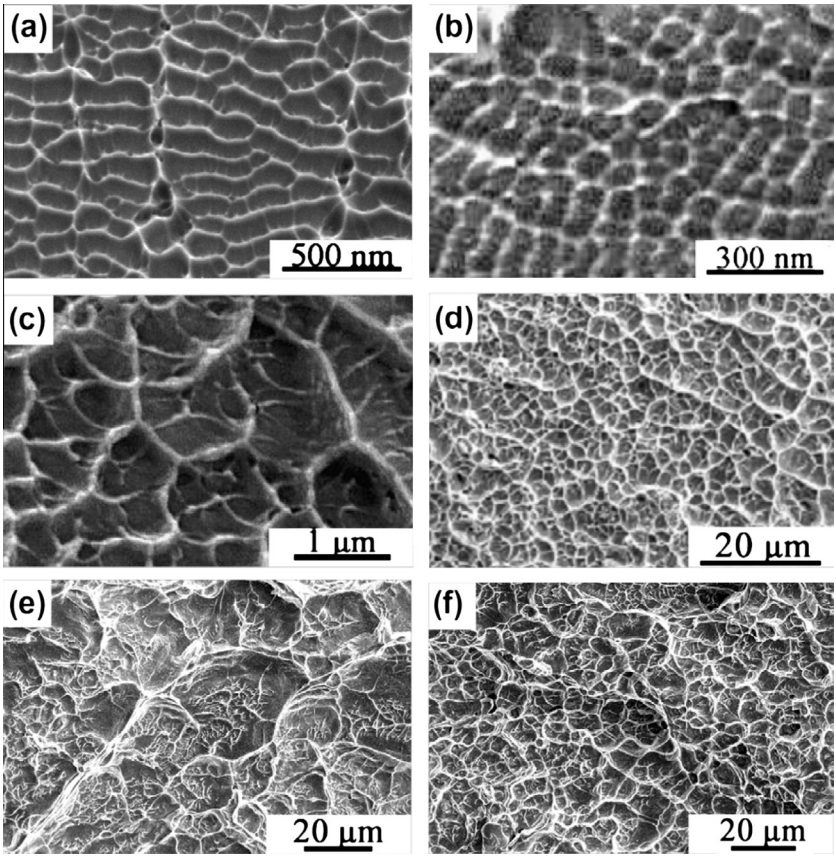

Fig. 44. SEM images of dimple structures on the fracture surface of BMGs at various fracture toughness. (a) $Dy_{40}Y_{16}Al_{24}Co_{20}$; (b) $Mg_{65}Cu_{25}Gd_{10}$; (c) $La_{55}Al_{25}Cu_{10}Ni_5Co_5$; (d) $Ce_{60}Al_{20}Ni_{10}Cu_{10}$; (e) $Zr_{52.5}Cu_{17.9}Ni_{14.6}Al_{10}Ti_5$; (f) $Zr_{57}Nb_5Cu_{15.4}Ni_{12.6}Al_{10}$ (reproduced from Ref. [268] with permission. ©2012. Elsevier).

(the box-counting method). The original gray-scale SEM micrographs are first digitized into the binary black-and-white images by applying the median filter method. These images are divided by the grids of square box with the edge length Δx. For the fractal nature of dimple structures, the number of boxes $N(\Delta x)$ that covering at least one pixel of the wall of dimple structure can be expressed as $N(\Delta x) \sim \Delta x^{-D}$. The D can be viewed as the fractal dimension [see Fig. 45(a)]. Strikingly, the fractal dimensions of the dimple-like structure appearing in different length scales for various BMGs seems to be a constant in a narrow range of 1.6–1.8 [see Fig. 45(b)], indicating a unified fracture mechanism for BMGs with different properties. It is noted that the dimple structure on the fracture surface have 3D topography and the values of D obtained from SEM micrographs are in fact the fractal dimensions of 2D in-plane projection of the dimple network. According to the fractal theory, the real fractal dimension D_R for 3D dimple structure should be $D_R = D + 1$ and the D is related with the above roughness exponent β by $\beta = 3 - D_R = 2 - D$. The fractal nature of dimple structure suggests that the fracture of BMGs is a complex process, which may be far from the equilibrium with a non-linear dynamics. This is different from the common view that the fracture process and characteristics are generally described by the mean-field theoretical models. The appearance of the fractal has been suggested to relate with the interacting entities during the fracture process. As the formation of dimple structures on the fracture surface is closely related with the plastic deformation zone ahead of the crack tips [see Fig. 45(c)], the fractal nature of dimple structure has been correlated with the interaction of flow units, which could cause a spatial distribution of the plastic zone size during the fracture. A stochastic theoretical model for spatial evolution of correlated STZs was proposed [170]. According to the model, the interaction between STZs via the long-range elastic field induce the fluctuating

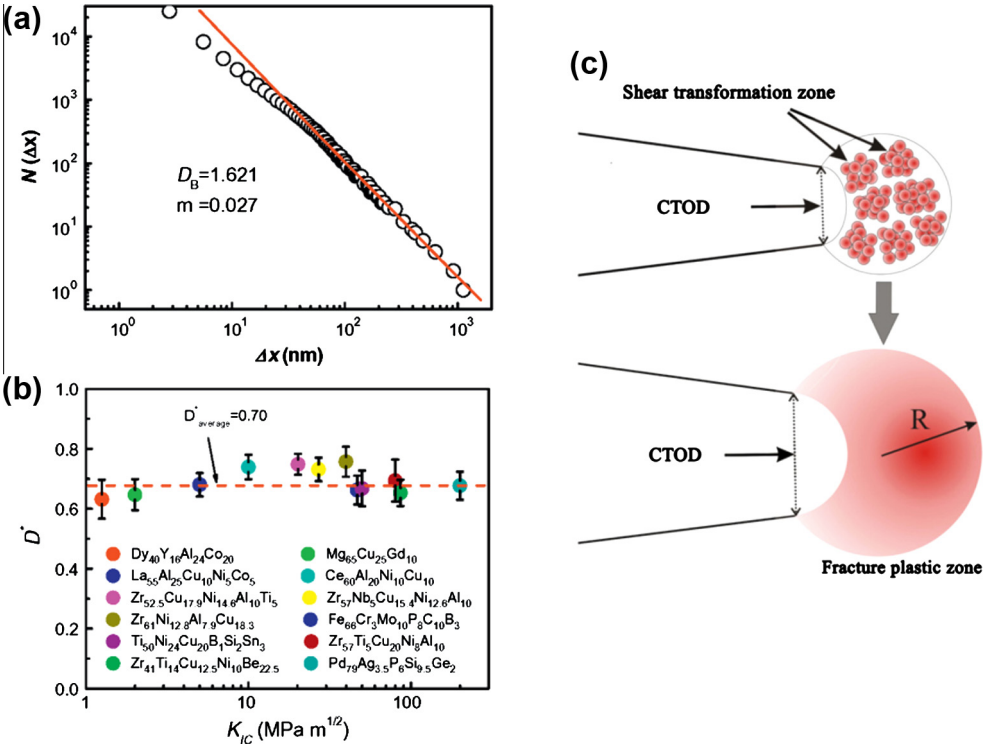

Fig. 45. (a) Log–log plot of the number of box $N(\Delta x)$ versus the size of box Δx of binary black-and-white images of $Dy_{40}Y_{16}Al_{24}Co_{20}$. (b) Fractal dimension increment $D^* = D - 1$ versus K_C of 12 MGs. The red dashed line represents the average D^* value (0.70) for studied MGs. (c) The Sketch of the formation mechanism of plastic zone in front of the crack tip (reproduced from Ref. [268] with permission. ©2012. Elsevier).

internal stress and strain rate. The internal fluctuating strain rate can be assumed as the noise with a stationary Gauss white distribution that is exerted on the steady-state strain rate without considering the interactions. Taking the expression of noise into the mean-field STZ dynamics and solving the stochastic differential dynamic equations, a power-law probability distribution of STZ density is obtained at the lower limit, an indicator of the fracture during plastic deformation and fracture of BMGs. The study clearly implies that the non-linear behavior in the crack tip may be a consequence of the coupling between density fluctuation and deformation field as well as the interaction of STZs, which lead to the complex fracture process of BMGs [170].

5.6. Summary on fracture morphology of BMGs

Fracture morphology of BMGs is closely related to fracture toughness and strength, and important for understanding of fracture mechanism of BMGs. The patterns, such as the vein-or river-like structures and nanoperiodical stripes, are unique in BMGs and are rarely observed in other materials such as crystalline metals and alloys and oxide glasses. The formation of these patterns is related with the unique structure features, deformation mechanism and strain softening in BMGs.

The size scales of the fracture patterns are across several hundreds of micrometers to tens of nanometers. The scale of these pattern is well correlated with the fracture toughness in different BMG systems which could range from the most toughest alloys to ideally brittle oxide glasses. Combining the remarkable and diverse mechanical properties, the fracture of BMGs provides a wealth of resources to investigate some fundamental issues in the fracture such as crack dynamic instability and the fracture surface roughening and branching.

The fracture patterns on the surface have some hidden orders, e.g. the fractal nature of dimple structures and exactly periodical stripes. The hidden orders in the fracture of BMGs cannot be explained by the traditional mean-field theory. Instead, some theoretical methods and concepts from non-equilibrium dynamics [such as the fractals and self-organized criticality (SOC)] have to be used, reflecting the limitation of traditional continuum-mechanics approach in the complex nature of disorder materials. Interestingly, similar non-equilibrium phenomena have also been observed in plastic deformation of BMGs, e.g. the fractal patterns of multiple shear bands and the SOC state for the deformation of ductile BMGs. As the fracture of BMGs often involve the formation of multiple shear bands in the crack tip, the observed hidden orders should be related with the complex nature of plastic flow process of the glasses.

Fig. 46 summarizes the fracture morphology of various BMGs, and their correlation with the fracture toughness and the dominated plastic flow mechanism in the crack tip. A comparison with traditional crystalline materials and oxide glasses is also shown. It is obvious that the unique fracture behavior and morphology of BMGs closely correlate with their plastic deformation and fracture mechanism at different scales. At the atomic scale, all BMGs are capable of plastic flowing by the activation of flow units, and this is totally different from the dislocation-mediated plasticity in crystalline alloys and the case for ideal oxide glasses where the fracture is assumed to proceed by the direct break of atomic bonding without involving the plastic flow process. In contrast to the strain hardening of dislocation motions in crystalline materials, the STZ-mediated plastic flow has a nature of strain softening, which lead to different crack tip behaviors depending on the fracture toughness of BMGs. For tough BMGs such as Pt-, Pd-, Zr-, Ti, and Cu-based, the strain softening often results in inhomogeneous shear bands ahead of the crack tip. The extension and deflection of multiple shear bands form a plastic zone ahead of the crack tip and the crack often proceeds along the path of some shear bands, leaves the vein-like patterns on the fracture surface. The plastic zone formed by shear bands is fundamentally different from the plastic zone in the fracture of crystalline alloys. One major difference is that the plastic flow is highly inhomogeneous in the plastic zone of BMGs with strain localized into shear bands, while the plastic zone for crystalline alloy is homogeneous. In fact, the real volume (the volume occupied by shear bands) that contributes to the plastic flow process ahead of the crack tip of BMGs is very small. In this sense, a large portion of the fracture toughness of ductile BMGs comes from their relatively high strength. That is also a reason for that the fracture toughness of some BMGs is much lower than that of crystalline alloys even they have the same plastic zone size. For brittle BMGs such as Mg-, Fe-, Dy- and Tb-based, a small-scale plastic zone instead of the inhomogeneous shear bands

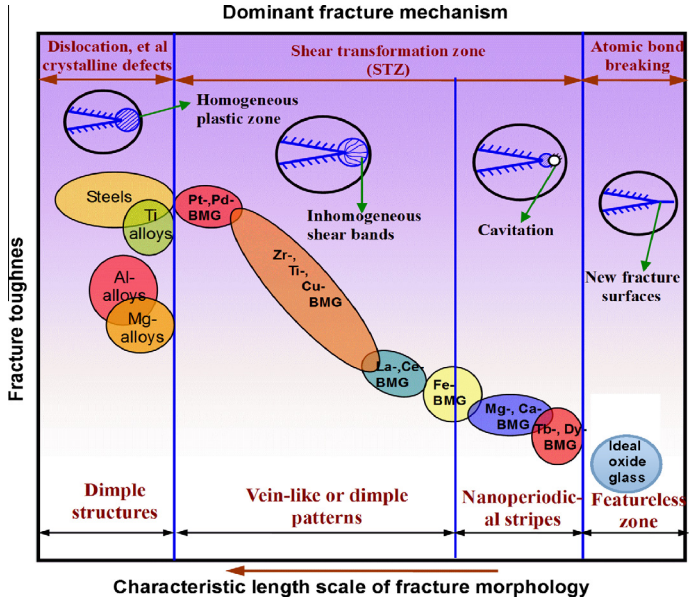

Fig. 46. The schematic diagram for the correlation between the fracture morphology and the fracture toughness in various materials including crystalline alloys, BMGs and oxide glasses. The dominant fracture mechanism both at the atomic scale and the mesoscale for these materials is also shown.

may appear in the crack tip. Due to the significant strain softening, and the materials in the small plastic zone can be viewed as a viscous fluid, and the meniscus instability or the cavitation instability in the plastic zone may dominant the crack propagation behavior. The competition between the two instability processes leads to the formation of either nm-scale dimples or periodical stripes. This is also different from the case of brittle oxide glasses where the crack is propagate by creating new relatively flat surfaces, and featureless smooth zone is often observed on the fracture surface (sometimes some features formed by the crack front wave such as the Waller lines can also be found [25,133]). Studies such as the work of Marsh et al. also suggested that the fracture of brittle oxide glasses also involve a substantial contribution of plastic flow. Here, for the sake of comparison, we only simply refer to those ideal oxide glasses where the fracture proceeds by the breaking of atomic bonding. Therefore, BMGs are intermediate and well bridge the gap between the traditional ductile crystalline alloys and pure brittle materials such as oxide glasses and ceramics. BMGs are able to flow at the crack tip, but their deformation is more complex than that of crystalline alloys and oxide glasses. That is reason why plentiful fracture patterns and far-from equilibrium phenomena are observed in the fracture of BMGs.

Fig. 46 also shows a clear correlation between the fracture morphology and the fracture toughness found among various materials regardless their structures and plastic deformation mechanisms. With the reduction of fracture toughness, the characteristic length scale of the fracture morphology tends to be gradually decreased. This correlation can be well interpreted from continuum fracture mechanics. In general, the fracture toughness of a material is proportional to the energy dissipated during the fracture, which generally includes the plastic energy dissipated in the crack tip and the energy to create new fracture surfaces. The dissipated plastic energy is often proportional to the size of plastic zone in the crack tip corresponding to the characteristic length scale of fracture patterns, and the energy to create new surfaces is proportional to the roughness of fracture patterns. Therefore, it is anticipated that the fracture morphology should have a correlation with the fracture toughness as given by Eq. (38) if one assumes that the characteristic size of fracture patterns are roughly comparable to the size of plastic zone in the crack tip of BMGs.

6. Modeling and simulations on fracture process of BMGs

For BMGs, the crack is often initiated in highly localized regions or shear bands. Once the crack is formed, its propagation speed will quickly reach several thousands of mm/s, and it is difficult to experimentally characterize and resolve the initiation and evolution of crack during fracture. In contrary, the modeling and simulations can provide important information and details on the fracture process and mechanism, especially in the atomic scale process, which is not accessible by the current experimental instruments and methods. In parallel with the experimental studies, there are also many theoretical model and simulation efforts on the fracture process of BMGs [27,29–31,179,250,269,270]. The studies involve in a large different scales from continuous modeling to atomistic simulations, and make up an important portion in understanding the fracture mechanism and macroscopic mechanical behaviors of BMGs and other glassy materials. In this section, a brief review on these modeling and simulation works is presented.

6.1. Coarse-grain continuum modeling

To understand mechanisms of plastic deformation and fracture in glassy materials, many microscopic theories, such as free volume and STZ models, have been developed in past decades. The basic picture of these theories is supported by the molecular dynamic simulations, however, most of these microscopic theories treat spatial correlation effects in the mean-field level, which is difficult to describe the precise spatio-temporal evolution of the inhomogeneous structure in the nucleation and propagation of shear bands and the onset of fracture [29]. In addition, many parameters in these theories depending on the microscopic details have to be determined to make a direct comparison with experiments, resulting in a rather limit power for these models.

To overcome the difficulties of the microscopic approach, Furukawa and Tanaka [29] developed a coarse-grain continuum model for the fracture of glassy materials. In this model, they conceived that the key concept that controls the plastic flow and fracture behavior of glass is the viscoelasticity, which has been verified by experiments. The mesoscopic dynamics of glass can be described by a set of equations for compressible viscoelastic materials. That is, the mass density $\rho(r,t)$ follows the continuity equation:

$$\frac{\partial \rho}{\partial t} = -\Delta(\rho \mathbf{v}), \tag{42}$$

here, $\mathbf{v}(r,t)$ is the velocity field that obeys the generalized Navier–Stokes equation:

$$\rho\left(\frac{\partial}{\partial t} + \mathbf{v}\cdot\nabla\right)\mathbf{v} = -\nabla\cdot\mathbf{\Pi} + \nabla\cdot\boldsymbol{\sigma}, \tag{43}$$

where $\mathbf{\Pi}(r,t)$ and $\boldsymbol{\sigma}(r,t)$ are the pressure tensor and viscoelastic stress tensor, respectively. From the concept of free volume, the general constitutive law that describing the time evolution of structural relaxation for glasses can be written as:

$$\left(\frac{\partial}{\partial t} + \mathbf{v}\cdot\nabla\right)\boldsymbol{\sigma} - \left(\nabla\mathbf{v}^{\dagger}\cdot\boldsymbol{\sigma} + \boldsymbol{\sigma}\cdot\nabla\mathbf{v}\right) = G(\rho)\left(\nabla\mathbf{v}^{\dagger} + \nabla\mathbf{v}\right) - \boldsymbol{\sigma}/\tau(\rho)). \tag{44}$$

The right hand of the equation represents the upper convective time derivative, G and τ are the shear modulus and the relaxation time, respectively, which depend on the density and can be used to describe the spatial heterogeneity of material properties. In most materials, the lower the density or the larger the free volume often indicates the more liquid-like behavior with shorter τ and smaller G.

The shear-induced instability or the onset of fracture can be analyzed by carrying out the linear stability of above dynamic equations on the system subjected to a simple shear (for more details see [29]). An important insight resulting from the analysis is that the fracture may originate from the coupling between density fluctuations and stress fields, i.e., shear-induced enhancement of density fluctuation is self-amplified by dynamic and elastic asymmetry between dense and less-dense regions.

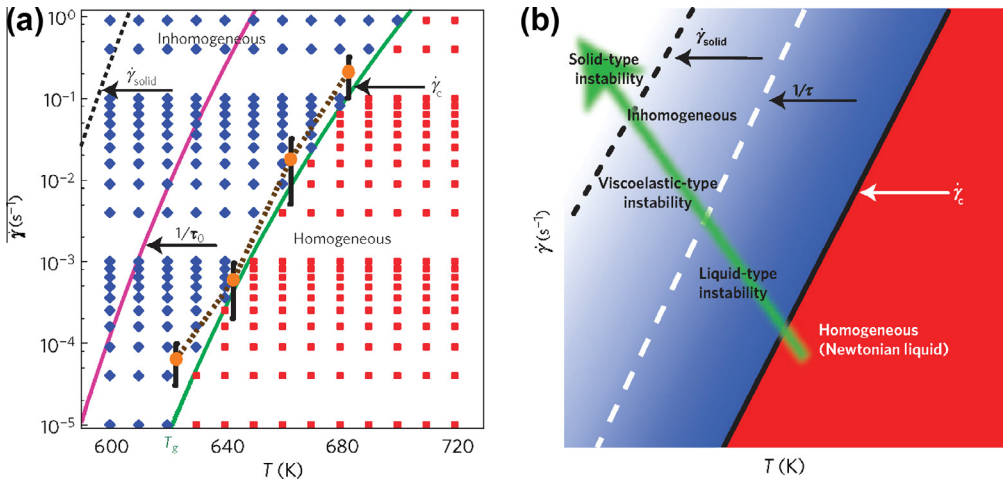

Fig. 47. (a) Dynamic phase diagram of Vitreloy-1 alloy. The red and blue points indicate stable and unstable homogeneous state, respectively. The green and red solid curves represented the predicted critical shear strain rate in the viscous regime and the inverse of relaxation time, respectively. The black dotted curve represents the predicted critical strain rate above which solid-type instability occurs and the orange circles represents the experimentally observed crossover shear rate from Newtonian to non-Newtonian shear thinning behavior. (b) The schematic dynamic phase diagram. (reproduced from [29] with permission. ©2009. Nature Publishing Group).

Three types of mechanical instability have been identified, which dominants the brittle versus ductile fracture behavior of glassy materials at different conditions, as shown in the form of the phase dynamic program of Fig. 47. When characteristic deformation time scale is much longer than the intrinsic structure relaxation time, $t \gg \tau_0$, or equivalently, $\dot{\gamma}\tau_0 \ll 1$, the liquid-type instability dominants, where the effective isothermal compressibility becomes negative. For the onset of this type of instability, the strain rate must be larger than a critical value, which is given by the inverse of the derivative of viscosity η with respect to p, $\dot{\gamma}_c = (\partial\eta/\partial p)_T^{-1}$. In the opposite limit ($t \ll \tau_0$), the structural relaxation is not fully completed, resulting in the solid-type instability where the state become highly heterogeneous when the shear strain is above a critical value, similar to the liquid-type instability. While in the medium time regime $\tau_0[(\partial \ln G/\ln\rho)/(\ln\tau/\ln\rho)] < t < \tau_0$, the unstable mode grows in a different manner from that of solid-like instability, resulting in the viscoelastic-type instability. This type of instability is also of purely dynamic origin and controlled by the strain rate, i.e. $\dot{\gamma} \geqslant (\tau_0/\gamma)^2/\dot{\gamma}_c$. The validity of the three types of instability have also been verified by comparing them with numerical simulation of the model and the existing experimental results of BMGs and glassy polymers. Therefore, the various fracture behavior (brittle fracture versus ductile fracture) that appear in different $T - \dot{\gamma}$ regimes can be interpreted from a unified viewpoint of continuum mechanics. This also provides a criterion to predict and design the fracture behavior of glass from the pressure dependence of viscoelastic properties [28].

Recently, another coarse-grain approach modeling fracture process ahead of the blunted straight crack of a BMG was also developed by Rycroft et al. [212]. The advanced Eulerian level set formulations by coupling the low-temperature STZ theory and the continuum fracture mechanics were used to solve the complex free-boundary problems. The fracture toughness values of metallic glasses were calculated as a function of a increasing degree of structural relaxation (manifested as the initial effective disorder temperature χ_0). According to the STZ theory, the evolution dynamics of the plastic deformation rate D^{pl} and the effective disorder temperature χ are expressed as:

$$\boldsymbol{D}^{pl}(s,T,\chi) = \tau_0^{-1}\Lambda(\chi)C(\bar{s},T)[1 - s_y/\bar{s}]\boldsymbol{s}/\bar{s}, \tag{45}$$

$$\tau_0^{-1}\dot{\chi} = \Gamma(\bar{s},\chi)(\chi_\infty - \chi), \tag{46}$$

where $\boldsymbol{s}$ is the deviator stress tensor and $\bar{s} = \sqrt{s_{ij}s_{ij}/2}$, τ_0 is the characteristic time scale for the STZ flipping, $\Lambda(\chi)$ is the probability to find a structural fluctuation that is susceptible to a STZ, which is a function of the effective disorder temperature $\Lambda(\chi) = \exp(-e_z/k_B\chi)$. $C(\bar{s}, T)$ is the rate for which STZs undergo shear transformation, and the last terms in Eq. (45) represents deformation-induced anisotropy making the expression tensorially consistent. χ_∞ is the steady-state value of χ, $\Gamma(\bar{s}, \chi)$ is the mechanically generated noise that tends to rejuvenate the glass. The explicit forms for $C(\bar{s}, T)$ and $\Gamma(\bar{s}, \chi)$ can be found in Ref. [212].

In the Eulerian formulation, the deformation rate tensor is a sum of elastic and plastic contributions $\boldsymbol{D}^{tot} = \boldsymbol{D}^{el} + \boldsymbol{D}^{pl}$, where $D^{tot} = (1/2)[\nabla \boldsymbol{v} + (\nabla \boldsymbol{v})^T]$, $\boldsymbol{D}^{el} = \partial_t \boldsymbol{\varepsilon} + \boldsymbol{v} \cdot \nabla \boldsymbol{\varepsilon} + \boldsymbol{\varepsilon} \cdot \boldsymbol{\omega} - \boldsymbol{\omega} \cdot \boldsymbol{\varepsilon}$, and $\boldsymbol{\omega} = (1/2)[\nabla \boldsymbol{v} - (\nabla \boldsymbol{v})^T]$. The strain tensor relates to the stress tensor through Hooke's law. The evolution for the velocity field $\boldsymbol{v}(\boldsymbol{r}, t)$ is $\rho_0(\partial_t \boldsymbol{v} + \boldsymbol{v} \cdot \nabla \boldsymbol{v}) = \nabla \cdot \boldsymbol{\sigma}$, where ρ_0 is the mass density and r is the spatial coordinate. For a blunted straight crack (notch) with root radius ρ under the plane-strain conditions, the mode I crack tip velocity field in a polar coordinate system is:

$$v_x(r, \theta, t) = \frac{\dot{K}_I(t)}{4\mu}\sqrt{\frac{r}{2\pi}}\left[(5 - 8\nu)\cos\left(\frac{\theta}{2}\right) - \cos\left(\frac{3\theta}{2}\right)\right], \tag{47a}$$

$$v_y(r, \theta, t) = \frac{\dot{K}_I(t)}{4\mu}\sqrt{\frac{r}{2\pi}}\left[(7 - 8\nu)\sin\left(\frac{\theta}{2}\right) - \sin\left(\frac{3\theta}{2}\right)\right]. \tag{47b}$$

The linear fracture toughness K_{IC} is the critical value of K_I, at which the crack initiates and global failure occurs. The crack formation is assumed to relate with the void nucleation near the crack tip for which the hydrostatic tension $(1/3)tr\boldsymbol{\sigma}$ exceeds a threshold, σ_c. For the nonhardening materials, $\sigma_c \cong 2s_y\{1 + \log[2E/(3\sqrt{3}s_y)]\}/\sqrt{3}$, where E is the Young's modulus and $s_y/E \ll 1$. Based on above equations, the linear fracture toughness of Vitreloy 1 was calculated for different initial values of χ and χ_0, which reflects the different degree of structural relaxation of the glass. The higher χ_0 the easier the glass is to flow. There numerical calculation results show that the spatial distribution of χ and the notch geometry are markedly different for the higher χ_0 (660 K) and the lower χ_0 (600 K). For the higher χ_0 case, χ is rather smoothly distributed in the near tip region and the notch undergoes continuous blunting with its radius of curvature growing continuously and uniformly with K_I. While the lower χ_0 case is qualitatively different. At small loads, there is little plastic deformation and the increase of K_I, and plastic deformation localizes in the root vicinity, resulting in sharply and inhomogeneously distributed χ. Meanwhile, the radius of the curvature of the notch varies spatially with a pronounced reduction near the root. The different distribution of χ results in totally different elasto-plastic crack tip instability as shown in Fig. 48, where the minimum pressure $p_{\min}$ versus K_I is shown for two values of χ_0. The lower χ_0 sample exhibits less plastic deformation and consequently less stress relaxation, resulting the more negative $p_{\min}$. As K_I increases, $p_{\min}$ drops abruptly for lower χ_0, while the curve for the higher one varies smoothly and moderately. The fracture toughness K_{IC} for which the $p_{\min}$ touch the threshold for the void nucleation, is determined to be 30 MPa $M^{1/2}$ for χ_0 = 600 K and 80 MPa $m^{1/2}$ for χ_0 = 660 K, respectively. This clearly suggests a annealing-induced embrittlement transition similar with that in experimental observations. The typical values of K_{IC} seems to be in a right ballpark, without fine-tuning the model parameters. The model could also be used to study the role of other parameters (e.g. the Poisson's ratio) on the toughness and crack tip instability if one assumes a dependence of these parameters on χ.

6.2. Finite element methods

The above theoretical continuum models could give some universal features of fracture mechanism, while analytically solution under complex loading conditions or boundary problems is difficult, and these model cannot give details on the evolution of stress fields in the crack tip during the fracture process either. The finite element (FE) simulations is a powerful tool to solve this kind of complex boundary problem and have been widely used in various engineering fields [271]. Tandaiya et al. [30,31,269] have systematically studied fracture process under different loading modes and factors that control the crack tip plasticity and toughness in BMGs with the FE simulations. They used the

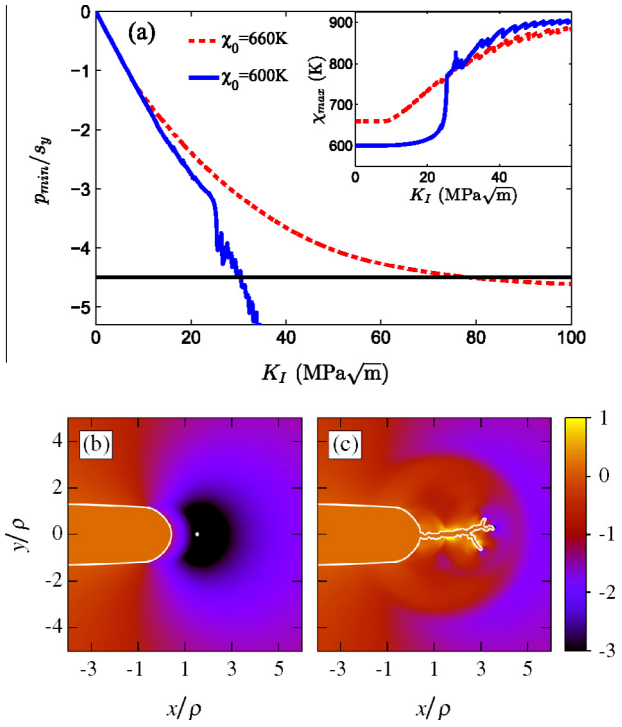

Fig. 48. The calculation results for the fracture for a blunted straight crack of two glasses with different degree of structural ordering, i.e. χ_0. (a) The p_{min}/s_y versus K_I for χ_0 = 600 K (solid blue line) and χ_0 = 660 K (dashed red line). The horizontal line is the threshold for void nucleation. (Inset) P_{max} versus K_I. (b) A snapshot of the system ($p = s_y$ is plotted) when a void nucleates. (c) The subsequent catastrophic failure (reproduced from Ref. [212] with permission. ©2012. American Physics Society).

plane strain, small-scale yielding (SSY) condition, and a elastic-viscoplastic theory proposed by Anand and Su (AS) [272] for the deformation of glasses. Compared to previous constitutive models, AS model incorporates the Mohr–Coulomb yield criterion, a variable dilatancy parameter and dilatation induced softening, and thus can accurately represent overall features such as load versus displacement response, as well as details of shear band formation during the deformation of BMGs in a variety of situation such as indentation and strip bending. In the AS model, the plastic flow is assumed to occur by shearing accompanied by dilation relative to some slip systems. There are three materials parameters, μ, b and c_0, used to govern the frictional response, the pressure sensitivity of yielding and softening, and the materials cohesion strength, respectively. For the FE modeling, a 2D plane strain boundary layer formulation is used, and a large circular domain containing a notch along its radii is considered. The radius of the outer boundary (R_0) is chosen to be several hundreds or thousands times larger than the initial notch root diameter b_0, so that the plastic zone is well contained within the boundary. To accurately capture the strain gradients and notch blunting, the mesh in the analysis is refined near the notch tip with 16 elements placed along the semi-circumference of the notch, and traction-free conditions are assumed on the notch surface.

The influence of internal friction and strain softening on the plastic zone, stress and deformation field and notch opening profiles can be systematically investigated by choosing different sets of values of μ, b and a uniform value of cohesion c_0 for the entire domain. Under mode I loading [30], the FE simulation results show that a higher value of the internal friction parameter μ leads to a larger plastic zone. For example, when μ is increased from 0 to 0.15, the size of the plastic zone ahead of the notch tip doubles. The plastic zone boundary also shows serrated features and the notch tip opening displacement is enhanced. In addition, a higher μ leads to a severe decrease in opening stress ahead of

the notch tip and a reduction in hydrostatic stress at all angles around the notch tip. On the other hand, it also results in a strong increase in the plastic strain accumulation ahead of the notch tip. These observations, in good agreement with the correlation between the plastic zone size and the toughness established earlier in BMGs, suggests that the enhanced internal friction could lead to improve fracture toughness in amorphous solids. The softening that reflects from the value of b is found to result in the reduction of the levels of all stress component, but enhance the plastic strains around the notch and the notch opening profile. While under mixed mode (I and II) loading [31], the situation becomes different, which is closely related with the mode mixities. In this case, the notch deforms into such a shape that one part of its surface sharpens while the other part blunts. The increase of mode II component is found to dramatically enhances the normalized plastic zone size, lowers the stresses, but significantly elevates the plastic strain levels near the notch tip. As μ is increased, the peak tangential stress is reduced and the plastic strain and stretching are enhanced near the blunting part of the notch.

To gain insight into the near-tip processes such as shear banding and crack branching, a statistical distribution of cohesion strength c_0 can be chosen so that the plastic slip line field and possible brittle crack trajectories around the notch root can be generated. Fig. 49 shows the shear band patterns near the notch tip in FE simulations as well as those observed in the experiments for the pure mode II and mixed mode loading case [31]. Fig. 49(a) and (c) are simulated contour plots for the maximum

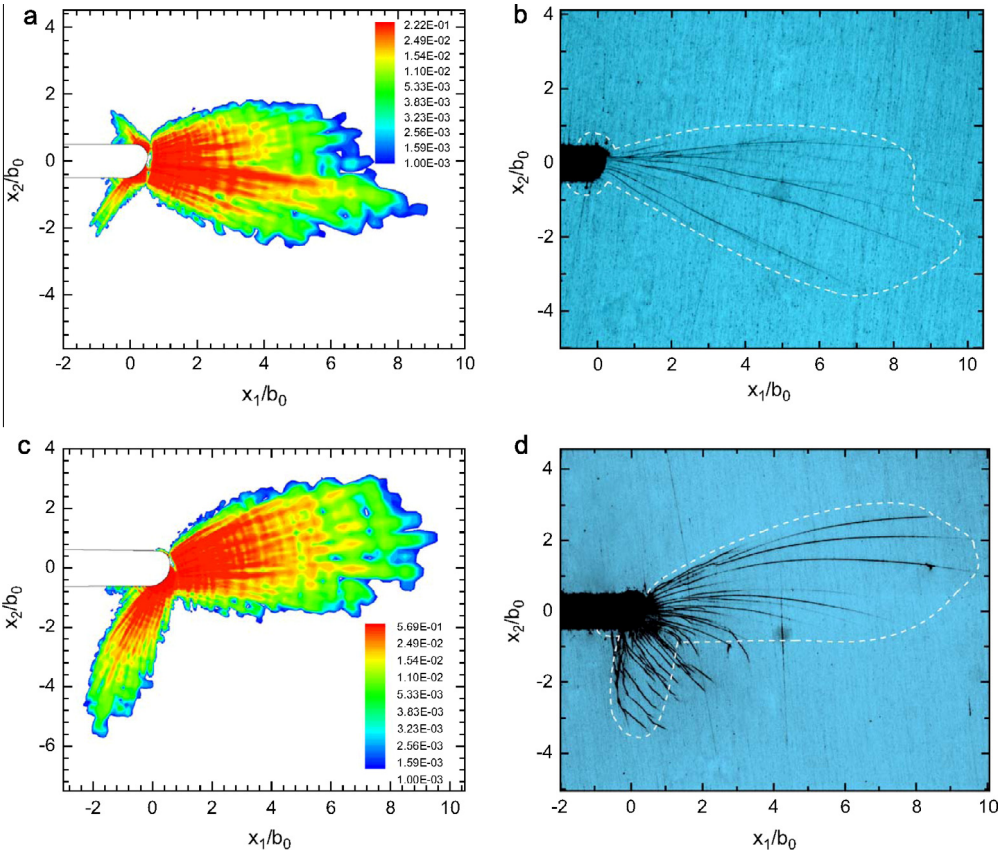

Fig. 49. Comparison of shear band patterns near the notch tip obtained from FE simulations and experiments. (a and c) are contour plots of $\ln(\lambda_1^p)$ for $\mu = 0.05$ corresponding to $M_e = 0$ and $M_e = 0.45$, respectively. (b and d) are the optical micrographs of the near-tip region of specimen with the same M_e (reproduced from Ref. [31] with permission. ©2009. Elsevier).

principle logarithmic plastic strain $\ln \lambda_1^p$, where the full field view of shear band near the notch are shown for the mode mixity $M_e = 0$ and 0.45, respectively. Here, the elastic–plastic boundary is defined as the lowest contour of $\ln \lambda_1^p = 0.001$. Fig. 49(b) and (d) displays the micrographs of the shear bands near the notch region of specimens with the same level of M_e as (a) and (c), respectively. The boundaries of shear bands are indicated by the dashed line. It can be seen that the shear bands predicted from the FE simulations emanate from the notch, forming the plastic zone with serrations in the elastic–plastic boundary. The features are similar to those observed from the corresponding optical micrographs. For case $M_e = 0$, a dominant shear band occurs at about $\theta = -10^\circ$ from the notch line and extends to a long distance from the notch tip. The most striking feature in this case is that the shear bands are straight, and few shear bands can be seen in the lower lobe of the plastic zone for pure mode II loading. In contrast, more shear bands are developed in the lower lobe with the increase of M_e, as shown Fig. 49(c) corresponding to $M_e = 0.45$. The lower lobe of the plastic zone is smaller than the front lobe and profuse shear banding occurs near the blunted lower part of the notch. All the above features from the FE simulations are in good agreement with what is observed from the corresponding experimental optical micrographs. For $M_e = 0.45$ case, however the shear band in the lower lobe in the optical micrograph curve more toward the front of the notch than that predicted from simulations. It should be noted that the overall envelope of shear band region around the notch tip in the optical micrographs is well captured by the FE simulations for both loading cases. All these results clearly suggests that the effectiveness of FE methods in studying the fracture process and in understanding the fracture mechanism of BMGs.

6.3. Atomistic simulations

We have noted that the detailed atomic evolution process during the fracture of BMGs is still poorly understood due to experimental difficulties in capturing the highly temporally and spatially localized shear banding and crack process. Since a closer examination of the fracture mechanisms at even smaller length scale requires higher resolutions than what can be achieved in current experiments, it is necessary to conduct atomistic simulations to gain further insights into the fracture mechanism of metallic glasses [27]. Recently, several works [179] on the atomistic simulation of fracture behavior and on the atomic mechanism of crack initiation in the fracture process of metallic glasses have been done. Murali et al. [27] studied the fracture behavior of typical brittle $Fe_{80}P_{20}$ and ductile $Cu_{50}Zr_{50}$ metallic glasses by the molecular dynamic simulation. Atomic interactions were modeled by embedded atom method potentials with parameters given by Mendelev et al. [273]. The simulation was conducted using the LAMMPS, a well tested and widely used open source code. Glass samples consisting of about 10^7 atoms with final dimensions of $400\,\text{nm} \times 270\,\text{nm} \times 2\,\text{nm}$ were prepared from a melting-and-quenching simulation of a randomly substituted solid solution in the fcc lattice, and were loaded in tension after introducing a sharp crack of length of 68 nm. During the simulation, only the top and bottom layers were subjected to controlled motion while the remaining atoms were allowed to react according to the local forces to avoid the stress waves. The temperature was maintained at 1 K to eliminate the thermal effects. The deformation was performed at the plastic-strain condition by applying the periodic boundary condition in the direction parallel to the crack front and holding the box dimension in this direction constant. Fig. 50 depicts how the crack advances in the tip region for the two glasses at different loading stages. The FeP glass is fails by the propagation of an atomically shaped crack tip, indicating its brittle fracture behavior. In contrast, the CuZr glass exhibits a blunted crack tip through extensive shear banding, suggesting a ductile fracture mode. A close inspection of the crack tip in the FeP glass reveals that the crack grows by a series of nanoscale void nucleation and coalescence events. The simulation results are reminiscent of experimental observations and provide further evidence that nanoscale periodic corrugations seen in brittle MGs are formed by the cavitation process. Further stress analysis shows that the key factor responsible for the two distinct types of fracture behavior observed in the two glasses is the atomic scale spatial fluctuations in local properties (e.g., density). The density fluctuation in the FeP glass are higher than those in the CuZr glass which can induce even larger fluctuations and voids which preferentially nucleate in the regions of low atomic density. The density fluctuation can induce even larger fluctuations in other local

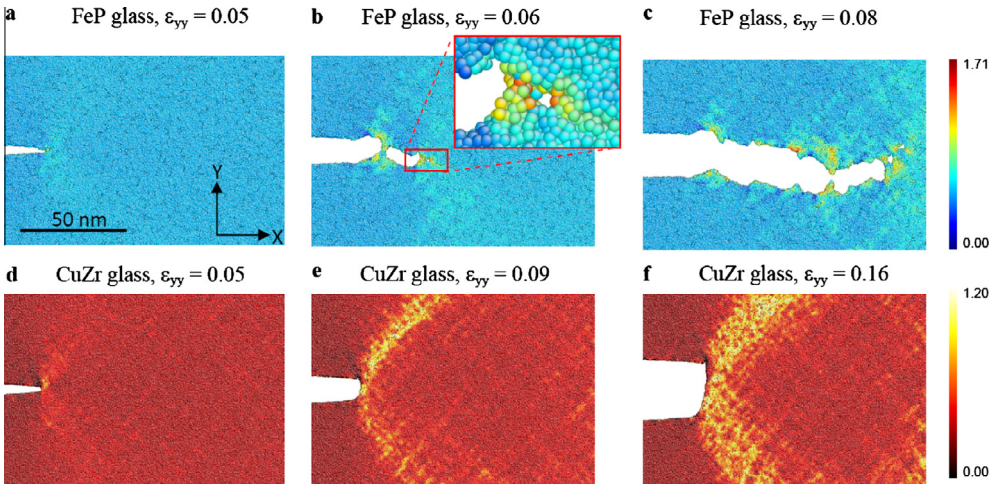

Fig. 50. Close-up views of crack-tip regions obtained by atomic simulations in FeP glass (a–c) and CuZr glass (d–f) at various applied strains ε_{yy} where $\varepsilon_{yy} = \delta h/h$ with h the sample height. The color indicates the local von Mises strain (reproduced from Ref. [27] with permission. ©2011. American Physics Society).

properties such as the local cavitation stress of the material. Indeed, from the hydrostatic dilation simulations, it is observed that the cavitation process in the brittle FeP glass undergoes a relatively large fluctuation of 40% in small samples, while the fluctuation in the cavitation stress in the CuZr glass is less than 10%. The study provides important insights into the root cause of ductile versus brittle behavior in BMGs.

Guan et al. [179] recently studied the mechanism of cavitation during fracture of a $Zr_{50}Cu_{50}$ metallic glass. They considered the expected nucleation rate of cavities in an amorphous solid and compared the simulation results with theoretical predictions. From the classical nucleation theory, energy fluctuation needed to nucleate a cavity must be sufficient to generate the new surfaces, and arrange the material to accommodate the cavity. The free energy barrier for the cavitation is

$$\Delta F_c = \frac{4}{3}\pi r_c^3 K(\varepsilon - \varepsilon_c) - 4\pi\gamma r_c^2, \tag{48}$$

where K is the bulk modulus, γ is the surface energy of the flat surface, r_c is the critical radius where the cavity become unstable, ε_c is the equivalent volume strain corresponding to the unstable cavity. The r_c is closely related with a parameter known as Tolman length δ [274]:

$$r_c = r^*\left(\frac{1}{2} + \frac{1}{2}\sqrt{1 + \frac{4\delta}{r^*}} - \frac{2\delta}{r^*}\right). \tag{49}$$

If the energy barrier is larger than the thermal energy scale k_BT, the rate of cavitation can be expressed as, $R_\varepsilon = \nu \exp(-\Delta F_c(\varepsilon)/k_BT)$, where ν is the attempted frequency. The fraction of the cavitated samples $f_\varepsilon^T(t)$ was calculated as a function of time for each strain at temperature T. If the cavitation process is a Poisson process, the fraction can be expressed as $f_\varepsilon^T(t) = 1 - \exp(-R_\varepsilon^T t)$ with a single constant cavitation rate R_ε^T. Fig. 51 shows typical plot $\ln(1 - f_\varepsilon^T(t))$ as a function of t for strain over the entire time window. For short time scale ($t < \tau_e$), the relation can be well fitted by the Poisson process, where the free energy barrier can be extracted from the data of samples. These calculations leave only one single fitting parameter, and the Tolman length δ was determined. The best fit for the data of glasses gives $\delta = 1.15 \pm 0.01$ Å. This suggests that the cavitation is controlled by the spatial heterogeneity in metallic glass with preferential nucleation sites. Within the framework of classical nucleation theory, the local fluctuation that control the cavity was investigated by varying the

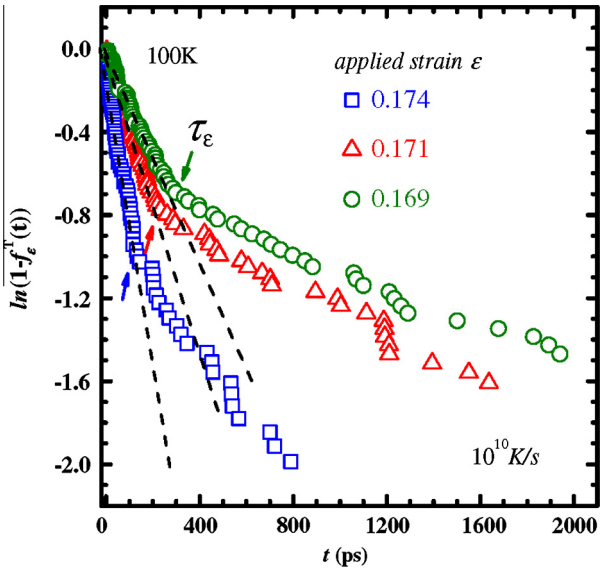

Fig. 51. The values of $\ln(1-f_{\varepsilon}^{T}(t))$ as a function of t for several applied strain of a simulated glassy sample. f_{ε}^{T} is the fraction of samples that have cavitated. The times that deviate from the Poisson behavior, τ_e, are denoted by arrows (reproduced from Ref. [179] with permission. ©2013. American Physics Society).

parameters such as the Tolman length, δ, and the critical strain, ε_c, in simulations. The analysis shows that the cavitation sites are characterized by the low local surface energy (high δ) and high structural susceptibility to plastic deformation (lower ε_c). On the longer time scales ($t > \tau_e$), strain aging or structure relaxation may take into effect, and results in the systematic decrease of cavitation rate as shown in Fig. 50. These insights extracted from the simulations strongly indicate that nanoscale cavitation must be considered as one factor, and perhaps the primary factor, which contributes to the experimental observed quasi-brittle behavior during fracture of many BMGs [8].

An et al. [275] also studied the cavitation process in a binary metallic liquid $Cu_{46}Zr_{54}$ during hydrostatic expansion by MD simulations using a quantum mechanics (QM)-derived potential. Different from the process in glass, they show that cavitation can be described as a random Poisson process. Using the activation volume obtained from the transition-state theory and the surface energy from the Tolman length model, they find that the cavitation rate is in accord with MD simulations. Extrapolation of the pressure dependence of the activation volume from MD simulations of low tensile pressure also agrees well with the macroscale cavitation experiments performed in Vitreloy 1 metallic liquid. Due to the significant softening, a shear band formed ahead of the crack tip during the fracture process of BMG can be viewed as a viscous liquid layer. The results about the cavitation in glass-forming liquids may be helpful for understanding cavitation instability in shear bands ahead of the crack tip during fracture of BMGs.

6.4. Mimic experiments and modeling

In the inhomogeneous flow regime, once a shear band is formed, its viscosity is significantly reduced due to the shear-induced disordering. The subsequent deformation and fracture process in BMGs can be viewed as the separation of a thin viscous layer between two elastic solids. This was first recognized by Pampillo et al. [276]. They conducted a set of model experiments with grease between glass slides and refer the Taylor instability as the cause of the fingers or veins which develop on the fracture surface. Spaepen et al. [277] analyzed the wavelength between the tributaries to establish a relationship between the fracture stress of metallic glass and the spacing between veins utilizing

the Taylor instability. The instability, where a viscous fluid becomes unstable and develops finger-like features, has been observed in metallic glasses and other systems. This provides an interesting opportunity to conduct model experiments of separation of grease between two plates to understand the fracture process of BMGs. Compared to the case of real fracture experiments on BMGs, many parameters that control the fracture process can be easily tuned in the mimic experiments, thus providing a convenient way to understand the Taylor instability in such systems. Deibler et al. [250] performed a series of model experiments in which a thin grease layer is tested in tension to mimic the vein-like fracture surface features in BMGs. In their experiments, layer thickness, substrate shape, viscosity of grease layer, and stress state are varied, and feature size of the vein patterns are examined. These correspond to the effects of sample geometry, shear band viscosity and stress state on the fracture behavior of BMGs. The typical fracture surface appearances that formed in these mimic experiments for different substrate shapes and aspect ratios are shown in Fig. 52. The results are reminiscent of the vein-like patterns formed on the fracture surface of BMGs. One can see that large river-like veins are favored for substrates with larger aspect ratios (2:1 and 10:1), while smaller, more equiaxial fracture surface features are formed for substrates with a 1:1 aspect ratio. In addition, the thickness and viscosity of the grease layer also have an influence on the feature surface sizes, where the spacing of vein patterns decreases with the decreasing thickness or increasing viscosity of the layer. These results are generally consistent with what is observed in the fracture of metallic glasses [278].

Mesoscopic models [151,279–281] have also been developed to mimic the fracture process of disordered and amorphous materials. Among them, the most commonly used is the random fuse model (RFM) [279], which is often used to study the brittle fracture behavior of materials. The RFM with a network of fuses subjected to an external voltage represents a scalar electric lattice analogy of the elasticity problem in brittle fracture where the local stress (σ_i), strain (ε_i), and local elastic modulus (E) are mapped to the current (I), the potential drop (V_i) and local conductance (g_i), respectively [270]. Each individual fuse i behaves Ohmically, $I_i = g_i V_i$, up to a local threshold current T_i, similar to the elastic behavior of brittle fracture. The local threshold T_i can be a uniformly distributed quenched random variable, corresponding to the heterogeneous local properties in amorphous materials. The model can well resolve the fracture behavior of brittle materials which fail in the elastic regime. However, the fracture of BMGs (even for brittle ones) are often involves local plastic deformation in the crack tip, which is often manifested as highly heterogeneous shear bands, which cannot be captured by the linear RFM. Recently, Picallo et al. [270] developed a ductile random fuse model

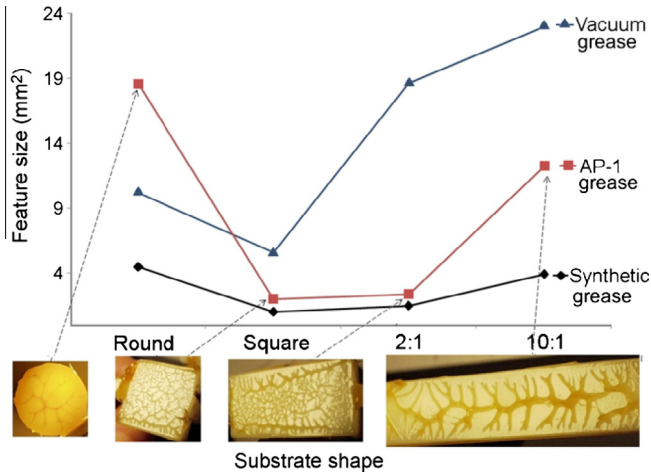

Fig. 52. The effect of substrate shape and aspect ratio on feature size and morphology of the fracture surface in the tension test of grease layer between two substrates (reproduced from Ref. [250] with permission. ©2010. Elsevier).

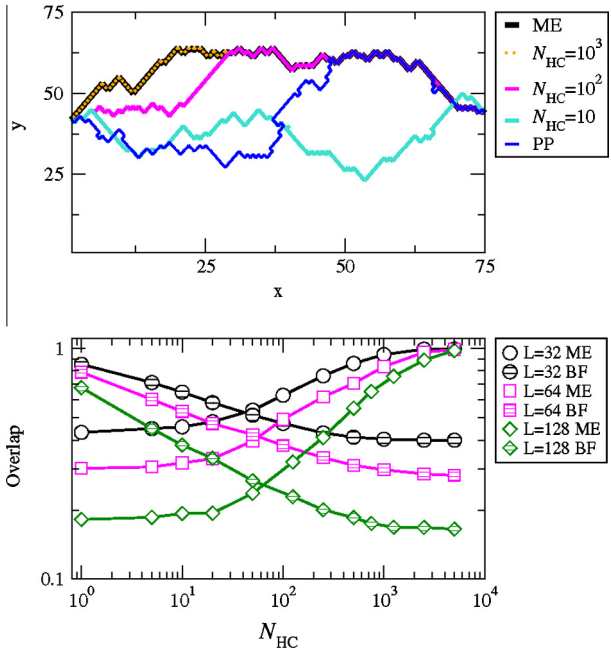

Fig. 53. Top: The fracture surfaces obtained from ME, PP and DRFM for the same disorder realization in a $L = 75$ system. Bottom: Average over 103 disorder realization of the total spatial overlap of the DRFM final crack with both the corresponding ME and BF ($N_{HC} = 0$) surface for $\beta = 0.1$ (reproduced from Ref. [270] with permission. ©2010. American Physics Society).

(DRFM) to incorporate the ductile fracture behavior of amorphous materials. To accommodate permanent deformation, they define a "healing cycle" of an individual element by imposing an voltage source (i.e., an electric battery) in series with the fuse to generate an opposite current through it, so that the elastic deformation is relaxed below the threshold while plastic deformation accumulates in the element. By varying the material properties, the model can exhibit fracture behavior ranging from brittle to ductile. Fig. 53(a) shows the fracture paths obtained from a typical disordered configuration in DRFM simulations. Here, N_{HC} is the numbers of healing circles experienced by a fuse element before its break, and therefore can be used to quantify the capability of the system to sustain local plastic deformation. For comparison, the fracture surface paths generated by the minimum energy (ME) surface [280,281] and the perfectly plastic path [280] for the same disordered configuration are also plotted. Apparently, with the increase of N_{HC} or ductility, the fracture surface path generated from DRFM gradually approaches the ME path; while the fracture surface largely overlaps with the purely brittle fracture surface ($N_{HC} = 0$) for systems with low values of N_{HC} [see Fig. 52(b)]. This is in agreement with the results reported in more complex models. For the ductile system, the yielding process takes place in the form of avalanches of strain events that are found to be power-law distributed with an exponent of $\tau \sim 1.5$, this is comparable with the experiments analysis of the serrated flow of BMGs ($\tau \sim 1.4$–1.6 [112]) and theoretical predictions of ($\tau = 3/2$ [282]).

7. Summary and outlook

Understanding and characterizing the complexity of material fracture is of great interest and importance in condensed matter physics, material science and engineering applications. As a new class of advanced materials, bulk metallic glasses are promising in wide applications due to their unique amorphous structure and remarkable and diverse mechanical, physical and chemical properties. The fracture behavior and the underlying fracture mechanism of BMGs are now receiving more

and more attention, and understanding the fracture of BMGs will provide useful guidelines for designing and controlling their mechanical properties in engineering applications. In this article, we briefly reviewed various aspects of the fracture of BMGs, including fracture behaviors and phenomena, fracture modes, the fracture criterion, the fracture toughness, and fracture surface morphology. Accumulated experimental data on fracture properties has been presented and its connections with theoretical developments have been provided. Depending on their composition and external loading conditions, BMGs display diverse fracture properties such as various fracture modes, a wide range of fracture toughness, and unique fracture surface morphology and fracture path. These remarkably different fracture properties, together with the unified plastic deformation mechanism at the crack tip (shear banding or plastic softening), render them model systems to study some critical and fundamental issues in the fracture physics of glassy materials such as crack initiation, crack instability, branching, and energy dissipation during the fracture process. In addition, the role of various intrinsic (structure, internal states and elastic constants, etc.) and extrinsic (temperature, stress and loading rate, etc.) factors in the fracture process of BMGs and possible mechanisms for these correlations have been discussed. Theoretical modeling and simulations of the fracture process ranging from continuum to atomic scale have also been introduced.

The fracture behaviors and features of BMGs are briefly summarized as follows:

(1) The BMGs have diverse fracture modes ranging from purely brittle to compressive plasticity, and even to superplasticity when the BMG has high flow defects or approaches its glass transition temperature; The fracture mode of BMGs depends not only on their composition, but also on various extrinsic factors such as the sample size, the loading rate, and testing conditions.
(2) The BMGs display multifarious fracture features such as various fracture modes, fracture paths, obvious deviation from the maximum shear stress plane, and a tension–compression strength asymmetry, which are completely different from traditional crystalline alloys.
(3) Due to the absence of strain hardening ability, the fracture strength of BMGs is roughly equal to their yield strength which is much higher than that of their crystalline counterparts. The fracture strength of BMGs correlates well with the Young's modulus due to their almost constant elastic limit ($\sim$2%). The fracture strength has a weak dependence on the loading rate, but could be affected by the pressure or normal stress.
(4) The fracture of BMGs cannot be fully described by a specific failure criterion such as the maximum normal stress criterion, the Tresca criterion, the von Mises criterion or the Mohr–Coulomb criterion. A unified fracture criterion such as the ellipse criterion can describe multifarious fracture features. The criterion strongly suggests that the pressure or the normal stress plays an important role in the plastic flow and fracture of BMGs.
(5) The fracture toughness of BMGs varies significantly from the almost ideally brittle Mg-based BMGs, approaching that of purely brittle oxide glasses, to the extremely tough Pd-based BMG with the highest known damage tolerance.
(6) Most BMGs, including the ideally brittle metallic glasses, proceed through a unified local softening mechanism at the crack front tip, but at different length scales. Depending on the toughness, this local softening can induce either shear bands or nanoscale plastic zone in front of the crack tip. The deflection and branching of shear bands can form a plastic zones in the crack front tip. In spite of the inhomogeneous nature, the size of the plastic zone formed by shear bands has a clear correlation with yield strength and toughness, which can be described by continuum fracture mechanics.
(7) The fracture of BMGs has plentiful fracture surface morphology including a vein-like dimple pattern, nanoperiodical corrugation, a mixture of dimpled and nano-striped pattern, and unique nanoscale structures, etc. due to the local softening nature of the fracture mechanism. The fracture surface morphology is closely associated with the fracture toughness and the microstructural characteristics of metallic glasses, and can reflect the glassy nature and fracture energy dissipation mechanism.
(8) The fracture behavior of BMGs is very sensitive to intrinsic and extrinsic factors such as composition, strain rate, fracture mode, the crack propagation speed, and measuring environments.

(9) The factors determining intrinsic fracture or brittleness have no simple link with interatomic potentials, yet there is a correlation between the ratio of the elastic shear modulus G to the bulk modulus K and fracture toughness or plasticity: a high ratio of G/K favors brittleness and vice versa. The correlation provides useful guidance for the design of tough BMGs.
(10) The BMGs with remarkable diverse fracture properties, together with the unified plastic deformation mechanism at the crack tip, are model systems to study some critical issues in fracture physics such as crack initiation, crack instability and branching and energy dissipation during the propagation process of crack.

We note that despite the extensive works above, studies on the fracture of BMGs are generally at a preliminary stage compared to their extensively studied elastic and plastic deformation properties, glass-forming ability, structure characteristics and relaxations. Many studies are still on a qualitative level and the desired comprehensive and quantitative understanding of the fracture process of BMGs is yet missing. This can be attributed to the complex nature of fracture mechanics compared to elastic and plastic mechanics, and the lack of good-quality BMG specimens in sufficiently large sizes and quantities. We now would like to raise some open and critical issues in this field. These topics and issues are only a few from a vast list of potentially intriguing directions but are believed to represent current research importance and interests.

- *The atomic basis for fracture criterion in BMGs:* The classical fracture criteria such as the Tresca and Von Mises criterion that are commonly used in crystalline materials fail to describe the fracture behavior of BMGs. The newly proposed ellipse criterion seems to be a good candidate to account for the fracture of various BMGs in a unified manner. However, the atomic basis for the phonological criterion, the physical meaning of the parameters in the ellipse criterion, and how parameters correlate with the atomic structure (such as SRO or MRO) and bonding nature of BMGs are still challenges for the future.
- *Crack initiation process:* Experimental and simulation studies have shown that the crack is preferentially initiated in a shear band by the cavitation process, however, the detailed mechanism for this process is still elusive. What is the key factor that controls the cavitation process, or is the cavitation is related to a critical shear strain or strain rate or other properties (such as the free volume or the viscosity) during the deformation process of a shear band? What happens in the atomic-scale structure when a nano-scale void is formed in a shear band? More advanced experimental techniques and sophisticated simulations are expected to address this issue.
- *Correlation between the fracture toughness and the atomic structure:* Some BMGs show large fracture toughness comparable to that of steels and Ti-based alloys, while some are as brittle as oxide glasses. This large variability in the intrinsic toughness values of BMGs must be associated with their atomic structures. However, a clear correlation between fracture toughness and atomic structure such as the SRO configurations and their connection manner is not well established. Elucidating this issue needs comprehensive experimental and atomistic-simulation studies of the atomic-level structure as well as their correlation with the fracture behaviors of various BMGs. Progress made in this issue would help to clarify the correlation between the Poisson's ratio and the toughness/ductility in BMGs.
- *The crack instability, branching process and dynamic fracture of BMGs:* This long-standing issue is not limited to BMGs, but exists in other glassy and brittle materials as well. Crack instability and branching are the energy dissipation process during the dynamic fracture process of materials. Compared to that of brittle glassy materials, the dynamic fracture process of BMGs is more complex, which involves both the creation of new fracture surfaces and the inhomogeneous plastic deformation process at the crack tip. A fully quantitative description of the process from a combination of continuum fracture dynamic mechanics and the plastic flow mechanism of BMGs is far from established. The crack instability and branching process are also crucial for understanding the diverse patterns (vein-like patterns, nanoperiodical corrugations) observed on the fracture surface of BMGs.

- *Interdisciplinary BMGs fracture study:* The fracture study of BMGs could generate strong interdisciplinary interest and information for specialists outside the field of glasses. Information regarding BMG fracture has implications for understanding a lot of critical and far-from-equilibrium phenomena in nature. For example, the spatiotemporal striped patterns have been observed in a variety of disparate systems far from equilibrium, including vertically vibrated granular layers, Rayleigh–Benard convection cells, ferromagnetic films with dipolar interactions, biological systems, earth quakes, or closer to hand, in one's fingerprints. The observed nanoscale periodic patterns with a similar distinctive characteristics independent of loading conditions observed on the fracture surface of various BMGs, which are similar to various other nonequilibrium systems, demonstrate that the study of the fractals of dimple structures and periodic corrugations on the fracture surface of BMGs could provide a powerful clue toward the understanding of catastrophic fracture, crack dynamics and related energy dissipation mechanisms, which are the most poorly understood fundamental phenomena in materials science and condensed matter physics.

Acknowledgments

The financial supports of the NSF of China (Grant Nrs. 50321101, 50621061, 50921091, 50731008 and 51271195) and MOST 973 of China (Nrs. 2015CB856800) are appreciated. We thank D.Q. Zhao, Z. Wang, X.K. Xi, M.Z. Li, G. Wang, M.X. Pan, and H.Y. Bai for experimental assistance and insightful discussions.

References

[1] Klement W, Willens RH, Duwez P. Non-crystalline structure in solidified gold–silicon alloys. Nature 1960;187:869–70.
[2] Davis HA. In: Luborsky FE, editor. Amorphous metallic alloys. London: Butterworths; 1983.
[3] Kavesh S. In: Gillman JJ, editor. Metallic glasses. Metals Park, OH: ASM International; 1978.
[4] Johnson WL. Fundamental aspects of bulk metallic glass formation in multicomponent alloys. Mater Sci Forum 1996;225–227:35–50.
[5] Inoue A. Stabilization of metallic supercooled liquid and bulk amorphous alloys. Acta Mater 2000;48:279–306.
[6] Löffler JF. Bulk metallic glasses. Intermetallics 2003;11:529–40.
[7] Telford M. The case for bulk metallic glass. Mater Today 2004;7:36–43.
[8] Schuh C, Hufnagel T, Ramamurty U. Mechanical behavior of amorphous alloys. Acta Mater 2007;55:4067–109.
[9] Greer AL, Ma E. Bulk metallic glasses: at the cutting edge of metals research. MRS Bull 2007;32:611–9.
[10] Wang WH, Dong C, Shek CH. Bulk metallic glasses. Mater Sci Eng: R 2004;44:45–89.
[11] Hofmann DC. Bulk metallic glasses and their composites: a brief history of diverging fields. J Mater 2013;13:8.
[12] Schroers J. Bulk metallic glasses. Phys Today 2013;66:32–7.
[13] Wang WH. Roles of minor additions in formation and properties of bulk metallic glasses. Prog Mater Sci 2007;52:540–96.
[14] Johnson WL. Bulk amorphous metals: an emerging engineering material. JOM 2002;54:40–3.
[15] Wang WH. Bulk metallic glasses with functional physical properties. Adv Mater 2009;21:4524–44.
[16] Cheng YQ, Ma E. Atomic-level structure and structure–property relationship in metallic glasses. Prog Mater Sci 2011;56:379–473.
[17] Chen M. Mechanical behavior of metallic glasses: microscopic understanding of strength and ductility. Annu Rev Mater Res 2008;38:445–69.
[18] Wang WH. The elastic properties, elastic models and elastic perspectives of metallic glasses. Prog Mater Sci 2012;57:487–656.
[19] Trexler MM, Thadhani NN. Mechanical properties of bulk metallic glasses. Prog Mater Sci 2010;55:759–839.
[20] Lawn B. Fracture of brittle solids. Cambridge University Press; 1993.
[21] Field JE. Brittle fracture: its study and application. Contemp Phys 1971;12:1–31.
[22] Xu J, Ramamurty U, Ma E. The fracture toughness of bulk metallic glasses. JOM 2010;62:10–8.
[23] Gilbert CJ, Ritchie RO, Johnson WL. Fracture toughness and fatigue-crack propagation in ZrTiNiCuBe bulk metallic glass. Appl Phys Lett 1997;71:476.
[24] Zhang ZF, Wu FF, Gao W, Tan J, Wang ZG, Stoica M, et al. Wavy cleavage fracture of bulk metallic glass. Appl Phys Lett 2006;89:251917.
[25] Wang G, Chan KC, Xu XH, Wang WH. Instability of crack propagation in brittle bulk metallic glass. Acta Mater 2008;56:5845–60.
[26] Falk ML. Molecular-dynamics study of ductile and brittle fracture in model noncrystalline solids. Phys Rev B 1999;60:7062–70.
[27] Murali P, Guo TF, Zhang YW, Narasimhan R, Li Y, Gao HJ. Atomic scale fluctuations govern brittle fracture and cavitation behavior in metallic glasses. Phys Rev Lett 2011;107:215501.
[28] Argon AS, Salama M. The mechanism of fracture in glassy materials capable of some inelastic deformation. Mater Sci Eng 1976;23:219–30.
[29] Furukawa A, Tanaka H. Inhomogeneous flow and fracture of glassy materials. Nat Mater 2009;8:601–9.

[30] Tandaiya P, Narasimhan R, Ramamurty U. Mode I crack tip fields in amorphous materials with application to metallic glasses. Acta Mater 2007;55:6541–52.
[31] Tandaiya P, Ramamurty U, Narasimhan R. Mixed mode (I and II) crack tip fields in bulk metallic glasses. J Mech Phys Solids 2009;57:1880–97.
[32] Griffith AA. The phenomena of rupture and flow in solids. Philos Trans R Soc Lond Ser A 1921;221:163–98.
[33] Irwin G. Analysis of stresses and strains near the end of a crack traversing a plate. J Appl Mech 1957;24:361–4.
[34] Erdogan F. Fracture mechanics. Int J Solids Struct 2000;37:171–83.
[35] Rooke DP, Cartwright DJ. Compendium of stress intensity factors. HMSO Ministry of Defence. Procurement Executive; 1976
[36] Sih GC, Macdonald B. Fracture mechanics applied to engineering problems – strain energy density fracture criterion. Eng Fract Mech 1974;6:361–86.
[37] Rice JR. A path independent integral and the approximate analysis of strain concentration by notches and cracks. J Appl Mech 1968;35:379–86.
[38] Zhu X-K, Joyce JA. Review of fracture toughness (G, K, J, CTOD, CTOA) testing and standardization. Eng Fract Mech 2012;85:1–46.
[39] Kobayashi AS, Chiu ST, Beeuwkes R. A numerical and experimental investigation on the use of *J*-integral. Eng Fract Mech 1973;5:293–305.
[40] Wells AA. Application of fracture mechanics at and beyond general yielding. Br Weld J 1963;10:563–70.
[41] E08 Committee. E1820-11e2 standard test method for measurement of fracture toughness. West Conshohocken, PA: ASTM International; 2011.
[42] E08 Committee. E399-12e1 standard test method for measurement of fracture toughness KIc of metallic materials. West Conshohocken, PA: ASTM International; 2011.
[43] Lu J, Ravichandran G, Johnson WL. Deformation behavior of ZrTiCuNiBe bulk metallic glass on strain-rates and temperatures. Acta Mater 2003;51:3429–43.
[44] Chen M, Inoue A, Zhang W, Sakurai T. Extraordinary plasticity of ductile bulk metallic glasses. Phys Rev Lett 2006;96:245502.
[45] Spaepen F. A microscopic mechanism for steady state inhomogeneous flow in metallic glasses. Acta Metall 1977;25:407–15.
[46] Argon AS. Plastic deformation in metallic glasses. Acta Metall 1979;27:47–58.
[47] Lewandowski JJ, Greer AL. Temperature rise at shear bands in metallic glasses. Nat Mater 2006;5:15–8.
[48] Donovan PE, Stobbs WM. The structure of shear bands in metallic glasses. Acta Metall 1981;29:1419–36.
[49] Wright WJ, Hufnagel TC, Florando JN. Studies of shear band velocity using spatially and temporally resolved measurements of strain during quasistatic compression of a bulk metallic glass. Acta Mater 2009;57:4639–48.
[50] Bruck HA, Rosakis AJ, Johnson WL. The dynamic compressive behavior of beryllium bearing bulk metallic glasses. J Mater Res 1996;11:503–11.
[51] Jiang WH, Liao HH, Liaw PK. Rate-dependent temperature increases in shear bands of a bulk-metallic glass. Metall Mater Trans A 2008;39:1822–30.
[52] Liu CT, Heatherly L, Horton JA, Easton DS, Carmichael CA, Wright JL, et al. Test environments and mechanical properties of Zr-base bulk amorphous alloys. Metall Mater Trans A 1998;29:1811–20.
[53] Bulatov VV, Argon AS. A stochastic model for continuum elasto-plastic behavior. I. Numerical approach and strain localization. Model Simul Mater Sci Eng 1994;2:167–85.
[54] Falk ML, Langer JS. Dynamics of viscoplastic deformation in amorphous solids. Phys Rev E 1998;57:7192–205.
[55] Bouchbinder E, Langer JS, Procaccia I. Athermal shear-transformation-zone theory of amorphous plastic deformation. I. Basic principles. Phys Rev E 2007;75:036107.
[56] Johnson WL, Samwer K. A universal criterion for plastic yielding of metallic glasses with $(T/T)^{2/3}$ temperature dependence. Phys Rev Lett 2005;95:195501.
[57] Steif PS, Spaepen F, Hutchinson JW. Strain localization in amorphous metals. Acta Metall 1982;30:447–55.
[58] Huang R, Suo Z, Prevost JH, Nix WD. Inhomogeneous deformation in metallic glasses. J Mech Phys Solids 2002;50:1011–27.
[59] Yang Q, Mota A, Ortiz M. A finite-deformation constitutive model of bulk metallic glass plasticity. Comput Mech 2006;37:194–204.
[60] Jiang MQ, Dai LH. On the origin of shear banding instability in metallic glasses. J Mech Phys Solids 2009;57:1267–92.
[61] Dasgupta R, Hentschel HGE, Procaccia I. Microscopic mechanism of shear bands in amorphous solids. Phys Rev Lett 2012;109:255502.
[62] Dmowski W, Iwashita T, Chuang CP, Almer J, Egami T. Elastic heterogeneity in metallic glasses. Phys Rev Lett 2010;105:205502.
[63] Ye JC, Lu J, Liu CT, Wang Q, Yang Y. Atomistic free-volume zones and inelastic deformation of metallic glasses. Nat Mater 2010;9:619–23.
[64] Wagner H, Bedorf D, Küchemann S, Schwabe M, Zhang B, Arnold W, et al. Local elastic properties of a metallic glass. Nat Mater 2011;10:439–42.
[65] Wang Z, Wen P, Huo LS, Bai HY, Wang WH. Signature of viscous flow units in apparent elastic regime of metallic glasses. Appl Phys Lett 2012;101:121906.
[66] Jiao W, Wen P, Peng HL, Bai HY, Sun BA, Wang WH. Evolution of structural and dynamic heterogeneities and activation energy distribution of deformation units in metallic glass. Appl Phys Lett 2013;102:101903.
[67] Cheng YQ, Ma E. Configurational dependence of elastic modulus of metallic glass. Phys Rev B 2009;80:064104.
[68] Huo LS, Ma J, Bai HY, Wang WH. Deformation units in metallic glasses revealed by stress-induced localized glass transition. J Appl Phys 2012;111:113522.
[69] Jiao W, Sun BA, Wen P, Bai HY, Kong QP, Wang WH. Crossover from stochastic activation to cooperative motions of shear transformation zones in metallic glasses. Appl Phys Lett 2013;103:081904.

[70] Fujita T, Wang W, Chen M. Low temperature uniform plastic deformation of metallic glasses during elastic iteration. Acta Mater 2012;60:3741.
[71] Liu YH, Wang D, Nakajima K, Zhang W, Hirata A, Nishi T, et al. Characterization of nanoscale mechanical heterogeneity in a metallic glass by dynamic force microscopy. Phys Rev Lett 2011;106:125504.
[72] Liu ST, Wang Z, Peng HL, Yu HB, Wang WH. The activation energy and volume of flow units of metallic glasses. Scripta Mater 2012;67:9–12.
[73] Khonik SV, Granato AV, Joncich DM, Pompe A, Khonik VA. Evidence of distributed interstitialcy-like relaxation of the shear modulus due to structural relaxation of metallic glasses. Phys Rev Lett 2008;100:065501.
[74] Schall P, Weitz DA, Spaepen F. Structural rearrangements that govern flow in colloidal glasses. Science 2007;318:1895–9.
[75] Huang PY, Kurasch S, Alden JS, Shekhawat A, Alemi AA, McEuen PL, et al. Imaging atomic rearrangements in two-dimensional silica glass: watching silica's dance. Science 2013;342:224–7.
[76] Ediger MD, Harrowell P. Perspective: supercooled liquids and glasses. J Chem Phys 2012;137:080901.
[77] Leocmach M, Tanaka H. Roles of icosahedral and crystal-like order in the hard spheres glass transition. Nat Commun 2012;3:974.
[78] Peng HL, Li MZ, Wang WH. Structural signature of plastic deformation in metallic glasses. Phys Rev Lett 2011;106:135503.
[79] Wang WH. Correlation between relaxations and plastic deformation, and elastic model of flow in metallic glasses and glass-forming liquids. J Appl Phys 2011;110:053221.
[80] Liu ST, Jiao W, Sun BA, Wang WH. A quasi-phase perspective on flow units of glass transition and plastic flow in metallic glasses. J Non-Cryst Solids 2013;376:76–80.
[81] Jiao W, Wen P, Bai HY, Kong QP, Wang WH. Transiently suppressed relaxations in metallic glass. Appl Phys Lett 2013;103:161902.
[82] Huo LS, Zeng JF, Wang WH, Liu CT, Yang Y. The dependence of shear modulus on dynamic relaxation and evolution of local structural heterogeneity in a metallic glass. Acta Mater 2013;61:4329–38.
[83] Zhu ZG, Wen P, Wang DP, Wang WH. Characterization of flow units in metallic glass through structural relaxations. J Appl Phys 2013;114:083512.
[84] Xue RJ, Wang DP, Zhang B, Wang WH. Characterization of flow units in metallic glass through density variation. J Appl Phys 2013;114:123514.
[85] Wang DP, Zhu ZG, Bai HY, Wang WH. Structural perspectives on the elastic and mechanical properties of metallic glasses. J Appl Phys 2013;114:173505.
[86] Yu HB, Wang WH, Bai HY, Wu Y, Chen MW. Relating activation of shear transformation zones to β relaxations in metallic glasses. Phys Rev B 2010;81:220201.
[87a] Yu HB, Shen X, Wang Z, Wang WH, Bai HY. Tensile plasticity in metallic glasses with pronounced β relaxations. Phys Rev Lett 2012;108:015504.
[87b] Lu Z, Jiao W, Wang WH, Bai HY. Flow unit perspective on room temperature homogeneous plastic deformation in metallic glasses. Phys Rev Lett 2014;113:045501.
[88] Wang Z, Sun BA, Bai HY, Wang WH. Evolution of hidden localized flow during glass-to-liquid transition in metallic glass. Nat Commun 2014;5:5823.
[89] Song SX, Nieh TG. Flow serration and shear-band viscosity during inhomogeneous deformation of metallic glass. Intermetallics 2009;17:762–7.
[90] Zhang ZF, Eckert J, Schultz L. Difference in compressive and tensile fracture mechanisms of ZrCuAlNiTi bulk metallic glass. Acta Mater 2003;51:1167–79.
[91] Greer AL, Cheng YQ, Ma E. Shear bands in metallic glasses. Mater Sci Eng: R 2013;74:71–132.
[92] Sun BA, Pauly S, Tan J, Stoica M, Wang WH, Kühn U, et al. Serrated flow and stick–slip deformation dynamics in the presence of shear-band interactions for a Zr-based metallic glass. Acta Mater 2012;60:4160–71.
[93] Sarmah R, Ananthakrishna G, Sun BA, Wang WH. Hidden order in serrated flow of metallic glasses. Acta Mater 2011;59:4482–93.
[94] Klaumünzer D, Lazarev A, Maaß R, Dalla Torre FH, Löffler JF. Probing shear-band initiation in metallic glasses. Phys Rev Lett 2011;107:185502.
[95] Klaumünzer D, Maaß R, Löffler JF. Stick-slip dynamics and recent insights into shear banding in metallic glasses. J Mater Res 2011;26:1453–63.
[96] Song SX, Nieh TG. Direct measurements of shear band propagation in metallic glasses – an overview. Intermetallics 2011;19:1968–77.
[97] Neuhäuser H. Rate of shear band formation in metallic glasses. Scripta Metall 1978;12:471–4.
[98] Wright WJ, Saha R, Nix WD. Deformation mechanisms of the $Zr_{40}Ti_{14}Ni_{10}Cu_{12}Be_{24}$ bulk metallic glass. Mater Trans, JIM 2001;42:642–9.
[99] Vinogradov AY, Khonik VA. Kinetics of shear banding in a bulk metallic glass monitored by acoustic emission measurements. Philos Mag 2004;84:2147–66.
[100] Sun BA, Pauly S, Hu J, Wang WH, Kühn U, Eckert J. Origin of intermittent plastic flow and instability of shear band sliding in bulk metallic glasses. Phys Rev Lett 2013;110:225501.
[101] Ke HB, Sun BA, Liu CT, Yang Y. Effect of size and base-element on the jerky flow dynamics in metallic glass. Acta Mater 2014;63:180–90.
[102] Dubach A, Dalla Torre FH, Löffler JF. Constitutive model for inhomogeneous flow in bulk metallic glasses. Acta Mater 2009;57:881–92.
[103] Lewandowski JJ, Wang WH, Greer AL. Intrinsic plasticity or brittleness of metallic glasses. Philos Mag Lett 2005;85:77–87.
[104] Han Z, Wu WF, Li Y, Wei YJ, Gao HJ. An instability index of shear band for plasticity in metallic glasses. Acta Mater 2009;57:1367–72.
[105] Wu WF, Li Y, Schuh CA. Strength, plasticity and brittleness of bulk metallic glasses under compression. Philos Mag 2007;88:71–89.
[106] Cheng YQ, Han Z, Li Y, Ma E. Cold versus hot shear banding in bulk metallic glass. Phys Rev B 2009;80:134115.

[107] Kumar J, Ciccotti M, Ananthakrishna G. Hidden order in crackling noise during peeling of an adhesive tape. Phys Rev E 2008;77:045202.
[108] Miguel MC, Vespignani A, Zapperi S, Weiss J, Grasso J-R. Intermittent dislocation flow in viscoplastic deformation. Nature 2001;410:667–71.
[109] Weiss J, Marsan D. Three-dimensional mapping of dislocation avalanches: clustering and space/time coupling. Science 2003;299:89–92.
[110] Mertens F, Franklin SV, Marder M. Dynamics of plastic deformation fronts in an aluminum alloy. Phys Rev Lett 1997;78:4502–5.
[111] Dimiduk DM, Woodward C, LeSar R, Uchic MD. Scale-free intermittent flow in crystal plasticity. Science 2006;312:1188–90.
[112] Sun BA, Yu HB, Jiao W, Bai HY, Wang WH. Plasticity of ductile metallic glasses: a self-organized critical state. Phys Rev Lett 2010;105:035501.
[113] Ananthakrishna G, Kubin LP. Crossover from chaotic to self-organized critical dynamics in jerky flow of single crystals. Phys Rev E 1999;60:5455–62.
[114] Bak P, Tang C, Wiesenfeld K. Self-organized criticality. Phys Rev A 1988;38:364–74.
[115] Carlson JM, Langer JS. Properties of earthquakes generated by fault dynamics. Phys Rev Lett 1989;62:2632–5.
[116] Sun BA, Wang WH. Fractal nature of multiple shear bands in severely deformed metallic glass. Appl Phys Lett 2011;98:201902.
[117] Conner RD, Li Y, Nix WD, Johnson WL. Shear band spacing under bending of Zr-based metallic glass plates. Acta Mater 2004;52:2429–34.
[118] Chen Y, Jiang MQ, Dai LH. Collective evolution dynamics of multiple shear bands in bulk metallic glasses. Int J Plast 2013;50:18–36.
[119] Ravichandran G, Molinari A. Analysis of shear banding in metallic glasses under bending. Acta Mater 2005;53:4087–95.
[120] Conner RD, Johnson WL, Paton NE, Nix WD. Shear bands and cracking of metallic glass plates in bending. J Appl Phys 2003;94:904–11.
[121] Zhang H, Maiti S, Subhash G. Evolution of shear bands in bulk metallic glasses under dynamic loading. J Mech Phys Solids 2008;56:2171–87.
[122] Demetriou MD, Launey ME, Garrett G, Schramm JP, Hofmann DC, Johnson WL, et al. A damage-tolerant glass. Nat Mater 2011;10:123–8.
[123] Yokoyama Y, Yavari AR, Inoue A. Malleable ZrNiCuAl bulk glassy alloys with tensile plastic elongation at room temperature. Philos Mag Lett 2009;89:322.
[124] Guo H, Yan PF, Wang YB, Tan J, Zhang ZF, Sui ML, et al. Tensile ductility and necking of metallic glass. Nat Mater 2007;6:735–9.
[125] Liu YH, Wang G, Wang RJ, Zhao DQ, Pan MX, Wang WH. Super plastic bulk metallic glasses at room temperature. Science 2007;315:1385–8.
[126] Das J, Tang MB, Kim KB, Baier F, Wang WH, et al. "Work-hardenable" ductile bulk metallic glass. Phys Rev Lett 2005;94:205501.
[127] Mukai T, Nieh TG, Inoue A, Higashi K. Effect of strain rate on compressive behavior of a $Pd_{40}Ni_{40}P_{20}$ bulk metallic glass. Intermetallics 2002;10:1071–7.
[128] Chen Y, Jiang MQ, Wei YJ, Dai LH. Failure criterion for metallic glasses. Philos Mag 2011;91:4536–54.
[129] Zhang Z, Eckert J. Unified tensile fracture criterion. Phys Rev Lett 2005:94.
[130] Desai CS, Siriwardane HJ. Constitutive laws for engineering materials. Englewood Cliffs, NJ: Prentice-Hall; 1984.
[131] Zhang Z, He G, Eckert J, Schultz L. Fracture mechanisms in bulk metallic glassy materials. Phys Rev Lett 2003:91.
[132] Sun BA, Tan J, Pauly S, Kuhn U, Eckert J. Stable fracture of a malleable Zr-based bulk metallic glass. J Appl Phys 2012;112:103533.
[133] Wang G, Zhao D, Bai H, Wang WH, et al. Nanoscale periodic morphologies on the fracture surface of brittle metallic glasses. Phys Rev Lett 2007;98:235501.
[134] Schultz R, Jensen M, Bradt R. Single crystal cleavage of brittle materials. Int J Fract 1994;65:291–312.
[135] Jiang MQ, Ling Z, Meng JX, Dai LH. Energy dissipation in fracture of bulk metallic glasses via inherent competition between local softening and quasi-cleavage. Philos Mag 2008;88:407–26.
[136] Zhao K, Xia XX, Bai HY, Zhao DQ, Wang WH. Room temperature homogeneous flow in a bulk metallic glass with low glass transition temperature. Appl Phys Lett 2011;98:141913.
[137] Stoica M, Eckert J, Wang WH. Mechanical behavior of FeCrMoGa4PCB bulk metallic glass. Intermetallics 2005;13:764–9.
[138] Zhang ZF, Zhang H, Shen BL, Inoue A, Eckert J. Shear fracture and fragmentation mechanisms of bulk metallic glasses. Philos Mag Lett 2006;86:643–50.
[139] Ghosh AK. Tensile instability and necking in materials with strain hardening and strain-rate hardening. Acta Metall 1977;25:1413–24.
[140] Greer JR, De Hosson JTM. Plasticity in small-sized metallic systems: intrinsic versus extrinsic size effect. Prog Mater Sci 2011;56:654–724.
[141] Hofmann DC, Suh JY, Wiest A, Duan G, Lind ML, Demetriou MD, et al. Designing metallic glass matrix composites with high toughness and tensile ductility. Nature 2008;451:1085–9.
[142] Wu Y, Xiao Y, Chen G, Liu CT, Lu Z. Bulk metallic glass composites with transformation-mediated work-hardening and ductility. Adv Mater 2010;22:2770.
[143] Hofmann DC, Suh JY, Wiest A, Lind ML, Demetriou MD, Johnson WL. Development of tough, low-density titanium-based bulk metallic glass matrix composites with tensile ductility. Proc Natl Acad Sci USA 2008;105:20136–40.
[144] Han Z, Yang H, Wu WF, Li Y. Invariant critical stress for shear banding in a bulk metallic glass. Appl Phys Lett 2008;93:231912.
[145] Wang WH. Correlations between elastic moduli and properties in bulk metallic glasses. J Appl Phys 2006;99:093506.
[146] Yuan CC, Xi XK. On the correlation of Young's modulus and the fracture strength of metallic glasses. J Appl Phys 2011;109:033515.

[147] Davis LA, Kavesh S. Deformation and fracture of an amorphous metallic alloy at high pressure. J Mater Sci 1975;10:453–9.
[148] Lewandowski JJ, Lowhaphandu P. Effects of hydrostatic pressure on the flow and fracture of a bulk amorphous metal. Philos Mag A 2002;82:3427–41.
[149] Lu J, Ravichandran G. Pressure-dependent flow behavior of ZrTiCuNiBe bulk metallic glass. J Mater Res 2003;18:2039–49.
[150] Flores KM, Dauskardt RH. Mean stress effects on flow localization and failure in a bulk metallic glass. Acta Mater 2001;49:2527–37.
[151] Vaidyanathan R, Dao M, Suresh S. Study of mechanical deformation in bulk metallic glass through instrumented indentation. Acta Mater 2001;49:3781–9.
[152] Lowhaphandu P, Lewandowski JJ. Effects of superimposed hydrostatic pressure on fracture of ZrTiNiCuBe bulk amorphous alloy. Scripta Mater 1999;41:19–24.
[153] Yu HB, Wang WH, Shek CH, Bai HY. Statistic analysis of the mechanical behavior of bulk metallic glasses. Adv Eng Mater 2009;11:370–3.
[154] Mayer MA, Chawla KK. Mechanical behavior of materials. Upper Saddle River, NJ: Prentice Hall; 1999.
[155] Courtney TH. Mechanical behavior of materials. New York: McGraw-Hill; 2000.
[156] Qu RT, Eckert J, Zhang ZF. Tensile fracture criterion of metallic glass. J Appl Phys 2011;109:083544.
[157] Schuh CA, Lund AC. Atomistic basis for the plastic yield criterion of metallic glass. Nat Mater 2003;2:449–52.
[158] Gludovatz B, Naleway SE, Ritchie RO, Kruzic JJ. Size-dependent fracture toughness of bulk metallic glasses. Acta Mater 2014;70:198–207.
[159] He Q, Cheng Y-Q, Ma E, Xu J. Locating bulk metallic glasses with high fracture toughness. Acta Mater 2011;59:202–15.
[160] Kimura H, Masumoto T. Fracture toughness of amorphous metals. Scripta Metall 1975;9:211–21.
[161] Ast DG, Krenitsky D. Fracture toughness and yield strength of annealed Ni–Fe base metallic glasses. Mater Sci Eng 1976;23:241–6.
[162] Cornner RD, Rosakis AJ, Johnson WL. Fracture toughness determination for a beryllium-bearing bulk metallic glass. Scripta Mater 1997;37:1373–8.
[163] Gilbert CJ, Schroeder V, Ritchie RO. Mechanisms for fracture and fatigue-crack propagation in a bulk metallic glass. Metall Mater Trans A 1999;30:1739–53.
[164] Lowhaphandu P, Lewandowski JJ. Fracture toughness and notched toughness of bulk amorphous alloy: Zr–Ti–Ni–Cu–Be. Scripta Mater 1998;38:1811–7.
[165] Lowhaphandu P, Lewandowski JJ. Deformation and fracture toughness of a bulk amorphous ZrTiNiCuBe alloy. Intermetallics 2000;8:487–92.
[166] Schneibel JH, Horton JA, Munroe PR. Fracture toughness, fracture morphology, and crack-tip plastic zone of a Zr-based bulk amorphous alloy. Metall Mater Trans A 2001;32:2819.
[167] Kawashima A, Inoue A. Fracture toughness of $Zr_{55}Al_{10}Ni_5Cu_{30}$ bulk metallic glass by 3-point bend testing. Mater Trans, JIM 2005;46:1725.
[168] Kim CP, Lind ML, Conner RD, Johnson WL. Fracture toughness study of new Zr-based Be-bearing bulk metallic glasses. Scripta Mater 2009;60:80.
[169] He Q, Shang JK, Ma E, Xu J. Crack-resistance curve of a ZrTiCuAl bulk metallic glass with extraordinary fracture toughness. Acta Mater 2012;60:4940.
[170] Flores KM, Dauskardt RH. Mode II fracture behavior of a Zr-based bulk metallic glass. J Mech Phys Solids 2006;54:2418–35.
[171] Varadarajan R, Thurston A, Lewandowski J. Increased toughness of zirconium-based bulk metallic glasses tested under mixed mode conditions. Metall Mater Trans A 2010;41:149–58.
[172] Schroers J, Johnson WL. Ductile bulk metallic glass. Phys Rev Lett 2004;93:255506.
[173] Xi XK, Zhao D, Pan M, Wang W, Wu Y, Lewandowski J. Fracture of brittle metallic glasses: brittleness or plasticity. Phys Rev Lett 2005;94:125510.
[174] Jia P, Zhu Z-d, Ma E, Xu J. Notch toughness of Cu-based bulk metallic glasses. Scripta Mater 2009;61:137–40.
[175] Gu XJ, Poon SJ, Shiflet GJ, Lewandowski JJ. Compressive plasticity and toughness of a Ti-based bulk metallic glass. Acta Mater 2010;58:1708.
[176] Ashby M, Greer A. Metallic glasses as structural materials. Scripta Mater 2006;54:321.
[177] Joyce JT. R. West Conshohocken, PA: ASTM International; 2000.
[178] Henann DL, Anand L. Fracture of metallic glasses at notches: effects of notch-root radius and the ratio of the elastic shear modulus to the bulk modulus on toughness. Acta Mater 2009;57:6057–7604.
[179] Guan P, Lu S, Spector MJB, Valavala PK, Falk ML. Cavitation in amorphous solids. Phys Rev Lett 2013;110:185502.
[180] Flores KM, Dauskardt RH. Enhanced toughness due to stable crack tip damage zones in bulk metallic glass. Scripta Mater 1999;41:937–43.
[181] McClintock FA. Fracture: an advanced treatise. New York: Academic Press; 1971.
[182] Sheng HW, Luo WK, Alamgir FM, Bai JM, Ma E. Atomic packing and short-to-medium-range order in metallic glasses. Nature 2006;439:419–25.
[183] Miracle DB, Egami T, Flores KM, Kelton KF. Structural aspects of metallic glasses. MRS Bull 2007;32:629–34.
[184] Liu ACY, Neish MJ, et al. Systematic mapping of icosahedral short-range order in a melt-spun ZrCu metallic glass. Phys Rev Lett 2013;110:205505.
[185] Ma D, Stoica AD, Wang XL, Lu ZP, Clausen B, Brown DW. Elastic moduli inheritance and the weakest link in bulk metallic glasses. Phys Rev Lett 2012;108:085501.
[186] Hirata A, Guan P, Fujita T, Hirotsu Y, Inoue A, Yavari AR, et al. Direct observation of local atomic order in a metallic glass. Nat Mater 2011;10:28–33.
[187] Peng HL, Li MZ, Wang WH. Effect of local structures and atomic packing on glass forming ability in CuZr metallic glasses. Appl Phys Lett 2010;96:021901.
[188] Boudreaux DS, Frost HJ. Short-range order in theoretical models of binary metallic glass alloys. Phys Rev B 1981;23:1506–16.

[189] Waseda Y, Chen HS. A structural study of metallic glasses containing boron (Fe–B, Co–B, and Ni–B). Phys Status Solidi A 1978;49:387–92.
[190] Tan J, Zhang Y, Sun BA, et al. Correlation between internal states and plasticity in bulk metallic glass. Appl Phys Lett 2011;98:151906.
[191] Adda-Bedia M, Arias RE, Bouchbinder E, Katzav E. Dynamic stability of crack fronts: out-of-plane corrugations. Phys Rev Lett 2013;110:014302.
[192] Gu XJ, Poon SJ, Shiflet GJ, Lewandowski JJ. Ductile-to-brittle transition in a Ti-based bulk metallic glass. Scripta Mater 2009;60:1027–30.
[193] Zhu Z-D, Ma E, Xu J. Elevating the fracture toughness of CuHfAl metallic glass. Intermetallics 2014;46:164–72.
[194] Aydiner CC, Üstündag E. Residual stresses in a bulk metallic glass cylinder induced by thermal tempering. Mech Mater 2005;37:201–12.
[195] Aydiner CC, Üstündag E, Prime MB, Peker A. Modeling and measurement of residual stresses in metallic glass plate. J Non-Cryst Solids 2003;316:82–95.
[196] Launey ME, Busch R, Kruzic JJ. Effects of free volume changes and residual stresses on the fatigue and fracture behavior of a ZrTiNiCuBe bulk metallic glass. Acta Mater 2008;56:500–10.
[197] Conner RD, Maire RE, Johnson WL. Effect of oxygen concentration upon the ductility of amorphous ZrNbAlCuNi. Mater Sci Eng: A 2006;419:148–52.
[198] Keryvin V, Bernard C, Rouxel T. Toughness of ZrCuAlNi bulk metallic glass for two oxygen levels. J Non-Cryst Solids 2006;352:2863–8.
[199] Shamimi Nouri A, Gu XJ, Poon SJ, Shiflet GJ, Lewandowski JJ. Chemistry (intrinsic) and inclusion (extrinsic) effects on the toughness and Weibull modulus of Fe-based bulk metallic glasses. Philos Mag Lett 2008;88:853–61.
[200] Madge SV, Louzguine-Luzgin DV, Lewandowski JJ, Greer AL. Toughness, extrinsic effects and Poisson's ratio of bulk metallic glasses. Acta Mater 2012;60:4800–9.
[201] Riontino G, Baricco M. Structural relaxation in metallic glasses. Philos Mag B 1987;56:177–83.
[202] Debenedetti PG, Stillinger FH. Supercooled liquids and the glass transition. Nature 2001;410:259–67.
[203] Murali P, Ramamurty U. Embrittlement of a bulk metallic glass due to sub-annealing. Acta Mater 2005;53:1467–78.
[204] Wu T-W, Spaepen F. The relation between embrittlement and structural relaxation of an amorphous metal. Philos Mag B 1990;61:739–50.
[205] Bhowmick R, Raghavan R, Chattopadhyay K, Ramamurty U. Plastic flow softening in a bulk metallic glass. Acta Mater 2006;54:4221–8.
[206] Van Den Beukel A, Radelaar S. On the kinetics of structural relaxation in metallic glasses. Acta Metall 1983;31:419–27.
[207] Slipenyuk A, Eckert J. Correlation between enthalpy change and free volume reduction during structural relaxation of $Zr_{55}Cu_{30}Al_{10}Ni_5$ metallic glass. Scripta Mater 2004;50:39–44.
[208] Pan D, Inoue A, Sakurai T, Chen MW. Experimental characterization of shear transformation zones for plastic flow of bulk metallic glasses. Proc Natl Acad Sci USA 2008;105:14769–72.
[209] Pan D, Yokoyama Y, Fujita T, Liu YH, Kohara S, Inoue A, et al. Correlation between structural relaxation and shear transformation zone volume of a bulk metallic glass. Appl Phys Lett 2009;95:141909.
[210] Dalla Torre FH, Dubach A, Siegrist ME, Löffler JF. Negative strain rate sensitivity in bulk metallic glass and its similarities with the dynamic strain aging effect during deformation. Appl Phys Lett 2006;89:091918.
[211] Dalla Torre FH, Dubach A, Schällibaum J, Löffler JF. Shear striations and deformation kinetics in highly deformed Zr-based bulk metallic glasses. Acta Mater 2008;56:4635–46.
[212] Rycroft CH, Bouchbinder E. Fracture toughness of metallic glasses: annealing-induced embrittlement. Phys Rev Lett 2012;109:194301.
[213] Raghavan R, Murali P, Ramamurty U. Ductile to brittle transition in the ZrTiCuNiBe bulk metallic glass. Intermetallics 2006;14:1051–4.
[214] Khantha M, Pope DP, Vitek V. Dislocation screening and brittle-to-ductile transition. Phys Rev Lett 1994;73:684–7.
[215] Raghavan R, Murali P, Ramamurty U. On factors influencing the ductile-to-brittle transition in a bulk metallic glass. Acta Mater 2009;57:3332–40.
[216] Pan D, Guo H, Zhang W, Inoue A, Chen MW. Temperature-induced anomalous brittle-to-ductile transition of bulk metallic glasses. Appl Phys Lett 2011;99:241907.
[217] Garrett GR, Demetriou MD, Chen J, Johnson WL. Effect of microalloying on the toughness of metallic glasses. Appl Phys Lett 2012;101:241913.
[218] Yu P, Bai HY. Poisson's ratio and plasticity in CuZrAl bulk metallic glasses. Mater Sci Eng: A 2008;485:1–4.
[219] Lee ML, Li Y, Schuh CA. Effect of a controlled volume fraction of dendritic phases on tensile and compressive ductility in La-based metallic glass matrix composites. Acta Mater 2004;52:4121–31.
[220] Xing LQ, Li Y, Ramesh KT, Li J, Hufnagel TC. Enhanced plastic strain in Zr-based bulk amorphous alloys. Phys Rev B 2001;64:180201.
[221] Wang G, Liu YH, Pan MX, Wang WH. Structural evolution in TiCu-based bulk metallic glass with large compressive plasticity. Appl Phys Lett 2006;89:251909.
[222] Demetriou MD, Floyd M, Crewdson C, Schramm JP, Garrett G, Johnson WL. Liquid-like platinum-rich glasses. Scripta Mater 2011;65:799–802.
[223] Dasgupta R, Mishra P, Procaccia I, Samwer K. Micro-alloying and the toughness of glasses: modeling with pinned particles. Appl Phys Lett 2013;102:191904.
[224] Zheng N, Qu RT, Pauly S, Calin M, Gemming T, Zhang ZF, et al. Design of ductile bulk metallic glasses by adding "soft" atoms. Appl Phys Lett 2012;100:141901.
[225] Yuan CC, Xiang JF, Xi XK, Wang WH. NMR signature of evolution of ductile-to-brittle transition in bulk metallic glasses. Phys Rev Lett 2011;107:236403.
[226] Stillinger FH. A topographic view of supercooled liquids and glass formation. Science 1995;267:1935–9.
[227] Alexander S. Amorphous solids: their structure, lattice dynamics and elasticity. Phys Rep 1998;296:65–236.
[228] Rice JR, Thomson R. Ductile versus brittle behaviour of crystals. Philos Mag 1974;29:73–97.

[229] Pugh SF. Relations between the elastic moduli and the plastic properties of polycrystalline pure metals. Philos Mag 1954;45:823–43.
[230] Kelly A, Tyson WR, Cottrell AH. Ductile and brittle crystals. Philos Mag 1967;15:567–86.
[231] Song F, Zhou J, Xu X, Xu Y, Bai Y. Effect of a negative Poisson ratio in the tension of ceramics. Phys Rev Lett 2008;100:245502.
[232] Chen HS, Coleman E. Elastic constants, hardness and their implications to flow properties of metallic glasses. J Non-Cryst Solids 1975;18:157–71.
[233] Gu XJ, McDermott AG, Poon SJ, Shiflet GJ. Critical Poisson's ratio for plasticity in FeMoCBLn bulk amorphous steel. Appl Phys Lett 2006;88:211905.
[234] Wang JQ, Wang WH, Liu YH, Bai HY. Characterization of activation energy for flow in metallic glasses. Phys Rev B 2011;83:012201.
[235] Egami T. Formation and deformation of metallic glasses: atomistic theory. Intermetallics 2006;14:882–7.
[236] Liu ZQ, Zhang ZF. Universal softening and intrinsic local fluctuations in metallic glasses. Appl Phys Lett 2013;103.
[237] Lewandowski JJ, Gu XJ, Nouri AS, Poon SJ, Shiflet GJ. Tough Fe-based bulk metallic glasses. Appl Phys Lett 2008;92:091918.
[238] Choi-Yim H, Johnson WL. Bulk metallic glass matrix composites. Appl Phys Lett 1997;71:3808–10.
[239] Choi-Yim H, Busch R, Köster U, Johnson WL. Synthesis and characterization of particulate reinforced $Zr_{57}Nb_5Al_{10}Cu_{15.4}Ni_{12.6}$ bulk metallic glass composites. Acta Mater 1999;47:2455–62.
[240] Hays CC, Kim CP, Johnson WL. Microstructure controlled shear band pattern formation and enhanced plasticity of bulk metallic glasses containing in situ formed ductile phase dendrite dispersions. Phys Rev Lett 2000;84:2901–4.
[241] Flores KM, Johnson WL, Dauskardt RH. Fracture and fatigue behavior of a Zr–Ti–Nb ductile phase reinforced bulk metallic glass matrix composite. Scripta Mater 2003;49:1181–7.
[242] Pauly S, Gorantla S, Wang G, Kühn U, Eckert J. Transformation-mediated ductility in CuZr-based bulk metallic glasses. Nat Mater 2010;9:473–7.
[243] Jacques PJ, Furnémont Q, Lani F, Pardoen T, Delannay F. Multiscale mechanics of TRIP-assisted multiphase steels: I. Characterization and mechanical testing. Acta Mater 2007;55:3681–93.
[244] Wu Y, Wang H, Chen GL, et al. Formation of CuZrAl bulk metallic glass composites with improved tensile properties. Acta Mater 2011;59:2928–36.
[245] Liu Z, Li R, Liu G, Su W, Wang H, Li Y, et al. Microstructural tailoring and improvement of mechanical properties in CuZr-based bulk metallic glass composites. Acta Mater 2012;60:3128–39.
[246] Park JS, Lim HK, Park ES, Lee WH, Kim WT, et al. Fracture behavior of bulk metallic glass/metal laminate composites. Mater Sci Eng: A 2006;417:239–42.
[247] Sun BA, Cheung KP, Fan JT, Lu J, Wang WH. Fiber metallic glass laminates. J Mater Res 2010;25:2287–91.
[248] Wang Y, Li J, Hamza AV, Barbee TW. Ductile crystalline – amorphous nanolaminates. Proc Natl Acad Sci USA 2007;104:11155–60.
[249] Donohue A, Spaepen F, Hoagland RG, Misra A. Suppression of the shear band instability during plastic flow of nanometer-scale confined metallic glasses. Appl Phys Lett 2007;91:241905-3.
[250] Deibler LA, Lewandowski JJ. Model experiments to mimic fracture surface features in metallic glasses. Mater Sci Eng: A 2010;527:2207–13.
[251] Sharp DH. An overview of Rayleigh–Taylor instability. Physica D 1984;12:3–18.
[252] Takayama S, Maddin R. Fracture of amorphous Ni–Pd–P alloys. Philos Mag 1975;32:457–70.
[253] Suh J-Y, Dale Conner R, Paul Kim C, Demetriou MD, Johnson WL. Correlation between fracture surface morphology and toughness in Zr-based bulk metallic glasses. J Mater Res 2010;25:982–90.
[254] Wang G, Wang YT, Zhao DQ, Wang WH. Evolution of nanoscale morphology on fracture surface of brittle metallic glass. Appl Phys Lett 2006;89:121909.
[255] Xi XK, Zhao DQ, Pan MX, Wang WH, Wu Y, Lewandowski JJ. Periodic corrugation on dynamic fracture surface in brittle bulk metallic glass. Appl Phys Lett 2006;89:181911.
[256] Wang G, Han YN, Xu XH, Ke FJ, Han BS, Wang WH. Ductile to brittle transition in dynamic fracture of brittle bulk metallic glass. J Appl Phys 2008;103:093520.
[257] Wang YT, Xi XK, Wang WH. Understanding of nanoscale periodic stripes on fracture surface of metallic glasses. J Appl Phys 2009;106:113528.
[258] Xia XX, Wang WH. Characterization and modeling of breaking-induced spontaneous nanoscale periodic stripes in metallic glasses. Small 2012;8:1197–203.
[259] Bonamy D, Ravi-Chandar K. Interaction of shear waves and propagating cracks. Phys Rev Lett 2003;91:235502.
[260] Ravi-Chandar K, Yang B. On the role of microcracks in the dynamic fracture of brittle materials. J Mech Phys Solids 1997;45:535–63.
[261] Xia XX, Wang WH, Greer AL. Plastic zone at crack tip: a nanolab for formation and study of metallic glassy nanostructures. J Mater Res 2011;24:2986–92.
[262] Bouchaud E, Bouchaud JP, Fisher DS, Ramanathan S, Rice JR. Can crack front waves explain the roughness of cracks? J Mech Phys Solids 2002;50:1703–25.
[263] Charkaluk E, Bigerelle M, Iost A. Fractals and fracture. Eng Fract Mech 1998;61:119–39.
[264] Mandelbrot BB, Passoja DE, Paullay AJ. Fractal character of fracture surfaces of metals. Nature 1984;308:721–2.
[265] Bouchaud E. Scaling properties of cracks. J Phys: Condens Matter 1997;9:4319.
[266] Bouchaud E, Boivin D, Pouchou JL, Bonamy D, Poon B, Ravichandran G. Fracture through cavitation in a metallic glass. Europhys Lett 2008;83:66006.
[267] Jiang MQ, Meng JX, Gao JB, Wang XL, Rouxel T, Keryvin V, et al. Fractal in fracture of bulk metallic glass. Intermetallics 2010;18:2468–71.
[268] Gao M, Sun BA, Yuan CC, Ma J, Wang WH. Hidden order in the fracture surface morphology of metallic glasses. Acta Mater 2012;60:6952–60.

[269] Tandaiya P, Ramamurty U, Narasimhan R. Effect of Poisson's ratio on crack tip fields and fracture behavior of metallic glasses. Acta Mater 2008;56:6077–86.
[270] Picallo CB, López JM, Zapperi S, Alava MJ. From brittle to ductile fracture in disordered materials. Phys Rev Lett 2010;105:155502.
[271] Bathe K-J. Finite element method. Wiley encyclopedia of computer science and engineering. John Wiley & Sons, Inc.; 2007.
[272] Anand L, Su C. A theory for amorphous viscoplastic materials undergoing finite deformations, with application to metallic glasses. J Mech Phys Solids 2005;53:1362–96.
[273] Mendelev MI, Sordelet DJ, Kramer MJ. Using atomistic computer simulations to analyze X-ray diffraction data from metallic glasses. J Appl Phys 2007;102:043501.
[274] Tolman RC. The effect of droplet size on surface tension. J Chem Phys 1949;17:333–7.
[275] An Q, Garrett G, Samwer K, et al. Atomistic characterization of stochastic cavitation of a binary metallic liquid under negative pressure. J Phys Chem Lett 2011;2:1320–3.
[276] Pampillo CA, Reimschuessel AC. The fracture topography of metallic glasses. J Mater Sci 1974;9:718–24.
[277] Spaepen F. On the fracture morphology of metallic glasses. Acta Metall 1975;23:615–20.
[278] Deibler LA, Lewandowski JJ. Effects of changes in strain rate and test temperature on MgCaCu metallic glass. Mater Sci Eng: A 2010;527:2214–21.
[279] Alava MJ, Nukala PKVV, Zapperi S. Statistical models of fracture. Adv Phys 2006;55:349–476.
[280] Roux S, Hansen A. Perfect plasticity in a random medium. J Phys II: France 1992;2:1007–21.
[281] Picallo CB, López JM, Zapperi S, Alava MJ. Optimization and plasticity in disordered media. Phys Rev Lett 2009;103:225502.
[282] Dahmen KA, Ben-Zion Y, Uhl JT. A simple analytic theory for the statistics of avalanches in sheared granular materials. Nat Phys 2011;7:554–7.
[283] Kimura H, Masumoto T. Strength, ductility and toughness – a study in model mechanics. In: Luborsky FE, editor. Amorphous metallic alloys. London: Butterworths; 1983.
[284] Donovan PE. A yield criterion for $Pd_{40}Ni_{40}P_{20}$ metallic glass. Acta Metall 1989;37:445–56.
[285] Sergueeva AV, Mara NA, Kuntz JD, Lavernia EJ, Mukherjee AK. Shear band formation and ductility in bulk metallic glass. Philos Mag 2005;85:2671–87.
[286] Bruck HA, Christman T, Rosakis AJ, Johnson WL. Quasi-static constitutive behavior of ZrTiNiCuBe bulk amorphous alloys. Scripta Metall 1994;30:429–34.
[287] He GL, Bian Z, Chen GL. Fracture morphology and quenched-in precipitates induced embrittlement in Zr-base bulk glass. Mater Trans 2001;42:356–64.
[288] Zhang ZF, Eckert J, Schultz L. Fatigue and fracture behavior of bulk metallic glass. Metall Mater Trans A 2004;35:3489–98.
[289] Yoshikawa T, Tokuda M, Inaba T. Influence of thermoplastic deformation on mechanical properties of Zr-based bulk metallic glasses at room temperature. Int J Mech Sci 2008;50:888–96.
[290] Keryvin V, Rouxel T, Kawamura Y. Thermal stability of ZrCuAlNi metallic glass studied by in situ ultrasonic echography. Intermetallics 2002;10:1289.
[291] Szuecs F, Kim CP, Johnson WL. Mechanical properties of ZrTiNbCuNiBe ductile phase reinforced metallic glass composite. Acta Mater 2001;49:1507–13.
[292] Inoue A, Zhang W, Zhang T, Kurosaka K. High-strength Cu-based bulk glassy alloys in CuZrTi and CuHfTi ternary systems. Acta Mater 2001;49:2645–52.
[293] Masumoto T, Maddin R. The mechanical properties of palladium 20 a/o silicon alloy quenched from the liquid state. Acta Metall 1971;19:725–41.
[294] Pan DG, Zhang HF, Wang AM, Wang ZG, Hu ZQ. Fracture instability in brittle Mg-based bulk metallic glasses. J Alloys Compd 2007;438:145–9.
[295] Jiang WH, Liu FX, Qiao DC, Choo H, Liaw PK. Plastic flow in dynamic compression of a Zr-based bulk metallic glass. J Mater Res 2006;21:1570–5.
[296] Hassan HA, Kecskes L, Lewandowski JJ. Effects of changes in test temperature and loading conditions on fracture toughness of a Zr-based bulk metallic glass. Metall Mater Trans A 2008;39:2077–85.